



**UNIVERSITY of the  
WESTERN CAPE**

# **Development of a Bipolar Nickel-Iron Battery Prototype for Energy Storage**

**By**

**Mohamed Ali Ben Ltaief**

**Thesis submitted in fulfillment of the requirements for the degree**

**Master of Science in Chemical Sciences**

**Faculty of Natural Science**

**Department of Chemistry**

**At the University of the Western Cape**

**Supervisor**

**Prof Bernard Bladergroen**

**August 2021**

**UWC Copyright Information**

The thesis may not be published either in part (in scholarly, scientific, or technical journals) or as a whole (as a monograph) unless permission has been obtained from the university.

<http://etd.uwc.ac.za/>

## Declaration

I, Mohamed Ali Ben Ltaief, declare that the contents of this thesis represent my own work, and that it has not previously been submitted for academic examination towards any qualification. Furthermore, all resources I have used or quoted have been fully referenced. It represents my own opinions and not necessarily those of either University of the Western Cape or the South African Institute of Advanced Materials Chemistry.

Signed:



Date: 19/04/2021



## Abstract

Energy storage systems represent a viable option to integrate renewable energy sources into the grid network. Multiple energy storage technologies are available such as mechanical, electrical, thermal, and electrochemical storage technologies. Battery Energy Storage Systems are considered as an accepted solution for energy storage with advantages such as, sustained power delivery, geographical independence and, fast response capability.

This thesis describes the development of rechargeable bipolar Nickel-Iron batteries as potential candidates for cost effective energy storage solutions. The first objective of this work was to design a bipolar electrode comprising an Iron (Fe)-based anode, a Nickel (Ni)-based cathode and a flexible bipolar plate and to optimise its production process in order to attain high performance in terms of capacity and efficiency. Research questions to be answered included;

What is the optimal anode and cathode composition yielding appropriate electrode capacity?

What is the most suitable electrode processing technique and what are the optimised process parameters that will yield dimensionally stable electrodes?

The electrode electrochemical performance of the produced electrodes and battery prototype were evaluated using cyclic voltammetry and galvanostatic cycling in alkaline medium. Materials characterisation techniques, namely X-ray diffraction (XRD), scanning electrode microscopy (SEM) were used to study both charged and discharged electrodes. The second objective was to develop a battery stack assembly using a laser welding technique.

The capacity of the nickel-based electrode material was increased from 90 mAh.g<sup>-1</sup> using a commercial Q-lite Nickel electrode to 140 mAh.g<sup>-1</sup> using a composite electrode. Important to note is that the electrode material was selected from industrial-grade material. The inclusion of Cu besides the graphite resulted in marginal stability improvement and further 10 % of specific capacity. Replacing the production mould from Stainless Steel (SS) to silicon resulted into a variation in electrode thickness was greatly reduced from 0.3 mm to 0.05 mm. This was a critical achievement as dimensional differences between bipolar electrodes have a great impact on the performance of the battery stack. Temperature, pressure, and pressing time have a major impact on the overall performance of the electrode, respectively 110°C, 25 MPa and 5 min was found to be the optimal operating parameters for hot-pressing. Operating parameter optimisation led to a successful battery prototype assembly in three versions 1.2 V, 2.4 V and 12 V as a proof of concept.

**Keywords:** Energy Storage, Nickel-Iron Battery, Electrode processing, Bipolar electrodes, Bipolar battery stack development

# Acknowledgements

I wish to express my gratitude to:

- My Parents, Lassaad and Wahida, their never-ending prayers and their tremendous support from the very beginning, as well as my grandparents Hmed, Aycha, Hedi, Gamra; I am grateful and indebted to them forever.
- My sisters, Rim and Oumaima, for their support, love and motivation throughout this journey, it meant a lot.
- My soulmate Olfa, for her constant encouragement and relentless support. I am forever grateful for her support and love.
- My supervisor, Prof B.J. Bladergroen, for believing in me. His constant encouragement and guidance throughout this journey ensured that this project was a success. It was a privilege being a student of such a prominent Professor and a great mentor. He has assisted not only as my supervisor for this project but also granted me adequate opportunities to extend my knowledge related to this project.
- Energy Storage Innovation Lab (ESIL) for the financial support provided throughout the course of the study. For their love, encouragement, support and all the interaction that made my master's journey exciting.
- Mrs Denise Davids for all the efforts to ensure my administrative documentation were addressed timeously. Her support was the key and could not go unmentioned.
- Dr Anna Greve and Dr Jens Burfeind, for accommodating me at Fraunhofer UMSICHT and contributing to my research work ensuring that it reached its full potential.
- My friends and family for their love and support.

# Table of Contents

Table of Contents .....	5
List of Figures .....	7
List of Tables .....	9
Equation .....	10
List of Acronyms and Abbreviations .....	11
1 Introduction.....	14
1.1 Background on the growing demand for energy storage .....	14
1.2 Safe and cost-effective energy storage solutions .....	16
1.3 Problem Statement .....	17
1.4 Research Aims and Objectives .....	18
1.5 Overview.....	20
1.6 Significance of this Research.....	21
1.7 Thesis Layout.....	21
2 Literature review.....	23
2.1 Classification of Energy Storage Technologies .....	23
2.1.1 Mechanical Storage.....	23
2.1.2 Thermal Storage.....	28
2.1.3 Electrical Storage.....	28
2.1.4 Chemical Storage.....	29
2.1.5 Electrochemical Storage .....	31
2.2 Review of Nickel-Iron Batteries.....	38
2.2.1 History of the Alkaline Ni-Fe Battery.....	38
2.2.2 Basic Operational Principal of a Battery.....	38
2.2.3 Nickel-Iron Battery Components.....	39
2.2.4 Nickel-Iron Battery Characteristics.....	42
2.2.5 Negative iron Electrode .....	49
2.2.6 Positive Electrode .....	53
2.3 Ni and Fe Electrode Design and Construction.....	57
2.3.1 Types of Electrodes.....	57
2.3.2 Battery/Cell Design.....	60
2.4 Summary of Literature Review.....	63
3 Experimental Methodology .....	67
3.1 Development of a free-standing Ni-based Electrode .....	67
3.1.1 Material and Chemicals .....	67
3.1.2 Equipment and procedures used for the development of a free standing Ni-based electrodes .....	68

3.2	Development of bipolar electrode and fabrication process.....	70
3.2.1	The bipolar plate .....	71
3.2.2	Bipolar electrode optimisation .....	75
3.2.3	Bipolar electrode production for the battery stack .....	77
3.3	Bipolar battery stack assembly and testing .....	79
3.3.1	Laser welding .....	80
3.3.2	Bipolar Ni-Fe battery construction.....	83
3.4	Physical Electrode Material Characterisation .....	86
3.4.1	X-Ray Diffraction .....	86
3.4.2	Scanning Electron Microscopy .....	88
3.5	Electrochemical Characterisation of Electrodes .....	91
3.5.1	Cycling Voltammetry.....	91
3.5.2	Galvanostatic Charge/Discharge.....	95
4	Results and Discussion .....	101
4.1	The development of a free-standing Ni-based Electrode.....	101
4.1.1	X-Ray Diffraction results analysis.....	105
4.1.2	Scanning Electrode Microscopy analysis.....	108
4.1.3	Electrochemical Characterisation results .....	110
4.2	The development of the bipolar electrode and it's fabrication process.....	118
4.2.1	Pre-treatment results of the bipolar plates.....	118
4.2.2	Mould optimisation results.....	120
4.2.3	Hot-pressing optimisation results.....	121
4.3	The stack assembly and testing .....	126
5	Conclusions.....	133
6	Recommendations.....	134
	Appendix A: Definition of battery parameters .....	143
	Appendix B: Equipment used for the development of the electrodes.....	146
	Appendix C: Nickel electroplating of Cu current collector .....	149

## List of Figures

Figure 1: Estimated Renewable Energy Share of Global Electricity Production, End-2018 [3].....	14
Figure 2: Global Power Generating Capacity, by Source, 2008-2018 [3]. .....	15
Figure 3: Illustration of pumped hydro storage with the pumping energy supplied by wind turbines [21] .....	24
Figure 4: Illustration an earlier of compressed-air energy storage [31] .....	26
Figure 5: The flywheel storage system [36].....	27
Figure 6 : Classification of chemical storage systems (named technologies are only examples)[53] .....	30
Figure 7: Schematic overview of a redox flow cell energy storage .....	32
Figure 8: Schematic diagram of a typical electrochemical capacitor using high surface area carbon [49] .....	34
Figure 9:Cross section of Nickel-Iron battery [13] .....	41
Figure 10: Time-Voltage discharge curves of Nickel-Iron battery[60] .....	44
Figure 11: Ni-Fe typical voltage characteristics during constant-rate discharge[60] .....	44
Figure 12: Typical charging voltage for a Nickel-Iron battery at various rates[60] .....	45
Figure 13: Cycle life as a function of depth-of-discharge for a typical Ni-Fe cell[60].....	48
Figure 14: Correlations between capacity and discharge rates at 25°C[60] .....	48
Figure 15: Voltammogram curve with the redox peaks assigned to corresponding reactions [74].....	51
Figure 16:The Ni(OH) <sub>2</sub> layered crystal structure [64] .....	55
Figure 17:Bode diagram showing transformations among various phases of the nickel hydroxide [64].....	57
Figure 18: Pocket plate construction [65] .....	58
Figure 19: Nickel-Iron prismatic battery .....	60
Figure 20 : Schematic of Bipolar battery Construction [88].....	61
Figure 21 : Comparison of monopolar (A1) and Bipolar (A2) Lead-acid battery design [89] .....	62
Figure 22 : A1-Schematic of the conventional unipolar electrode structure (one-unit cell) Vs A2-Schematic of the bipolar electrode structure (two-unit cell) [90]. .....	63
Figure 23: Face 1 of the press mould Version 1 .....	69
Figure 24:Face 2 of the press mould Version 1 .....	69
Figure 25: Bipolar electrode configuration .....	71
Figure 26 : Bipolar plate roll and sheets in its commercial form [101] .....	72
Figure 27: Bipolar plate treatment with the plasma pistol .....	73
Figure 28: Two-point probe for conductivity measurements.....	74
Figure 29: Press mould Version 2.....	76
Figure 30: Dimensions of the bipolar Fe-based electrode .....	78
Figure 31: Dimensions of the bipolar Ni-based electrode .....	79
Figure 32 : Dimensions of the Freudenberg separator .....	80
Figure 33: Diode Laser welding machine .....	82
Figure 34: Exploded view drawing of BiNiFe Battery .....	84
Figure 35: Schematic of Ni-Fe bipolar battery construction process.....	84
Figure 36: Schematic illustration of bipolar Ni-Fe battery prototype production.....	85
Figure 37: Geometrical condition for diffraction from lattice planes[105] .....	87
Figure 38: Huber G670 Leaflet -XRD Powder diffraction .....	88



Figure 39: Schematic diagram of an SEM machine.....	89
Figure 40 : Steps of sample preparation for SEM analysis .....	90
Figure 41: JSM-7500F Field Emission Scanning Electron Microscope .....	90
Figure 42: Potential-time profiles generated during the linear sweep and cyclic voltammetry .....	91
Figure 43: Cyclic voltammogram plot analysis [107].....	92
Figure 44: ZENNIUM pro potentiostat / galvanostat[109].....	93
Figure 45: Power cell multiplexer PMux [109] .....	93
Figure 46: Experimental testing configuration for cycling voltammetry [108] .....	94
Figure 47: Schematic of the electrode configuration (Top view) .....	95
Figure 48: Different types of chronopotentiometry experiments: (a) constant current chronopotentiometry, (b) linearly rising current chronopotentiometry with linearly, (c) current reversal chronopotentiometry and (d) cyclic chronopotentiometry [110].....	96
Figure 49: Front panel of the IVIUM battery testing station .....	97
Figure 50: Schematic of nickel hydroxide colour change after the first charging process [111].....	102
Figure 51 : Ni-G1 electrode surface (a) before and (b) after the first charge .....	102
Figure 52 : Photos of the Nickel-based electrode surface after cycling (a) Ni-CB1, (b) Ni-G1 .....	103
Figure 53 : Discharge curves of Q-lite commercial electrode, Ni-G1 and Ni-G-Cu1 from 1.4 to 0.8 V at 100 mAh·g <sup>-1</sup> .....	104
Figure 54: Capacity loss measurements during cycling.....	105
Figure 55: XRD patterns of Ni(OH) <sub>2</sub> powders from Bochemie [112] .....	106
Figure 56: XRD patterns of charged and discharged Ni-G1 electrode in comparison with electrode material before the first charge.....	107
Figure 57: SEM images of Ni(OH) <sub>2</sub> Bochemie Powder (a) 300 nm scale, (b)1.2 μm scale [112].....	108
Figure 58: SEM micrographs of the same charged Nickel-based electrode at similar magnification .....	109
Figure 59: SEM micrographs of a discharged Nickel-based electrode .....	110
Figure 60: Typical cyclic voltammogram of a Ni(OH) <sub>2</sub> electrode at 4 different scan rates [117].....	111
Figure 61 : Cyclic voltammogram of Ni-G1 electrode .....	112
Figure 62: Activation cycling of Ni-G-Cu1 electrode at 100 mA between 1.6 and 0.8 V.....	113
Figure 63: Galvanogram of the Nickel-Iron cell during 20 cycles at 500 mA .....	114
Figure 64 : Typical two step discharge of the Nickel-Iron cell[124].....	115
Figure 65: Galvanostatic cycling of Ni-G-Cu1 electrode at 100 mA between 1.6 and 0.8 V.....	116
Figure 66 : Surface of a fresh Nickel-based electrode .....	117
Figure 67 : Photo of the Nickel-based electrode after cycling.....	117
Figure 68: CLSM results of a non-treated bipolar plate .....	119
Figure 69: CLSM results of a plasma-treated bipolar plate .....	119
Figure 70: Overall electrode thickness compared to the design requirements for batch 01 in which a SS frame was used.....	120
Figure 71: Overall electrode thickness compared to the design requirements for batch 02 in which a silicon frame was used, .....	121
Figure 72: Negative side of the bipolar electrode .....	126
Figure 73: Positive side of the bipolar electrode.....	126
Figure 74: Assembly diagram for the bipolar Ni-Fe battery .....	127
Figure 75: Upscale of Ni-Fe Battery prototypes .....	129
Figure 76: Galvanostatic cycling of the bipolar Ni-Fe battery prototype .....	130
Figure 77: Post-mortem photo of bipolar prototype Components .....	130

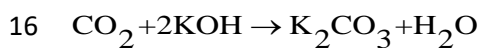
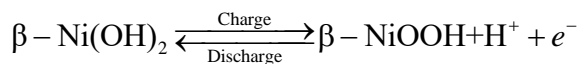
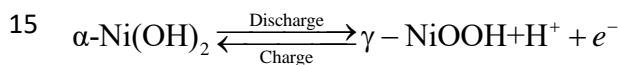
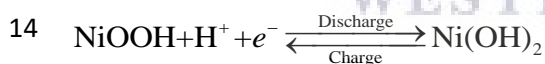
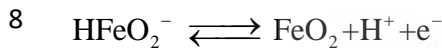
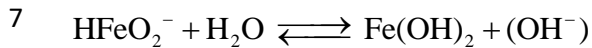
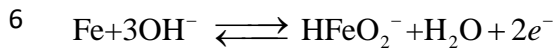
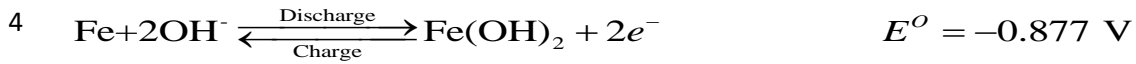
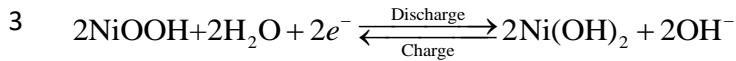
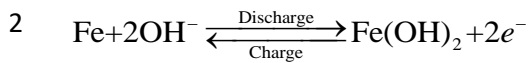
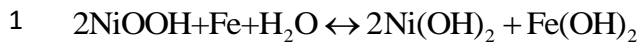


Figure 78 : Photo of the bipolar electrode cracks .....	131
Figure 79 : Photo comparison of battery separator (A) before and (B) After cycling .....	132
Figure 80: Hot-Press Polystat 300S .....	147
Figure 81: Polycontrol Interface .....	148
Figure 82: Vacuum oven BINDER VD 115 model [126].....	148
Figure 83 : Experimental setup for electroplating.....	152
Figure 84 : Before and after nickel electroplating .....	153

## List of Tables

Table 1: Comparison of different types of flow battery [33] .....	33
Table 2: Material and chemicals details .....	68
Table 3: Operating parameter for electrode hot pressing [100] .....	70
Table 4 : Nickel-based free-standing electrodes and their compositions.....	70
Table 5 : Bipolar plate specifications [101] .....	72
Table 6 : Influence of Hydraulic Pressure .....	75
Table 7 : Influence of Pressing temperature .....	76
Table 8 : Influence of Pressing time .....	77
Table 9 : Freudenberg separator specifications[104] .....	80
Table 10: Laser welding steps.....	82
Table 11 : Nickel electrodes composition and performance .....	101
Table 12: Swelling Measurement of various composite electrodes .....	116
Table 13: Initial electrode processing parameters and their impact on electrode properties .....	121
Table 14: Variation of pressing temperature and its impact on electrode properties .....	122
Table 15 : Variation of pressing time and its impact on electrode properties.....	123
Table 16: Variation of hydraulic pressure and its impact on electrode properties.....	124
Table 17 : Optimised pressing parameters .....	125
Table 18: Electrode specifications .....	128
Table 19: Technical Data Polystat 300S [93] .....	146
Table 20: Technical data of BINDER VD 115 model [126] .....	149
Table 21 : Time to electrodeposit nickel at various current densities .....	151

## Equation



$$17 \quad n\lambda = 2d \sin \theta$$

$$18 \quad \sigma = \frac{L}{\text{RWT}}$$

## List of Acronyms and Abbreviations

Ah	Ampere-Hours
CAES	Compressed Air Energy Storage
CC	Constant Current
CC_CV	Constant Current_Constant Voltage
CV	Cyclic voltammetry
DoD	Depth of Discharge
EDLC	Electrochemical Double Layer Capacitors
$E^0$	Standard potential
HER	Hydrogen Evolution Reaction
I	Electric Current
OER	Oxygen Evolution Reaction
SoC	State of Charge
SEM	Scanning Electronic Micrograph
ESS	Energy Storage System
U	Electric Potential
UOP	Over Potential
UOC	Open Circuit potential
PVDF	PolyVinylidene Fluoride
PtG	Power to Gas
SEM	Scanning Electron Microscopy
SMES	Superconducting Magnetic Energy Storage
XRD	X-Ray Diffraction
PEM	Proton Exchange Membrane
PTFE	PolyTetraFluoroEthylene
PSH	Pumped-Storage Hydroelectricity
LDPE	Low-Density PolyEthylene
FES	Flywheel Energy Storage

## Scientific Symbols

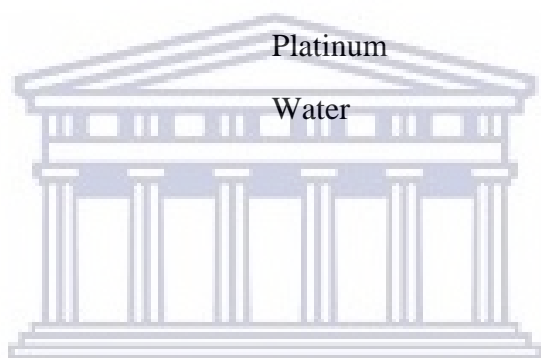
<b>Symbol</b>	<b>Description</b>	<b>Units</b>
$\theta$	Angle	°
$I$	Current	A
$E$	Energy	J
$\eta$	Energy Efficiency	%
$P$	Power	W
$R$	Resistance	$\Omega$
$V$	Voltage	V
$\lambda$	Wavelength	Hz



#### CHEMICAL SYMBOLS

$\text{Co(OH)}_2$	Cobalt(II) hydroxide
$\text{CuO}_2$	Copper(IV) oxide
Fe	Iron
$\text{Fe}^{2+}$	Ferrous iron
$\text{Fe}^{3+}$	Ferric iron
FeOOH	Iron(III) oxide-hydroxide
$\text{Fe(OH)}_2$	Iron(II) hydroxide
FeS	Iron(II) sulfide, troilite
KOH	Potassium hydroxide
LiOH	Lithium hydroxide
$\text{Na}_2\text{S}$	Sodium sulfide
Ni	Nickel

NiCd	Nickel-Cadmium
NiFe	Nickel-iron
Ni <sup>2+</sup>	Nickel(II) ion
Ni <sup>3+</sup>	Nickel(III) ion
$\alpha$ -Ni(OH) <sub>2</sub>	$\alpha$ -Nickel(II) hydroxide
$\beta$ -Ni(OH) <sub>2</sub>	$\beta$ -Nickel(II) hydroxide
$\beta$ -NiOOH	$\beta$ -Nickel(II) oxide-hydroxide
$\gamma$ -NiOOH	$\gamma$ -Nickel(II) oxide-hydroxide
NiMH	Nickel-MetalHydride
OH <sup>-</sup>	Hydroxyl anion
Hg/HgO	Mercury/Mercury Oxide
Pt	Platinum
H <sub>2</sub> O	Water



UNIVERSITY *of the*  
WESTERN CAPE

# 1 Introduction

## 1.1 Background on the growing demand for energy storage

Energy continues to be a key element in worldwide economic development. Due to the oil price wavering, diminishing fossil fuel reserves, climate change and pollution increases, geopolitical strains, and augmentation of energy demand, renewable energies and effective usage of fossil fuels have gained more attention and importance than at any time in history[1][2].

Fossil fuel markets are subjected to irregular price changes in both oil and natural gas. Energy and environmental contingencies are merging to inspire a dramatic pattern shift from fossil fuels to cleaner and/or more efficient energy sources. Using renewable energy sources seems a favourable option, their abundance, and environmentally friendliness makes them an attractive alternative. According to the global status report REN21[3], renewable energy continues its expansion in power generation share; nearly 181 GW was installed worldwide in 2018, where 90 countries already installed at least 1 GW of generating capacity including hydropower, also, 30 countries managed to exceed 10 GW of installed capacity[3].

As shown in Figure 1, generation using renewable energy is growing every year, mainly hydropower representing 60% of electricity production in the year 2018, followed by wind power with 21%, solar PV with 9%, and bio-power with 8%. Cumulative power capacity was sufficient to supply 26.2% of global electricity production.

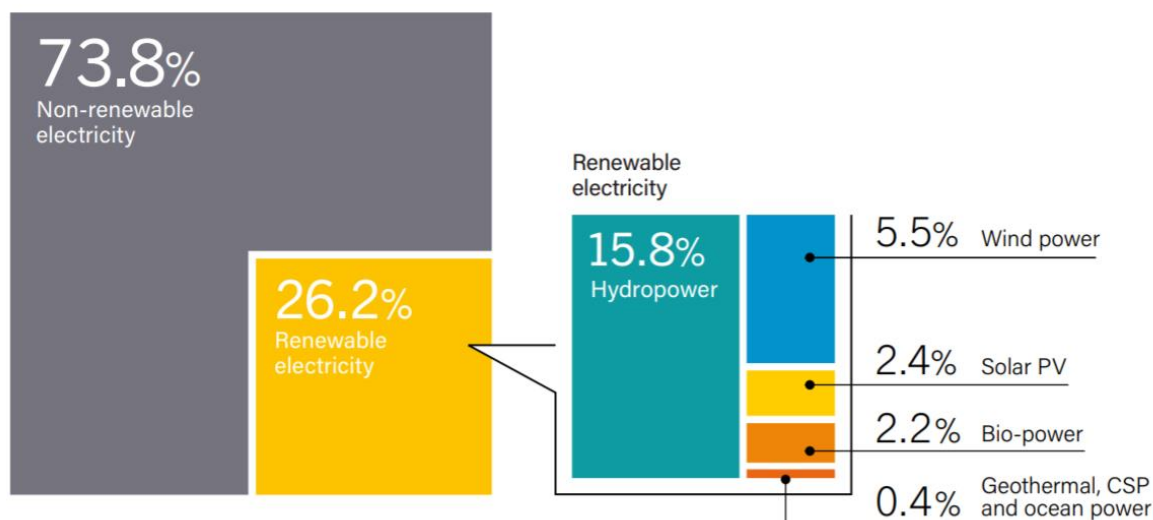


Figure 1: Estimated Renewable Energy Share of Global Electricity Production, End-2018 [3].

The same report indicated that China is leading the world in renewable energy generation capacity, followed by the United States, Brazil Germany, and India.

As shown in Figure 2 the global composition of installed renewable power capacity continued to shift during 2018 where hydropower represented close to 48%, wind power nearly 25%, and PV exceed 20%. Overall, renewable energy reached more than 33% of the global installed power generation capacity.

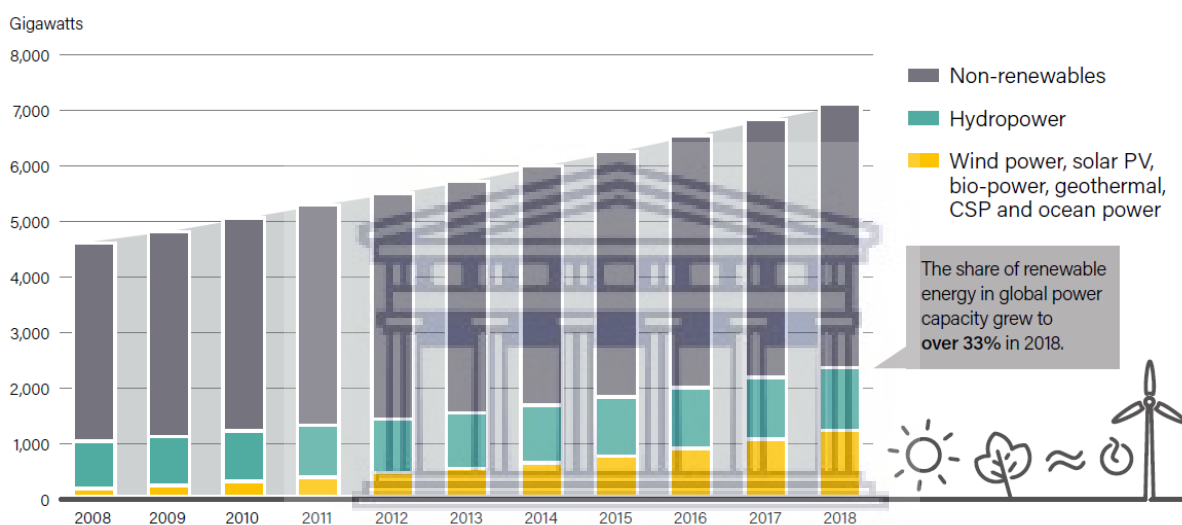


Figure 2: Global Power Generating Capacity, by Source, 2008-2018 [3].

However, there are serious challenges regarding some renewable energy sources and their implementation, such as their intermittency in power production [4][5].

Power generation from renewable energy resources such as wind and solar energies cannot be constant, because their production depends on multiple variables like the season and the time of the day.

Global research and development efforts focus on providing technological solutions and making these technologies a commercially viable option. Therefore, adopting renewable energy resources to become effective as primary sources of energy, the storage part is the crucial factor [6] [7].



Electricity is the most preferred form of energy for many applications. Electricity is transmitted over long distances and distributed to consumers by cable, but there is often the problem of matching the supply to meet the demand. This calls for the development of energy storage systems for the efficient storage of electricity [5].

Load levelling is another application when the storage of excess electricity generated meets the increased demand during the day [5]. Energy storage is also applicable to avoid the need for the part-loaded main plant which is held on standby to meet sudden demands, also, power emergencies which from the failure of generating units and/or transmission lines [8] [9]. Considering the wide range of applications, energy storage can be multi-beneficial to both utilities and their customers in terms of reducing primary fuel consumption through energy conservation and improved systems operation efficiency, providing security of energy supply, and reducing environmental impact. Storing the energy during low energy demand and then discharging it during the peak energy demand can overcome existing obstacles. The integration of renewable energy and energy storage enables efficient energy generation.

Several energy storage techniques are widely utilised, these include mechanical, thermal, electrical, chemical, and electrochemical techniques [3]. Electrochemical energy storage offers an attractive solution that would help balance the electrical energy grid by mitigating the sporadic impediment between energy generation and demand chiefly due to its high round-trip efficiency, long cycle life, low cost, and scalability [3].

## **1.2 Safe and cost-effective energy storage solutions**

Many battery technologies have been developed but only a few have been demonstrated in large-scale applications. Among the various developed battery technologies, aqueous batteries have the potential to aid in balancing the future electrical energy grid at a lower cost than any of their non-aqueous counterparts such as Li-ion, Na-ion, etc. Aqueous batteries consist of globally abundant raw materials and low-cost aqueous electrolyte solutions. Non-aqueous batteries require a costly safety system to minimise the risk of thermal runaways and explosions [10].

The lead-acid battery is a mature technology, its energy density is 35 to 40 Wh·kg<sup>-1</sup>, the toxicity of raw materials corrosiveness of the electrolyte, and short cycle life limit its potential as an ideal renewable energy storage technology candidate [11]. In comparison, Nickel-Iron (Ni-Fe)

cells were invented and commercialised in the early 20th century, and could potentially deliver 2 to 3 times the specific energy of Pb-acid batteries they have long cycle life and deep. surpass 15000 cycles of charge and discharge, they surpass most of their competing battery technologies Where Lead-acid has 300-400 cycles, Ni-MH has 500–800, and Ni-Cd (1300-1600 cycles) [11].

Increasing efforts are in progress to develop cost-effective, highly efficient energy storage technologies. Ni-Fe cells are secondary batteries that are well known for robustness, non-toxicity, and eco-friendliness [12][13]. The relative abundance of chemicals and raw materials required to build these batteries signify that this battery technology could provide a cost-effective solution to store energy for electricity grid system applications. However, the successful commercial deployment of these batteries has been blocked by their poor coulombic efficiency (40–60%), low discharge rate capability, and low specific energy ( $\sim 50 \text{ Wh}\cdot\text{kg}^{-1}$ ) [14].

The main drawbacks were identified being the parasitic reaction of the hydrogen evolution taking place on the Iron-based electrode during charging, also the passivation happening during the discharge of the iron electrode due to an insulating layer of iron oxides [14][15]. When Nickel-based electrodes are charged for prolonged periods the  $\beta$ -NiOOH is converted to  $\gamma$ -NiOOH and causes irreversible damage to the electrode due to the accompanying mechanical deformation [16]. The Fe-based electrode and the Nickel-based electrode influences the overall electrochemical performance of the Ni-Fe battery, therefore, by modifying the electrode's material composition, design, nanostructure, and production methods, the battery's overall performance will potentially improve [15].

The use of industrial-grade material with an optimised composition of the nickel electrode could potentially inhibit the swelling during cycling the inclusion of graphite could provide a good conductive network improving the reversibility of the active material and could optimise the porosity of the electrode. The electrode can be integrated into a bipolar design. Such a low-cost design saves up to 80% of conventional battery materials in areas such as electrolytes, insulating sheets, and cables.

### 1.3 Problem Statement

The implementation of renewable energy systems as part of the energy supply is facing some challenges, which are caused by the intermittent nature of renewable energy sources.

Accordingly, storing energy for later use becomes of paramount importance. Producing a stable, robust, low-cost, environmentally friendly, and efficient energy storage system is then the main challenge.

A rechargeable battery allows storage of electrical energy as chemical energy, which can be used reversibly through redox-reactions. Rechargeable batteries together with a renewable energy generation technology are a step towards a green future with a low carbon footprint.

During the last decade, the search for a low-cost stationary energy storage system has led to a renewed focus on the Ni-Fe battery. The Ni-Fe battery is well-known for its robustness and long life. Nevertheless, the Ni-Fe battery suffers from severe drawbacks, mostly induced by the negative electrode, which exhibits low efficiency and low specific energy. Besides, expensive production methods are currently employed for electrode production. These drawbacks block existing Ni-Fe battery technology from being a viable energy storage alternative.

Developing a Nickel-based composite electrode with optimised conductivity and porosity using graphite for the alkaline Ni-Fe battery storage system for renewable energy might contribute to addressing these drawbacks.

The development of suitable electrodes with optimised production techniques using bipolar plates in a bipolar Ni-Fe battery design is the challenge addressed in this work in order to enhance the performance of the alkaline Ni-Fe battery as a storage system.

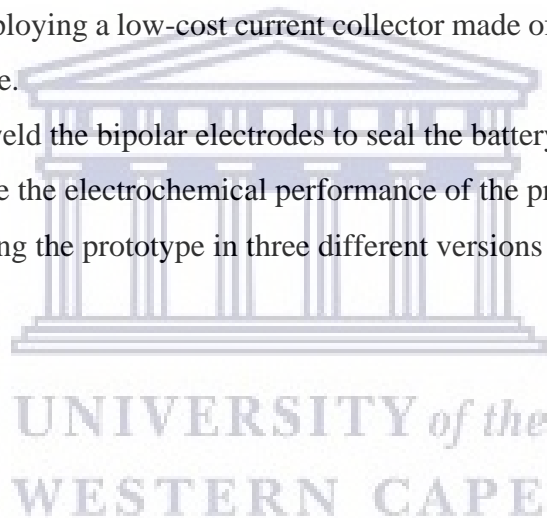
#### **1.4 Research Aims and Objectives**

The main aims of this research were to develop, optimise, and test the overall performance of a Ni-Fe battery prototype. A literature review revealed that a significant cost saving can be achieved when a bipolar battery design is considered.

To achieve the aims, the following objectives and sub-objectives were addressed.

- A suitable production technique must be developed to achieve the formation of bipolar electrodes
  - Operating parameters such as pressure, temperature and time to be optimised to achieve reproducible bipolar electrodes while hot-pressing.

- Appropriate additives must be considered to reach desired electrode performance characteristics
- Compare the effect of using carbon black and/or graphite on the mechanical stability of the produced electrode, and swelling observations on electrode surfaces after cycling.
- Characterise the electrodes by X-ray diffraction analysis, scanning electrode microscopy, cyclic voltammetry, and galvanostatic charge and discharge test.
- Determine the optimum composition of the positive electrode and construct a bipolar Ni-Fe battery prototype using industrial-grade electrode materials.
- Construction of a battery stack
  - Produce composite electrodes by using low-cost hot-pressing techniques and employing a low-cost current collector made of the conductive polymer substrate.
  - Laser-weld the bipolar electrodes to seal the battery prototype.
  - Evaluate the electrochemical performance of the prototype battery.
  - Upscaling the prototype in three different versions as a proof of concept.



## 1.5 Overview

The current study forms part of a larger collaborative effort to commercialise low-cost NiFe batteries. Two collaborators are based in Germany (Fraunhofer UMSICHT and Volterion) and two are based in South Africa (UWC and Connect'd Energy). It was Connect'd Energy who identified NiFe as a potential candidate for low-cost energy storage. Connect'd Energy approached Fraunhofer and UWC to conduct a short preliminary research study. Soon thereafter, research proposals were submitted and eventually funded by both the German government, the Department of Science and Innovation (DSI) of South African, and the South African electricity utility Eskom.

There were 4 students involved in this project, each of them with a specific research task to focus on:

- Development of Fe based electrode by Mr Tendai Tawonezvi, Master student
- Development of Ni based electrode by Miss Dorcas Zide, PhD student
- Development of a bipolar NiFe electrode by Mr M Ali Ben Ltaief (this study). This development included some optimisation of Ni and Fe electrodes in parallel to the work of the other students)
- Development of the bipolar NiFe electrode stack welding by Mr Lucas Welhim , PhD student at Fraunhofer UMSICHT.
- Trouble shooting battery stack assembly and testing by Mr M Ali Ben Ltaief (this study).

Volterion is a company that spun out of Fraunhofer UMSICHT in 2008 and currently produces redox flow batteries for the commercial energy storage market. The company is a world leader in welded battery stacks but has no experience with the production of NiFe batteries. Fraunhofer UMSICHT owns background IP on the manufacturing of so called “bipolar plates”, graphite loaded polymer film, and has know-how on laser-welded stacks. UWC and in particular the South African Institute for Advanced Materials Chemistry (SAIAMC) has significant experience with the development of batteries, particularly Li-ion batteries and Na-NiCl<sub>2</sub> batteries. Connect'd energy is part of the collaboration as a commercialisation partner of the NiFe battery technology when meaningful prototypes can be produced

The current study does not focus on the optimisation of the anode material, since it was tasked to a fellow co-worker in the project to investigate it, but rather on the cathode optimisation and the electrode manufacturing methods, optimisation of manufacturing process conditions and electrode testing, specifically with the aim to make a prototype NiFe bipolar battery.

## 1.6 Significance of this Research

A cost-effective energy storage system could play a critical role in humanity's efforts to decarbonise the world economy and reduce its dependence on fossil fuel consumption. The envisaged development of a bipolar Ni-Fe battery prototype aims to reduce the overall cost of battery construction and to increase the energy storage efficiency, which is both needed to make these batteries economically viable.

Other significant aspects of this study include the generation of knowledge in the field of electrochemical energy storage, potential job creation when commercially viable prototypes can be demonstrated, and local mineral beneficiation. Implementation of this product may assist to solve the renewable energy storage challenges.

## 1.7 Thesis Layout

The outline structure of this thesis is described under the chapter headings that follow:

### **Chapter 1 – Introduction:**

The introduction chapter gives an insight into the research and provides background information on energy storage and an overview of the potential improvements that are currently under investigation. Background on bipolar Nickel-Iron batteries being the focus of this research and its utilisation in grid-scale energy storage applications are discussed. The overall aims and research objectives are also identified and explained in this chapter.

### **Chapter 2 - Literature Review:**

The literature review provides the background information required to gain a proper understanding of the fundamental principles that are applied in this research starting from the

identification of the gaps in the overall existing energy storage technologies all the way to the details of the Nickel-Iron battery. Bipolar Nickel-Iron battery development is the focus of the review; however, additional sections related to Nickel-Iron battery construction have also been featured briefly to allow for connections to the overall concept to be made easily. Fundamental understandings of Nickel-Iron battery bipolar design and components, testing protocols required to validate this study have also been covered and presented.

### **Chapter 3 – Experimental Methods:**

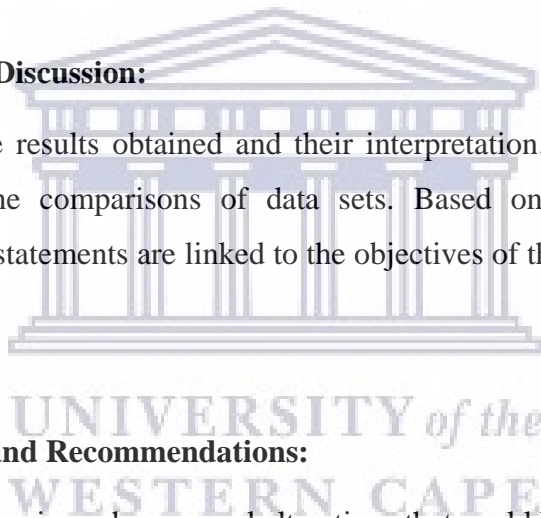
This chapter describes the materials and experimental methods used in this research. All the techniques, programs, and equipment are detailed and presented clearly to explain how the literature information was employed in practice to solve the research problem.

### **Chapter 4 – Results and Discussion:**

This chapter describes the results obtained and their interpretation. The investigations and discussions also cover the comparisons of data sets. Based on these discussions and examinations, concluding statements are linked to the objectives of the research mentioned in Chapter 1.

### **Chapter 5 – Conclusion and Recommendations:**

Chapter 5 summarises the various changes and alterations that could be implemented. Recommendations based on the research, are made in terms of future research work in the area of energy storage systems development.





## 2 Literature review

The literature review provides background information on most energy storage technologies (section 2.1) to provide the appropriate context for this study. Section 2.2 focuses specifically on Nickel-Iron batteries including their origin, their main operational principles, characteristics, and battery components. Section 2.3 discusses battery design and construction followed by the literature review summary giving guidance to the experimental work in Chapter 3.

### 2.1 Classification of Energy Storage Technologies

An energy storage system is defined as an installation, subject to independent control, with which it is possible to store energy generated and consumed it when needed [9] [17]. Energy storage can optimise existing generation and transmission infrastructures whilst also preventing expensive upgrades.

Different energy storage technologies coexist because their characteristics make them attractive to different applications. In general, energy storage systems can be described as either electrical or thermal [18] [19].

Energy storage systems include a broad range of technologies, which either directly or indirectly can provide electrical energy storage via an electrical input and output. The principal technologies are:

- Mechanical Storage (see section 2.1.1)
- Thermal Storage (see section 2.1.2 )
- Electrical Storage (see section 2.1.3)
- Chemical Storage (see section 2.1.4)
- Electrochemical Storage (see section 2.1.5)

#### 2.1.1 Mechanical Storage

##### 2.1.1.1 Pumped hydro storage (PHS)

Pumped hydro storage technology uses the power of water, considered as a concentrated renewable energy source. Currently, it is one of the most appropriate technologies for high-power and energy applications with an energy output rating from 500 to 8000 MWh and a power rating from 10 to 1000 MW[4].

In principle, during low energy demand periods, electricity is supplied to pump the water from the lower reservoir to the upper reservoir as shown in Figure 3. The water flows gravitationally from the upper reservoir activating the turbines to generate the electricity needed for high-demand periods.

The conversion efficiency of such a system is between 65 to 80%, depending on the characteristics of the equipment installed [20]. In most cases, 4 kWh is consumed to generate 3 kWh. The height of the waterfall and the volume of water govern the storage capacity. By approximation, 1 ton of water flowing down 100 m can generate 0.272 kWh. This technology has been used to store huge amounts of electricity but one of the main drawbacks is the specificity of such a site considering the location and the different water elevations [20].

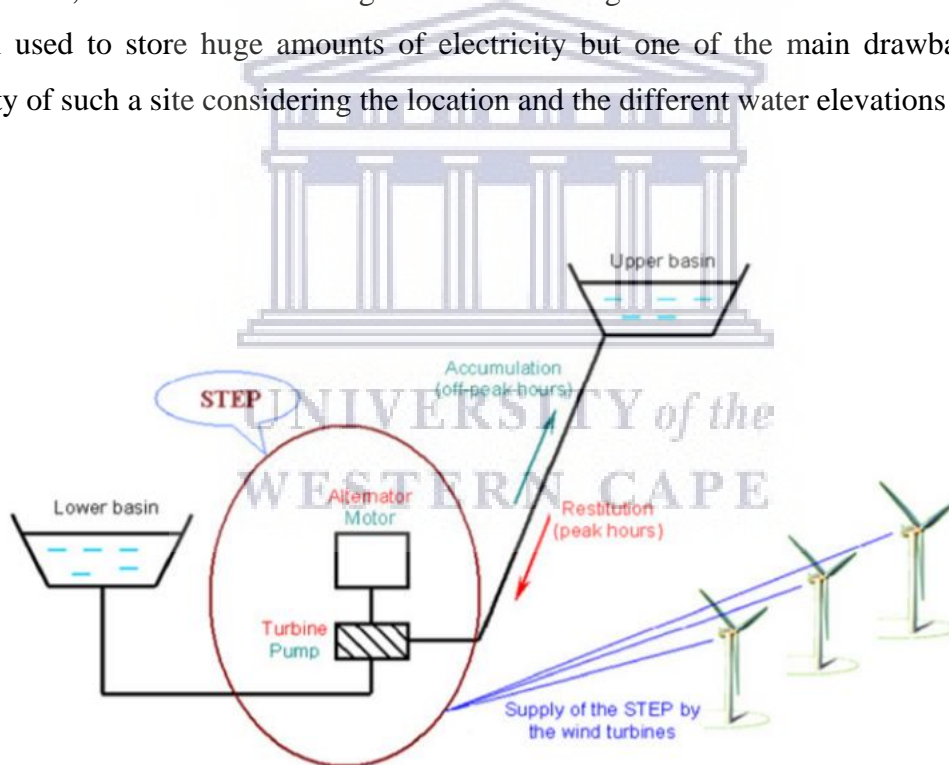


Figure 3: Illustration of pumped hydro storage with the pumping energy supplied by wind turbines [21]

Generation and pumping can be accomplished either by single-unit, reversible pump-turbines or by separate pumps and turbines. The switch between pumping and generating can occur within 60 to 90 seconds. Depending on the installation, such changes occur once or twice to more than 40 times daily. Flooded mineshafts or other natural cavities, are technically possible to use for underground pumped storage. In other cases, the open sea can be used as the lower

reservoir [22]. With about 300 systems operating worldwide, pumped hydro-storage is considered as a low-cost, environmentally friendly, scalable energy storage system [23].

According to Dursun and Alboyaci [24], running pumped hydro storage systems can be divided into 24 h time-scale applications and could be extended for longer energy storage time, even for several days. However, the construction and application of this system result in the ecosystem and environmental damage, loss of land, water loss (through mass evaporation), and toxic methane gas emissions and is marked with associated failure risks and geographic and meteorological limitations [25]. In practice, PSH reported round trip energy efficiency ranges between 75% and 85%, with some reaching up to 88%. Overall, the lifetime of PHS is approximately 30–50 years, and power capital costs of 500–1500 Euro/kW and 10–20 Euro/kWh [26]. PSH energy storage technology is flexible, relatively low costly, suitable for industrial applications, and prompt reduced carbon dioxide emissions. However, this system results in ecosystem and environmental damage, loss of land, water loss (through mass evaporation), and toxic methane gas emissions [27] [28].

#### 2.1.1.2 Compressed air energy storage (CAES)

In this storage system, energy is stored by compressing the air within a reservoir, putting in service a compressor powered by a low-cost electric energy source [29] [30].

A particular design is essential to allow the turbine to operate in two directions, one for charging and one for discharging as shown in Figure 4. Three types of reservoirs are generally considered; naturally occurring aquifers similar to those used for natural gas storage, salt caverns, and mechanically formed reservoirs in rock formations. The turbine turns the alternator, which generates electricity. Currently, the use of CAES is still limited. Only two plants have been established in the world, one in the USA built-in 1991 (110 MW) and the other in Germany built-in 1978 (290 MW) [31]. The energy density of this storage system is around  $12 \text{ kWh}\cdot\text{m}^{-3}$  [32], the system efficiency is roughly 70% and the lifetime is nearly 40 years [33]. The costs of construction depend on the underground storage conditions, extending typically between \$1950 and 2150 per kW and approximate LCOE of \$390-430 kWh [34].

Taking into consideration the low self-discharge rates, CAES is considered a long-term time scale storage option, which can compete with PHS. CAES and PHS are the only existing technologies that are currently suitable for large-scale power and high-energy storage applications. However, various features make CAES very distinct from PHS. The capital cost

of CAES is remarkably lower and thanks to its underground structure, there is a low impact on the surface environment [35]. CAES is based on a relatively mature technology with several high-power projects under construction.

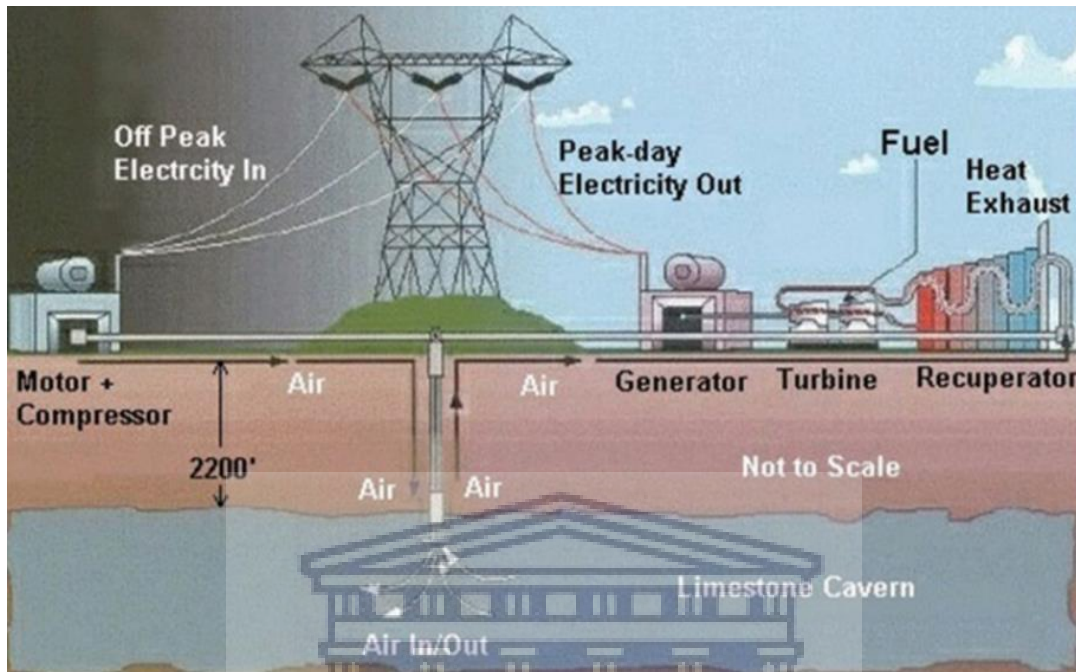


Figure 4: Illustration an earlier of compressed-air energy storage [31]

Compressed air energy storage is accomplished at high pressures ranging from 40 to 70 bars, at near-ambient temperatures. This contributes to less volume and a smaller storage reservoir. Large caverns made of high-quality rock deep in the ground, ancient salt mines, or underground natural gas storage caves are the best options for compressed air storage, as they benefit from geostatic pressure, which facilitates the containment of the air mass. A large number of studies have shown that the air could be compressed and stored in underground, high-pressure piping (20–100 bars) [31].

### 2.1.1.3 Flywheel energy storage (FES)

Flywheels have been in existence for centuries, however, over the past few decades they have been considered as tools for bulk energy storage. High efficiencies for short durations of storage have been achieved through recent developments with optimisation in design.

As shown in Figure 5, the entire system is placed in a vacuum to reduce wind shear [36]. Flywheels store energy via the rotating discs as kinetic energy from their angular momentum. During the charging operation energy is supplied to run a motor which increases the speed of

the flywheel. This flywheel remains spinning until the energy is needed. During discharge operation, the speed of the flywheel decreases, transferring energy to the outer circuit.

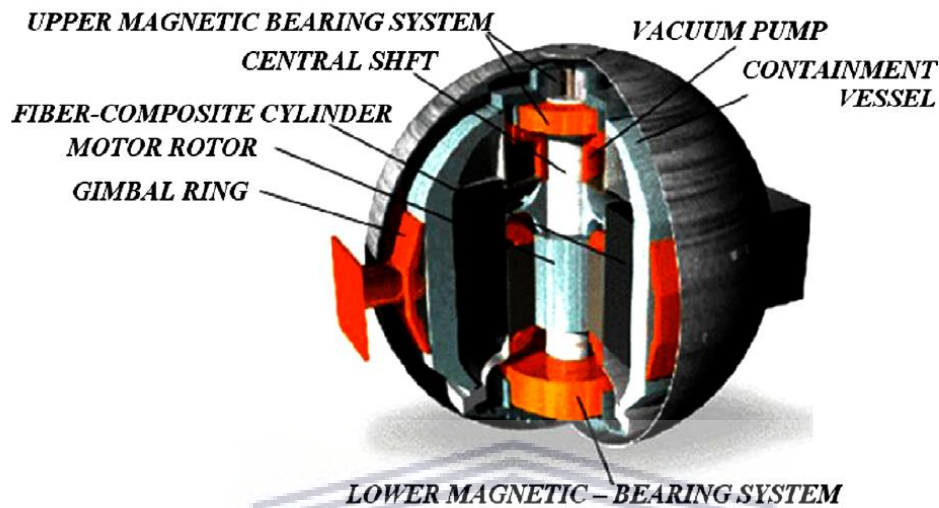


Figure 5: The flywheel storage system [36]

Among the important aspects of flywheel design, are the bearings that hold the shaft that connects the device to the motor and generator in place while allowing for rotation. Mechanical bearings create friction, and that friction is inevitable even in the best design, which results in energy loss as the flywheel spins. The recent optimisation efforts regarding the design were replacing the mechanical bearings with magnetic ones, which significantly reduce frictional losses, and thereby the self-discharge. These devices are categorised into low-speed and high-speed designs, the low-speed designs are 10,000 rpm or less, and are usually made of heavy steel discs. The shaft is either vertical or horizontal and may have mechanical or magnetic bearings. The high-speed designs operate above 10,000 rpm, some can reach 100,000 rpm. Due to the high speeds, and associated fatigue failure risks, stronger materials are required, including composites of graphite or fiberglass [36].

The energy efficiency of flywheels is around 90%. However, the main drawbacks of flywheels are the high energy costs ranging from \$1000 to 5000 per kWh,[37], and the high frictional losses leading to self-discharge rates of flywheel systems, with a minimum rate of 20% of the stored capacity per hour. Among flywheel, applications are the provision of power when there is a total power loss as a result of electricity grid failure [8].



## 2.1.2 Thermal Storage

Thermal energy storage (TES) consists of storing heat energy using high specific heat capacity materials. Various technologies fall under the thermal energy storage category, such as latent heat energy storage, sensible heat storage, and adsorption/absorption thermochemical sorption via thermo-chemical sorption [38] [39]. Absorbing and retaining the heat for several hours and even days and then delivering it when the energy input is low for systems in applications such as air-conditioning or solar thermal heating. There are two types, low-temperature thermal energy storage (LTTES) and high-temperature thermal energy storage (HTTES) [40]. LTTES has a temperature application range of less than 200 °C, it could be useful in a different range of applications such as solar water boilers, building air-conditioning, solar cooking, and solar greenhouses [41] [42] [43]. High-temperature thermal energy storage, where the temperature range exceeds 200 °C, offers a key role in renewable energy integration technologies mainly in waste heat regeneration, metallurgical, mining industry, and construction materials production [44] [45].

Latent heat energy storage is accomplished by exploiting phase change materials (PCMs) as energy storage mediums such as various salt hydrates (Inorganic materials) and paraffin (Organic materials). This type of TES takes place without temperature shifts during energy transitions [46]. It was reported that TES systems have a low round-trip efficiency of over 55%, and a capital cost of around \$350 to 450/kWh due to its large size storage system occupying a large space, engendering a higher and causing large thermal losses [47].

## 2.1.3 Electrical Storage

### 2.1.3.1 Capacitors and super-capacitors

A capacitor (formerly known as a 'condenser') is a passive electrical component that can electrostatically store energy in an electrical field.

The configuration of capacitors varies widely, but all constitute at least two electro-conductive plates separated by a dielectric sheet (i.e., insulator). A capacitor can retain electrical energy when disconnected from its charging device, so it can temporarily act as a battery or any other energy storage technology. Capacitors are widely applied in electronic devices to sustain constant power supply whereas charge fluctuates in electrochemical batteries, this avoids

information loss in volatile memory [48]. Capacitors have extremely fast response time, high round trip energy efficiency (>70%), and essentially unlimited cycle lifetimes, however, the energy capacity is limited, typically can store less than  $0.1 \text{ Wh}\cdot\text{kg}^{-1}$ . In light of this, they consequently pose a limited role in applications where significant energy amounts need to be stored [48] [49].

### 2.1.3.2 Superconducting Magnetic Energy Storage

Superconducting magnetic energy storage systems (SMES) store energy in a magnetic field generated by the unidirectional flow of an electric charge in a coil composed of a superconducting wire that has been cryo-cooled to a temperature level below its critical superconducting temperature [50]. The electric charge does not decay when the superconducting coil is fully charged, implying that the magnetic energy can be stored indefinitely. The capacity (maximum storable energy) is determined by the dimensions and geometry of the superconducting coil, these parameters also determine the inductance of the coil. The magnetic energy stored is discharged by the superconducting coil via a direct current (DC) to alternating current (AC) conversion process enacted by a power inverter. The integrated power rectifier/inverter accounts for approximately 1–3% energy loss during either the charge or discharge process [51]. SMES systems lose the least amount of energy during the discharge process compared to other energy storage technologies thereby actuating a round-trip efficiency ranging from 80 to 90% [52]. However, SMES systems have a very high-power density ( $10 - 10^4 \text{ W}\cdot\text{kg}^{-1}$ ) but discharge that energy in a very short period, prompting a device with low energy density ( $1-2 \text{ Wh}\cdot\text{kg}^{-1}$ ) [50]. The limitation of this technology resides in its high cost, mainly due to the cost of the superconducting wire and the refrigeration energy requirements. SMES are limited to high-power and short duration applications such as frequency control, voltage control, and peak shaving [52].

## 2.1.4 Chemical Storage

### 2.1.4.1 Power to Gas

Chemical storage systems can be classified into systems with internal and external storage. As shown in Figure 6 storage systems with external storage have the advantage that energy content and power capability can be designed separately.



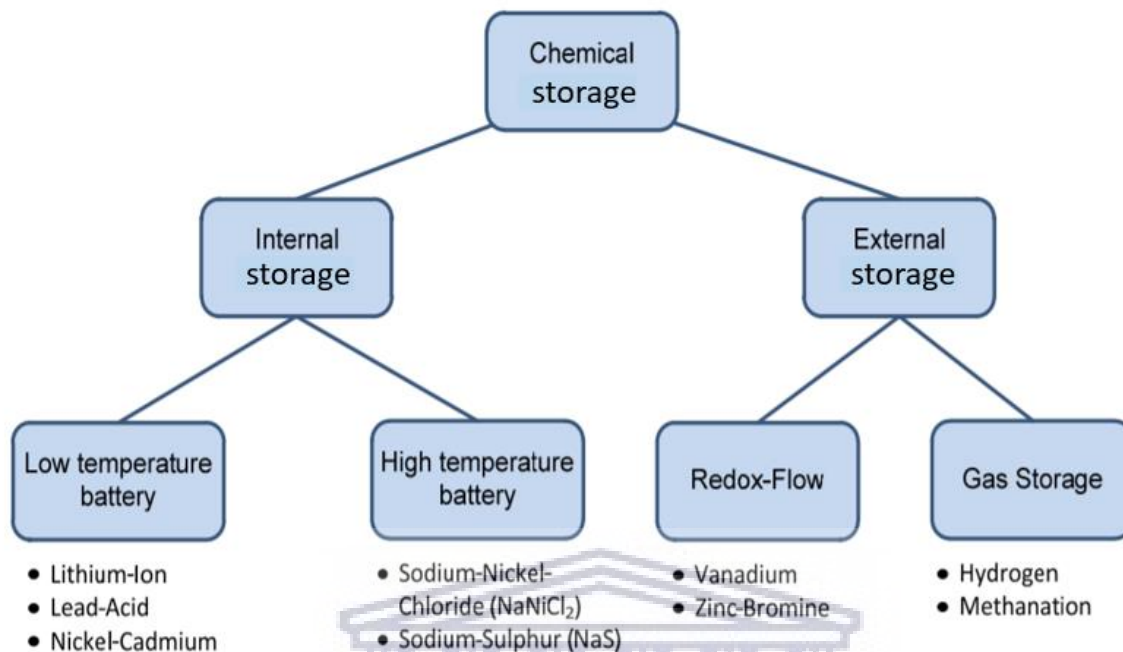


Figure 6 : Classification of chemical storage systems (named technologies are only examples)[53]

Power to gas (PtG) is a process that converts electrical power into gaseous energy-rich fuels such as carbon-neutral methane through methanation process or hydrogen through electrolysis. Three water electrolysis technologies are widely utilised to produce hydrogen namely alkaline electrolysis, proton exchange membrane (PEM) electrolysis, and solid oxide electrolysis. Alkaline electrolysis is at present the most economical process; in the future, however, PEM electrolysis could be a better fit for the gas process chain. Solid oxide electrolysis could also be a suitable option in the future, especially if there are vast heat sources available [53].

Three PtG technologies are widely utilised. The first PtG method involves the injection of hydrogen into the natural gas grid to utilise it in transportation or industry. The second PtG method comprises the reaction of hydrogen with carbon dioxide to yield methane via a methanation reaction (such as the Sabatier reaction), or biological methanation, which results in an extra energy conversion loss of approximately 10% [53][54] [55].

The methane may then be fed into the natural gas grid. The third PtG method utilises the output mixed gas (primarily methane and carbon dioxide) of a wood gasification unit (wood gas

generator) or a biogas plant after biogas is mixed with the hydrogen (from the electrolyser) in the biogas upgrader to upgrade the quality of the biogas. However, the technology has negative environmental implications (CO<sub>2</sub> emissions), low round-trip efficiency (<55%) and entails high economic costs with a capital cost ranging from 950 to 1100 \$/kWh. These factors will limit its wide implementation soon [55].

## 2.1.5 Electrochemical Storage

An energy storage technology that is receiving intensive attention is electrochemical energy storage. In the context of multidimensional challenges, electrochemical energy storage (EES) technology is a feasible solution.

### 2.1.5.1 Redox Flow Battery

A redox flow battery (RFB) operates by circulating an electrolyte solution over an ion-selective membrane where ions are exchanged to discharge or charge the battery. For various applications, cell voltage varies from 1.1 to 2.5, as is electrochemically determined by the Nernst equation. The energy storage capacity of a typical RFB is regulated by the volume of the tanks housing the electrolyte solution [56] [57]. The 2003 report highlighted that the term “redox” refers to the electrochemical reduction and oxidation reactions that transpire in the RFB to store energy in the liquid electrolyte solution. During the discharge process, an electron is released to the external circuit via an oxidation reaction from a high chemical potential state on the negative electrode or anode lateral of the battery. The electron travels through an external circuit simultaneously discharging energy through executing work. Ultimately, the electron is accepted on the positive electrode or cathode lateral of the battery via a reduction reaction at a lower chemical potential state. The trajectory of the current and the chemical reactions is reversed during charging [57]. RFB is considered to be an electrochemical battery and fuel cell. Commercial RFB technologies are designed for long half-cycle energy storage such as power sources for backup grids. The vanadium redox flow battery (VRFB) is the most technologically advanced system, it has been piloted since the 1990s by corporations such as Cellstrom (Australia) and Prudent Energy (Canada) [58]. The diffusion of metal ions through the ion-selective membrane cannot be halted (as is the case for most RFB), resulting in loss of energy. In other RFB systems, which utilise different metals ions for anolyte and catholyte, the crossover fosters irreversible electrolyte degradation and capacity loss.

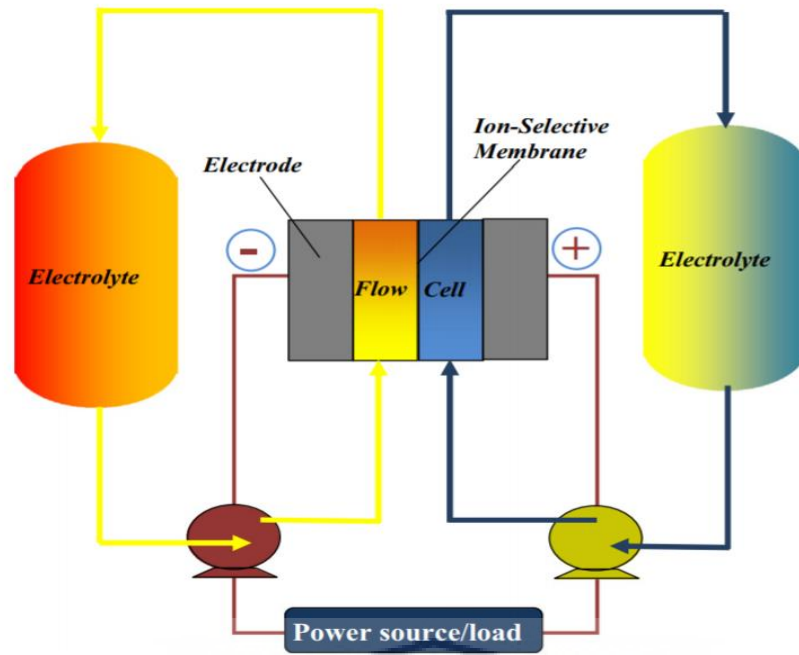


Figure 7: Schematic overview of a redox flow cell energy storage

Figure 7 illustrates a schematic design of a typical redox flow battery system. Redox flow batteries, especially vanadium redox flow batteries, and hybrid flow batteries to a lesser extent, offer a versatile layout advantage (attributed to detachment of the power and energy elements), long cycle life (due to absence of solid-to-solid phase transitions), fast response times, no need for "charge equalisation" of the battery (overcharging of a battery to ensure that all cells contain equal charge) and no hazardous gas emissions [59]. They also offer a simplified determination of state-of-charge (via voltage dependence on charge), require sparse maintenance, and tolerant to electrochemical abuse (overcharge/over-discharge). In comparison with rechargeable batteries (such as Li-ion), RFBs, and aqueous RFBs, in particular, can operate effectively at higher power and current densities [58]. These technical merits propel redox flow batteries to qualify as a pertinent option for large-scale energy storage. Flow batteries also operate at considerably lower efficiency (60-80%) relative to non-reversible fuel cells or electrolyzers utilising identical electrolytic chemistries. The development and economics involved in upscaling from pilot scale to industrial scale is an ongoing process. The high cost of stack components such as end plates, bipolar plates, seals, and membranes are the most prominent impediments faced by this technology.

Three types of flow batteries were able to reach the commercialisation stage, these types are vanadium redox battery (VRB), Polysulphide Bromide Batteries (PSB), and zinc-bromine battery (ZnBr). Table 1 presents important characteristics of these technologies, where VBR performs better than PSB and ZnBr as they have low capacities and low cycle life, with noticeable better efficiency for the VBR.

Table 1: Comparison of different types of flow battery [33]

Technology	VRB	PSB	ZnBr
Efficiency (%)	85	75	75
Cycle life charge/discharge	13,000 (12,000+)	-	2500 (2000+)
Capacity (MW)	0.5–100	1–15	0.05–1 (0.05–2)
Operation temp. (°C)	0–40	50	50
Energy density (Wh·kg <sup>-1</sup> )	30 (10–30)	-	50 (20–50)
Self-discharge	low	low	low

#### 2.1.5.2 Electrochemical Super-capacitor

Supercapacitors, also known as electric double-layer capacitors (EDLC) or ultra-capacitors are universal terms for a group of electrochemical capacitors that do not possess conventional solid dielectrics. Capacitance is regulated by two storage concepts, double-layer, and pseudocapacitance. Storing energy in a super-capacitor takes the form of an electrical field between two electrodes, which is similar to what happens inside the capacitors, the difference though resides in replacing the insulating material with an ionic conductor usually an electrolyte that offers a large specific surface and facilitates the movement of ions [49].

The existing gap between rechargeable batteries and conventional capacitors is bridged by super-capacitors. Electrochemical capacitors have the highest specific energy or energy density (can store the highest energy per unit of mass or volume) among capacitors. They can deliver up to 11,500 farads/1.2 volts, up to 11,500 times more than that of electrolytic capacitors, but deliver or accept less than half as much energy per unit time (low power density). The technology has high round energy efficiency (>90%) [49].

Although super-capacitors offer energy densities of approximately 10% of standard conventional batteries, their power density is typically 20 to 200 times greater. This results in

much-shortened charge and discharge periods. Additionally, electrochemical supercapacitors tolerate many more electrochemical cycles than standard conventional batteries [49].

Super-capacitors exhibit extremely fast responses (very short response timeframes) and essentially unlimited electrochemical cycle lifetimes but store very little energy per unit of mass, typically less than  $0.1 \text{Wh}\cdot\text{kg}^{-1}$  and they thus have limited applications where significant amounts of energy need to be stored [49].

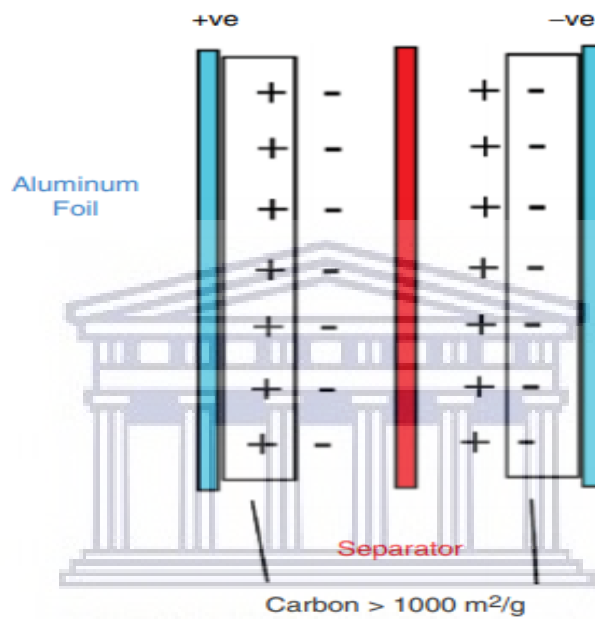


Figure 8: Schematic diagram of a typical electrochemical capacitor using high surface area carbon [49]

### 2.1.5.3 Traditional Rechargeable Batteries

A rechargeable battery is made of one or more reversible electrochemical cells. They are called secondary batteries mainly because of the electrochemical reversibility nature of their redox reactions.

Non-rechargeable batteries have a higher operating cost and environmental impact than secondary batteries. Numerous rechargeable batteries have a higher capital cost, nevertheless, they can be charged at a low cost and for multiple usage times giving a low levelled cost of energy.

Known rechargeable battery chemistries include:

- **Lead–Acid Battery (Pb-Acid):**

Pb-acid batteries have the biggest market share in the electrical energy storage products market. One Pb-cell delivers a nominal voltage of 2.1 V when completely charged. In the charged state the metallic Pb negative electrode and the lead oxide (PbO<sub>2</sub>) positive electrode are immersed in a dilute sulfuric acid (H<sub>2</sub>SO<sub>4</sub>) electrolyte[60].

During discharge, lead oxide accepts electrons and is reduced and lead sulfate is formed, at the negative electrode lead is oxidised and lead sulphate is also formed. While the electrolyte is gradually diluted. Pb-acid batteries can supply high surge currents, maintain a high power density, allied with low cost, and require minimum maintenance). However, they have a low energy density, limited depth-discharge level, and battery materials that are environmentally unfriendly [60].

- **Nickel–Cadmium Battery (Ni-Cd):**

Ni-Cd batteries utilises NiOOH and metallic Cd plates as electrodes. However, Cd metal was banned for most applications by the European Union in 2004 because of its highly toxic nature [60]. Ni-Cd batteries have been nearly substituted exclusively by NiMH batteries.

- **Nickel–Metal Hydride Battery (NiMH):**

The first commercial Ni-MH batteries were made available in 1989. They are now an established consumer and industrial product. The battery houses a hydrogen-absorbing alloy (metal hydride) for the negative electrode instead of cadmium. The battery is less prone to cyclic memory effect than Ni-Cd, environmentally friendly, contains only mild toxic contaminants. They utilise Ni material which makes recycling profitable, exhibit 35–45% higher capacity than a standard Ni-Cd, subject to simple storage and transportation, and is not subject to regulatory control [60]. However, they are susceptible to limited cycle life (deep discharge reduces cycle life), require complex charge algorithms, readily suffer overcharge damage, trickle charge must be kept low, generate heat during fast-charge and high-load discharge, and suffer self-discharge when not in use [60].

- **Lithium-Ion Battery (Li-ion):**

The Li-ion battery is the sole choice in many consumer electronics and possesses one of the best energy density and efficiency levels; however, it suffers from a slow self-



discharge when not in use. Although Li-ion batteries have a market share of over 55% in the small portable electronic devices market, there are still some challenges hindering the development of large-scale Li-ion batteries[60]. The main obstacles include the entailed high capital costs of more than \$900/kWh (due to special packaging), internal overcharge protection circuits, and very short cycle life [61]. However, intense research is underway in an attempt to slash the cost and increase the life of the battery [61][62]. *Lithium-Ion Polymer Battery (Li-Poly)* are light in weight and can be molded into any shape desired. Apart from being ultra-light, the battery has high power density, high capability, and high cell voltage, however, they are costly, delicate, and can explode if misused [62].

- **Nickel–Iron Battery (Ni-Fe):**

Ni-Fe batteries utilise NiOOH and metallic Fe as electrode materials. Ni–Fe cells provide 1.5–2 times the energy density of Pb-acid batteries, with their increased ruggedness and longer cycle life at deep discharge state (2000 cycles at 80% Depth of Discharge). Also, Ni-Fe batteries are well known for their long cycle life, typically exceeding 4000 cycles of charge and discharge vastly exceeding most of their competing technologies, which include Pb-acid (400 cycles), Ni-Cd (1600 cycles), and Ni-MH (600–900)[37].

Among various energy storage technologies, Ni-Fe battery-based electrochemical energy storage offers an ideal practical solution that would help balance by eliminating the intermittent obstacle between electricity production and consumption from the electrical energy grid and demand [10]. Ni-Fe batteries serve as an ideal energy storage system because of the abundant availability of component raw materials, environmental friendliness, electrical and mechanical abuse tolerance, long operational cycle life, and compatibility with photovoltaics (PVs) [10].

There is a superfluity of reasons to forecast a large-scale utilisation of this battery technology. Attributable to their outstanding safety properties (zero flammability, fail-safe, electrochemical abuse tolerance), low cost, and long cycle lifespan [10][63], the anticipation that Ni-Fe will commercially bloom and edge out other competing technologies for customer-connected energy storage is inevitable. However, although appealing, there are a plethora of hurdles to overcome first, such as increasing the coulombic efficiency, averting electrolyte decomposition, inhibiting the evolution of hydrogen, and increasing energy and power densities [12].



, Ni-Fe batteries have the full potential to expand their commercial viability and phase out existing competing energy storage technologies. However, there are numerous drawbacks to overcome first, such as enhancing the coulombic efficiency, avoiding electrolyte decomposition, suppress the evolution of hydrogen, and increasing power and energy densities [12].



## 2.2 Review of Nickel-Iron Batteries

### 2.2.1 History of the Alkaline Ni-Fe Battery

In 1899 Waldemar Jungner, a Sweden national, discovered the first rechargeable battery in which an alkaline electrolyte (such as an aqueous solution of KOH or NaOH) was used. [13][64]. Jungner focused on Ni-Cd and Ni-Fe as the active materials of the system. The American Thomas Edison claimed the invention and patented the Ni-Fe battery in 1901 [64]. A patent dispute caused the collapse of Jungner's company. Jungner then switched his focus on the Ni-Cd batteries, using a pocket plate technique to produce his electrodes. Edison developed the Ni-Fe system based on a tubular electrode design, which was conceptualised and intended for electric vehicles.

By 1903 the Edison Storage Battery Company introduced the Ni-Fe battery to the market. From the start, the Ni-Fe battery already showed an outstanding lifetime of more than 3000 cycles with energy efficiency (Coulombic efficiency) of 55-75% resulting in a cycle life ranging from 20-50 years [13].

### 2.2.2 Basic Operational Principal of a Battery

A battery is an apparatus made of one or more electrochemically reversible cells that reversibly convert stored chemical energy into electrical energy. Primary or non-rechargeable batteries are discharged because the electrode active materials are irreversibly converted during discharge. Secondary or rechargeable batteries can be discharged and recharged multiple times by applying electrical current, reversing the current will reinstitute the original composition of the electrodes. When a battery is discharging (supplying energy or doing work), its negative terminal is the anode and its positive terminal is the cathode and when a battery is charging (accepting electrical charge), its negative terminal is the cathode and its positive terminal is the anode [60].

Each electrochemical cell in a battery is comprised of half-cells coupled in an ion-conductive electrolyte solution constituting cations and anions [13]. One half-cell constitutes the negative electrode and electrolyte solution, the negative electrode is where anions (negatively charged ions) migrate to during discharge; the other half-cell constitutes the positive electrode and the electrolyte, the positive electrode is where cations (positively charged ions) migrate to during

discharge. Redox reactions, in the cell, are responsible for power generation from the battery. Cations are reduced (electrons are accepted) at the cathode during charging, while anions are oxidised (electrons are emitted) from the anode during charging [10] [13]. During discharge, the electron transport processes are reversed. The electrode plates do not physically contact each other but are linked electrically via the electrolyte solution. Some cells utilise different electrolyte solutions for each half-cell compartment. A separator, inserted in-between electrodes, prevents mixing of the electrolytes and electrical short-circuits while allowing ionic charge carriers to shuttle between half-cells [10].

Each half-cell generates a force defined by its ability to drive electrical current from the electrode to the exterior circuit of the cell, this force is termed electromotive force (emf). The net emf of the cell is the difference between the emfs of its respective half-cells. Thus, if the electrodes have emfs  $\mathcal{E}_1$  and  $\mathcal{E}_2$ , then the net emf is  $\mathcal{E}_1 - \mathcal{E}_2$ , in other words, the difference between the reduction potentials of the half-cell reactions [10].

### 2.2.3 Nickel-Iron Battery Components

Ni-Fe battery technology is a rechargeable battery that generates electricity from a redox reaction. The basic configuration of a conventional Ni-Fe battery consists of four major parts:

- The negative electrode, a composite with predominately Fe/FeS material
- The positive electrode, predominantly composed of NiOOH material
- An ionic conducting electrolyte mainly an aqueous alkaline solution KOH or NaOH
- An insulating separator usually a polymeric membrane

The overall reaction between cathode and anode is presented in Equation 1:



The prismatic design of Ni-Fe batteries is the most employed design that is available in the market. Generally, the design consists of a rectangular polymer container, usually made of Polypropylene with the alternating electrode in form of pockets containing the active material.

### 2.2.3.1 Negative Electrode

The negative electrode is an electrode, where the oxidation reaction takes place during the charging phase. An electroconductive substrate is covered or loaded with Fe active material to construct the negative electrode [13]. During charging the Fe-based negative electrode material conducts the electric current through the external circuit while accepting electrons[13]. During discharge, it releases electrons to the external circuit by oxidising iron (Fe) to ferrous iron ( $\text{Fe}^{2+}$ ). The reduction of ferrous ion ( $\text{Fe}^{2+}$ ) to elemental iron (Fe) takes place while charging the electrode. To modify the electrochemical performance of the battery, different additives, and nanostructured materials have been incorporated into the electrode [10].

The electrochemical reactions at the negative electrode are illustrated by Equation 2 :

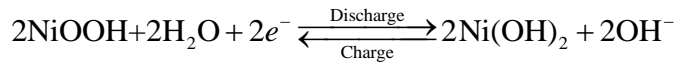


The negative electrode is readily oxidised and has, high charge output, medium electro-conductivity, electrode robustness, low capital cost, and physical stability [10].

### 2.2.3.2 Positive Electrode

The positive electrode in Ni-Fe cells is based on the  $\text{Ni}(\text{OH})_2/\text{NiOOH}$  material[10]. The electro-conductive support is loaded or impregnated with  $\text{Ni}(\text{OH})_2/\text{NiOOH}$  active material to construct the positive electrode [10][65]. There are two polymorphs of  $\text{Ni}(\text{OH})_2$ , namely  $\alpha$ - $\text{Ni}(\text{OH})_2$  and  $\beta$ - $\text{Ni}(\text{OH})_2$ , they can be converted into  $\gamma$ - $\text{NiOOH}$  and  $\beta$ - $\text{NiOOH}$ , respectively [65]. Nevertheless, the  $\beta$ - $\text{Ni}(\text{OH})_2$  is generally utilised as a forerunner electrode material in alkaline Nickel-based batteries due to the poor stability of  $\alpha$ - $\text{Ni}(\text{OH})_2$  in alkaline mediums[60] [66]. Research has been conducted, to enhance the electrochemical performance of the battery, where different additives and nanostructured materials have been incorporated into the electrode [66].

The positive electrode made of  $\text{NiOOH}$  gains electrons from the external circuit during discharge and is reduced, and therefore named the cathode. The half-reactions of the positive electrode are illustrated by Equation 3:



Equation 3

The positive electrode is readily reduced, in the presence of an aqueous electrolyte. It also shows good stability [67].

### 2.2.3.3 Electrolyte

The electrolyte is an ionic conducting medium having low electro-conductance. The solution operates as a medium for ions migration between the negative and positive electrodes at an optimum level and prevents short circuits. The electrolyte is an ion transfer carrier allowing the positive and negative electrodes to generate an electrical potential known as cell voltage. Ni-Fe cells work in strong alkaline solutions of KOH with certain additives such as lithium hydroxide and sulfide-based salts[15].

### 2.2.3.4 Minor Components

Minor components which are essential to the design of a Ni-Fe battery have little or no impact on the overall electrochemical performance of the battery:

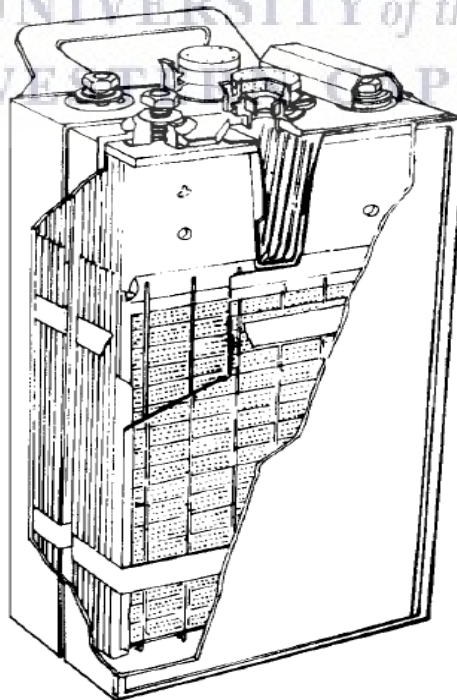


Figure 9: Cross section of Nickel-Iron battery [13]

- Case: a closed container that encapsulates all the battery parts of its electrolyte.
- Cover: a changeable cap facilitating battery maintenance at the top of the battery case gas vents.
- Electrodes: positive and negative plates containing the active materials for both anode and cathode.
- Separators: a porous ion-permeable membrane situated in-between negative and positive plates to avoid short-circuiting the battery. Separators ensure that electrons can only shuttle from the anode to the cathode via the external circuit.
- Vent Caps: they allow regulated expulsion of hydrogen gas produced during charging and the level of the electrolyte during battery maintenance.
- Terminals: Positive and negative electrical contacts on the case top, made of thick and metal connectors allowing it to collect the current generated by the battery or to charge it.

#### **2.2.4 Nickel-Iron Battery Characteristics**

The properties of the positive electrode, negative electrode, and the electrolyte solution constitute the pillars of the electrochemical performance of a Ni-Fe battery.

The electrochemical performance is evaluated and measured via various parameters defined in Appendix A: Definition of battery parameters, which include capacity, efficiency, discharge and charge characteristics, charge retention, cyclability and safety, and environmental friendliness [10] [68].

##### *2.2.4.1 Efficiency*

The energy efficiency of Ni-Fe batteries can differ, depending on the application of the battery, it's the design and the material composition of electrodes, and operating conditions. Round-trip energy efficiencies of Ni-Fe batteries range from 65% to 80%, not including energy losses caused by conditioning cycling [56]. The factors mentioned below represent the main factors in determining the efficiency of a Ni-Fe battery [36] [31].

- Electrolyte concentration: Electrolyte solution concentration can be modified to optimise voltaic and energy efficiency.
- Charging program: Charging at high charge rates to high-end voltages yields lower voltaic and energy efficiency. Prolonged overcharging will lower energy efficiency, as the majority of overcharge input is channeled to hydrogen evolution through electrolysis. Some studies have specified that pulse charging can boost both the voltaic and energy efficiency of a battery [31].
- Stand-time: If a battery is kept charged in an open-circuit state, it will lose energy through self-discharge (15% of its nominal capacity in the first 10 days), reducing the overall energy efficiency when it is discharged.
- Operating temperature: Operation at higher temperatures causes poorer charging efficiencies.

#### 2.2.4.2 Discharge and Charge Characteristics

The Ni-Fe battery delivers partial to full nominal capacity at any discharge rate, but the discharge should be aborted beyond the point where the discharge capacity nears exhaustion. The battery functions optimally when adapted to low or moderate discharge rates (0.15C-1C). The cut-off voltage during discharge depends on the battery's application and the desired cycle life but is conventionally between 0.6 and 1 V/cell. Moreover, the nominal voltage for Ni-Fe batteries is 1.2 V/cell. The charge cut off voltage widely enrolled to limit hydrogen gas evolution is approximately 1.6 V/cell [56].

Figure 10 and Figure 11 illustrates the charge and discharge characteristics of a typical Ni-Fe battery.



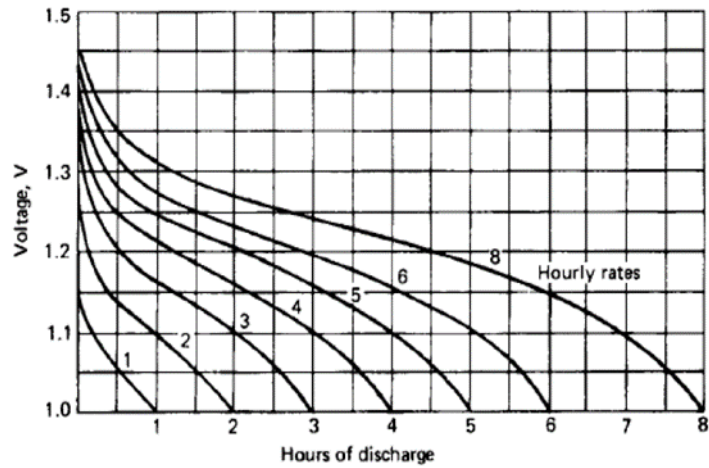


Figure 10: Time-Voltage discharge curves of Nickel-Iron battery[60]

Excessive hydrogen gassing will be temporarily combated by the frequent addition of water. If the cell voltage is limited to 1.6 V, an excessive gassing scenario should be avoided [56].

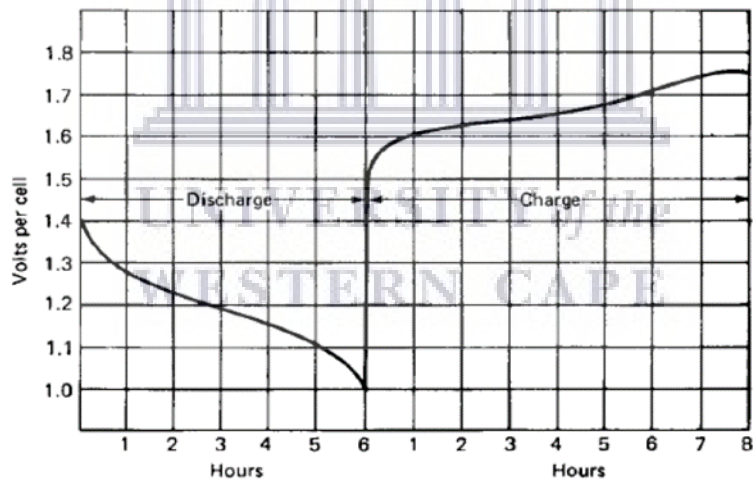


Figure 11: Ni-Fe typical voltage characteristics during constant-rate discharge[60]

The ampere-hour energy input (charge capacity) should be 10 to 40% above the amp-hour energy output (discharge capacity) to ensure attainment of full charge, the suggested charge rate is normally between 0.125C and 0.2C. These rates deliver the approximate nominal capacity in the 5-8 hr time frame as shown in Figure 12 [60].

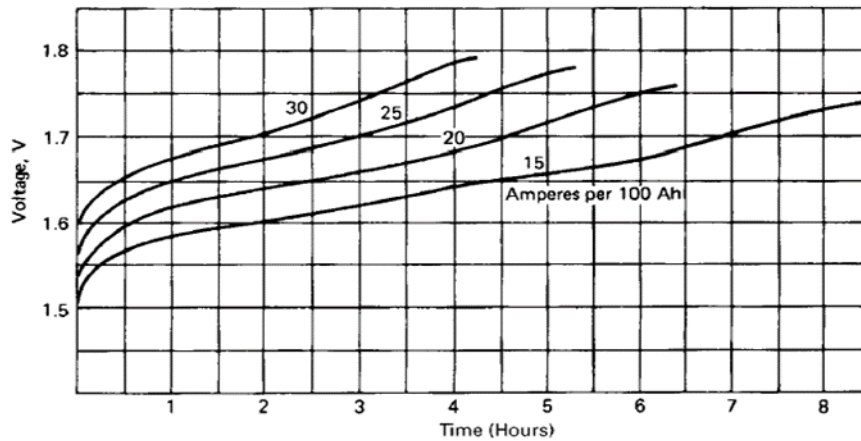


Figure 12: Typical charging voltage for a Nickel-Iron battery at various rates[60]

### 2.2.4.3 Charge Retention

Ni-Fe batteries lose charge slightly more quickly than Ni-MH, Li-ion, Pb-acid batteries, and various other energy storage technologies. At room temperature, fully-charged Ni-Fe batteries lose 2% to 10% of their amp-hour energy input (charge capacity) per month [60]. Charge retention in Ni-Fe batteries is not a big issue since its used in stationary storage ,where it is exposed to a daily charge.

By comparison, Pb-acid batteries lose about 1% of their amp-hour energy input per month. The rate of charge loss follows a decaying exponential curve thus the majority of amp-hour energy input is lost immediately after charging.

Self-discharge, in Ni-Fe batteries, emerges from multiple sources, the dominant source is the slow conversion of NiOOH to Ni(OH)<sub>2</sub>, along with corresponding reactions on the counter electrode [68] [56]. There is an additional mechanism of hydrogen diffusing to the positive electrode and reacting directly with the Ni-based active material [65].

Besides, there is also the possibility of a leakage of current contributing to the loss of charge attributed to resistive external current paths, electrode damage, or separator decay. The rate of self-discharge or charge loss increases rapidly with an increase in temperature. This correlation generates several critical issues in system design [56].

Ni-Fe batteries have extreme sensitivity to temperature gradients. If two cells in the same battery are operating at different temperatures, their self-discharge rates will be different, leading to a specific capacity variance over time [69].

This can lead to overcharging or current reversal, potentially instigating battery damage. Another important factor of the Ni-Fe battery characteristics is the effect of temperature, Sealed battery designs are generally much more susceptible to thermal runaway incidences than vented battery designs [70].

#### 2.2.4.4 *Effect of Temperature*

While Ni-based batteries are generally less temperature-sensitive than other competing battery technologies (Li-ion, Pb-acid, Ni-Cd, etc), the temperature can have negative effects on the overall electrochemical performance and life of the battery [36], the effects are depicted below:

- Internal resistance: Internal resistance decreases when the internal temperature rises. The decrease in internal resistance is attributed to the increase in electron mobility.
- Self-discharge: The rate of self-discharge (charge loss) increases when the internal temperature rises, as the electrochemical reactions inducing capacity loss to accelerate.
- Open Circuit Voltage (OCV): OCVs increase at higher temperatures due to inflated thermodynamic effects. Besides, since internal resistance is low at higher internal temperatures, over-voltages are lower for a specified current. These effects work collectively during discharge at high temperatures to cause higher discharge voltages but work against each other during charge consequently generating little effect.
- Capacity: Charge capacity decreases when the battery is charged in very high ambient temperatures, largely as a consequence of self-discharge.
- Life: Operation and storage at higher temperatures reduce the life of the battery. In general, the rate of aging amplifies when operated and stored at higher temperatures.

Smart battery design can, to a certain extent, circumvent the apparent trade-offs associated with temperature. Operations of a Ni-Fe battery in cold ambient temperatures will result in higher charge capacity but lower discharge voltage, while operation in warm ambient temperatures will result in higher discharge voltage but lower charge capacity [69].

This is an apparent trade-off in battery design. It has been demonstrated, however, that if the battery is charged in a cold bath and then warmed just before discharge, it will yield the high

charge capacity of a cold battery at the high discharge voltage of a warm battery, increasing the overall energy density.

Many Ni-Fe batteries, mostly sealed Ni-Fe batteries, experience a condition termed “thermal runaway.” This occurs when the internal temperature of the battery surpasses a certain critical temperature, attributable to high ambient temperature, high-rate charge or discharge, or overcharge. The elevated temperatures accelerate the rate of self-discharge rate. The energy lost by the cell through self-discharge is converted to heat, which heats the cell further. This malicious cycle continues until the battery fails, usually through separator decomposition or melting or failure of some other battery component(s). In some designs of Ni-Fe batteries, such as sealed Ni-Fe batteries, thermal runaway can lead to rupture of the casing, potentially creating a hazardous situation.

Thermal runaway scenarios can be avoided by integrating a proper cooling system onto the battery or by avoiding very high charge currents and long periods of overcharge. Thermal runaway invented batteries are unlikely except in specific circumstances, such as high-rate charging or prolonged exposure of electrode plates in an electrolyte starved medium.

#### 2.2.4.5 Cyclability

Ni-Fe battery, in its prismatic design, has a long life, and robust structure. Its life cycle ranges from 10 years when used for heavy-duty applications to 20 years or more for standby or float service applications. When heavily operated, 2000 cycles are easily reachable, under optimum conditions, by limiting the maximum operating temperatures to 35°C, 4000 to 5000 cycles have been accomplished [10][65].

The battery exhibits resistance to electrochemical damage caused by repeated deep discharge more than any other battery technology[71]. Cycling stability of a typical Ni-Fe battery is shown in Figure 13.

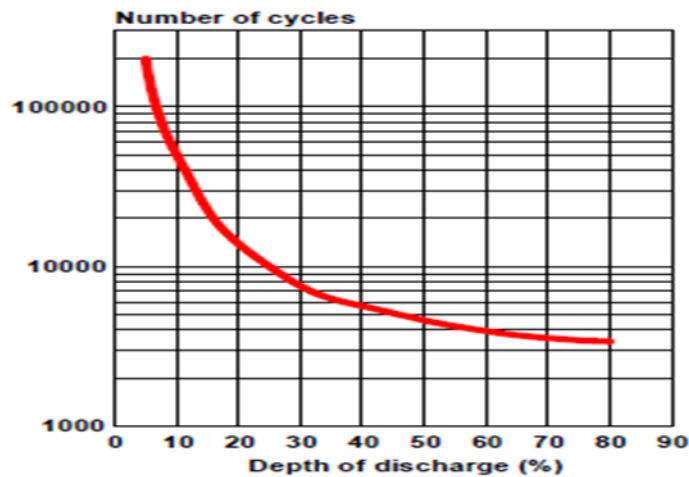


Figure 13: Cycle life as a function of depth-of-discharge for a typical Ni-Fe cell[60]

#### 2.2.4.6 Capacity and Rate Capability

The energy capacity of the Ni-Fe battery is electrochemically limited by the energy capacity of the positive Ni-based electrode and, hence, is a function of the active material quantity deposited on the positive plate [60]. The 5 hours discharge rate (0.2C or 5C) is usually employed as a reference for evaluating its energy capacity.

The Ni-Fe battery delivers moderate energy and power density for applications requiring low to moderate discharge rates ( $< C/10$ ) [70]. The battery is not adequate for high discharge rate applications such as starting up a car's engine [25]. The accumulation of internal resistance in the battery limits the terminal voltage when used for high discharge rate applications [65][60].

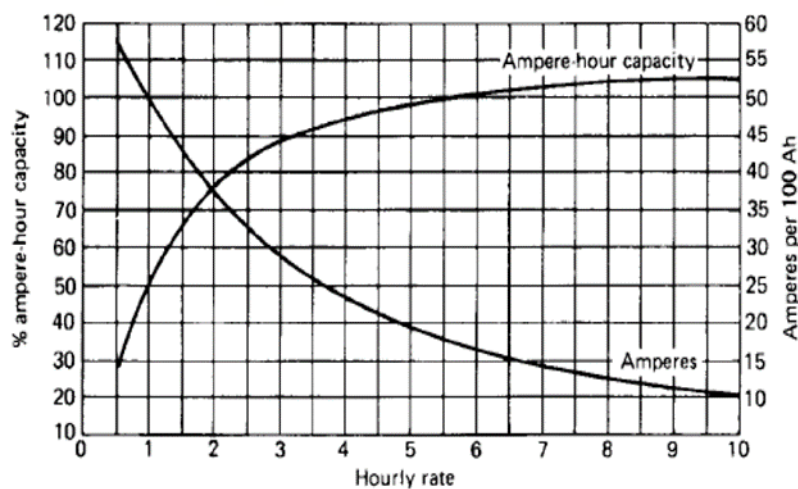


Figure 14: Correlations between capacity and discharge rates at 25°C[60]

As illustrated in Figure 14, the maximum capacity of the Ni-Fe battery is attained when the

discharge current is optimum at a 5-h discharge rate (C5 or 0.2C). When Ni-Fe battery is discharged at a high rate for one cycle, then discharged at a lower rate in the next cycle, the sum of the capacities delivered at the high and low rates approximately equals the capacity that will be attained at the single optimal discharge rate [65][60].

#### *2.2.4.7 Safety and Environment*

The safety concerns about Ni-Fe batteries are comparable to most existing battery technologies. Ni-Fe batteries work with an aqueous alkaline electrolyte which can cause a health hazard to exposed operators. Chemicals such as Ni(OH)<sub>2</sub>, also causes a genuine health hazard when ingested or contacted with human skin.

Ni-Fe batteries develop some gases, mainly, hydrogen and oxygen during the charging process caused by electrolysis of water in the aqueous alkaline electrolyte. Some sealed batteries contain a recombination system equipped with a catalyst like palladium or platinum. The released hydrogen and oxygen will then recombine in the battery and subsequently prevent a health and safety hazard to the maintenance operators [16]. It was reported that sealed cells may outpace the recombination rate of the battery when charged at a high rate due to the excessive amount of hydrogen. The gases inside the battery will lead to pressure build-up that may cause a serious hazard. However, most batteries are equipped with a safety valve that is designed to relieve pressure preventing the battery from cracking.

Batteries with a vented system, allows the hydrogen and oxygen gases accumulated during charge to be released to the atmosphere. Usually, it is advised to install the Ni-Fe batteries in a well-ventilated space where the generated gases are expelled into the atmosphere.

In general, Ni-Fe batteries are recyclable, and environmental organisations operating in most countries recycle the waste resulting from the disposal of these batteries in a safe eco-friendly way [56].

### **2.2.5 Negative iron Electrode**

#### *2.2.5.1 Electrochemistry*

The negative iron electrode in Ni-Fe batteries is made of Fe-based active material mixed with multiple additives. The Fe-based electrode has a theoretical specific capacity of approximately 0.97 Ah.g<sup>-1</sup> [65]. It was reported that the Fe-based electrode can withstand electrochemical over usage[60]. Moreover, Fe active material is eco-friendly and abundant all over the globe. The



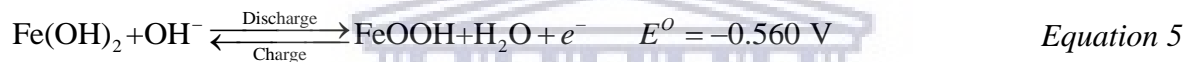
active material of the Fe electrode is a blend of Fe and Fe(OH)<sub>2</sub> [60].

The electrochemical reactions of charge/discharge illustrated in Equation 4 and Equation 5 have two different potentials respectively at -0.877 V and -0.560 V [16]. The Equation 5 rarely occurs since Ni-Fe cells are designed with an excess of Fe-active material.

The electrochemical charge/discharge reactions illustrated in Equation 4 :



The electrochemical charge/discharge reactions



Equation 4 is more reversible thermodynamically due to its higher negative electrode potential, while Equation 5 has a lower negative potential consequently it does not accept charge so readily [65].

Reports on the kinetic behaviour of the Fe-based electrode show strong evidence of a dissolution-precipitation mechanism [72] [73]. The kinetic mechanism of the electrochemical reaction is considered to be heterogeneous or multiphase involving liquid and solid phases [74].

X-Ray Diffraction Analysis of various discharge steps and subsequent products of a pure Fe electrode coupled with cyclic voltammetry characterisation on pure Fe electrodes in alkaline electrolytes showed that the oxidation of Fe happens in two multiphase steps as shown in Figure 15. The two steps involve the formation of soluble ferrite HFeO<sup>2-</sup> and ferrate FeO<sup>2-</sup> intermediates [74].



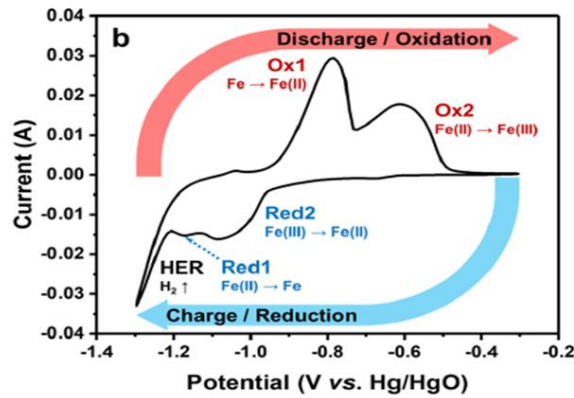


Figure 15: Voltammogram curve with the redox peaks assigned to corresponding reactions [74]



The first oxidation step of Fe to Fe(II), as a result of reactions Equation 6 and Equation 7, is more significant practically for cell operation than the second step from Fe(II) to Fe(III) illustrated by reactions Equation 8 and Equation 9 [74].

The pure Fe-based electrode during discharge involves first the formation of a ferrite ion which is soluble and dissolves in the electrolyte. Then, the ferrate ions undergo hydrolysis as shown in Equation 9 to precipitate as Fe(OH)<sub>2</sub>.

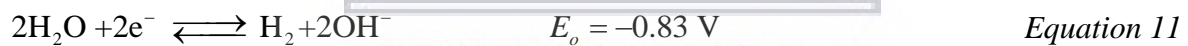
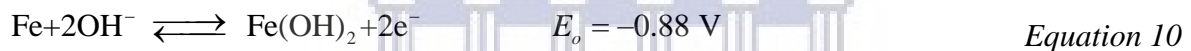
Ferrite ions have very low solubility, and the precipitated thin layer of ferrous hydroxide covers the electroactive area and causes a low active material utilisation coefficient. The low solubility of ferrite is dependent on the temperature and such correlation indicates that the electrochemical performance of the electrode at sub-zero temperatures is poor [75]. The

solubility of ferrite ion is in the order of 10<sup>-1</sup> M, this concentration can secure optimum electrochemical conditions at the Fe electrode [76].

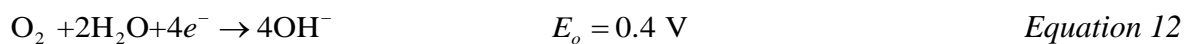
The mechanism of the Fe-based electrochemical reaction involves proton diffusion through the Fe(OH)<sub>2</sub> and δ-FeOOH solid-state network, therefore there is a gap in the electrode material mix between Fe(OH)<sub>2</sub> and δ-FeOOH. Considering that the transformation of Fe(OH)<sub>2</sub> to δ-FeOOH is a total process, the second discharge step of the mechanism is mainly homogeneous [77].

The open-circuit potential of a typical charged pure Fe electrode is relatively more negative than that of the hydrogen electrode in the same alkaline medium [65]. Fe is thermodynamically unstable and undergoes passivation with hydrogen evolution being the parasitic reaction.

The charge/discharge and hydrogen evolution reactions are respectively outlined in Equation 10 and Equation 11.



Moreover, the dissolved oxygen in the alkaline electrolyte can react according to Equation 12.



Oxygen dissolution reaction depicted in Equation 12 enables the passivation of Fe material. Through passivation reaction, the iron electrode causes self-discharge with a daily rate ranging from 1 to 3 % at room temperature. Hydrogen evolution as illustrated by Equation 11 also takes place simultaneously with the oxygen dissolution reaction during the charging process of the Fe electrodes in an alkaline medium [60] [70]. It was reported that the parasitic side reaction influences the charge acceptance of the electrode. Iron passivation affects the coulombic efficiency of the Fe electrode and is based on the 2-electron reaction, as per *Equation 11*, ranging from 35% in commercial iron electrodes to 65% in electrodes with high-purity Fe [60].

The potential of the redox couple Fe/Fe(OH)<sub>2</sub> depicted in Equation 10 is marginally more negative than Hydrogen Evolution Reaction (HER) in an aqueous alkaline medium. The hydrogen overvoltage is very low, consequently, a fast hydrogen evolution takes place during the charging process [65]. The high self-discharge rate of the Ni-Fe battery and its low coulombic efficiency is due to the side hydrogen evolution reaction [65][16].

The overall electrochemical performance of the Ni-Fe battery is influenced by the Fe-based electrode [15], subsequently, any modification of the electrode structure, morphology, or production techniques will have a huge impact on the electrochemical performance of the battery [14] [60].

## 2.2.6 Positive Electrode

### 2.2.6.1 Electrochemistry

In Ni-Fe batteries, the Ni-based active material is used as the positive electrode. The Ni-based electrodes have a low specific capacity compared to the Fe materials ranging from 0.100 to 0.260 Ah.g<sup>-1</sup> [65] [78]. NiOOH is obtained from the starting material, Ni(OH)<sub>2</sub> [66] [67] [16]. The reversible charge/discharge reactions are illustrated in Equation 13:

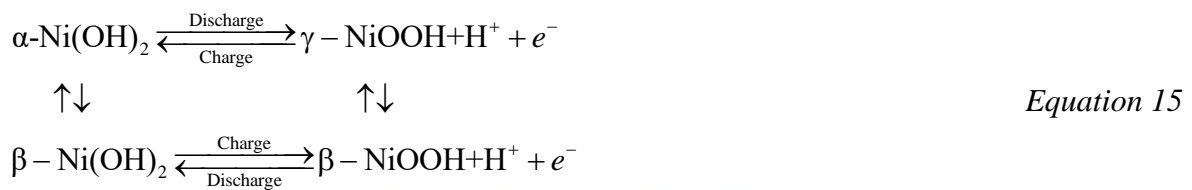


The electrochemical reaction mechanism includes the diffusion of hydrogen ions through the solid-state lattices of Ni(OH)<sub>2</sub> and NiOOH causing changes in the composition of the electroactive material [79]. The electrochemical reactions are illustrated as per Equation 14 :



Crystallographic polymorphs of Ni(OH)<sub>2</sub> and NiOOH exist [65]. Ni(OH)<sub>2</sub> can manifest as α-Ni(OH)<sub>2</sub> and β-Ni(OH)<sub>2</sub> polymorphs in the composition of the Nickel-based electrode. α-Ni(OH)<sub>2</sub> exhibits a layered structure with intercalated water molecules while β-Ni(OH)<sub>2</sub> shows a brucite structure layered with minimal water molecules content when resulting from

electrochemical precipitation from concentrated Ni(NO<sub>3</sub>)<sub>2</sub> solution [64][65]. Upon oxidation of [Ni(NO<sub>3</sub>)<sub>2</sub>·6H<sub>2</sub>O] in alkaline solution, hydrated γ-NiOOH forms and from β-Ni(OH)<sub>2</sub> synthesised by chemical precipitation β-NiOOH forms upon oxidation[65]. β-NiOOH is transformed to γ-NiOOH when the Nickel-based electrode is overcharged, α-Ni(OH)<sub>2</sub> produced from γ-NiOOH can be dehydrated to form β-Ni(OH)<sub>2</sub> [66]. The electrochemical process of charging and discharging is depicted in the equations numbered as per Equation 15 :



The electrode structure, morphology, and production techniques have an impact on the electrochemical performance of the positive electrode [66] [65].

#### 2.2.6.2 Composite Electrode Structure

The modification process of a composite electrode structure is a way of producing high-quality electroactive material content with the optimised electrochemical performance [71]. Composite electrodes can offer optimised electrical conductivity and high energy density [79]. The Ni composite electrodes exhibit optimum electrochemical properties demonstrated by an energy density ranging from 120 to 180 Ah·g<sup>-1</sup> [65]. Ni-coated fibers and graphite flakes can be employed to produce a highly porous substrate. Ni(OH)<sub>2</sub> is then loaded onto the substrate and mixed with a certain amount of Co(OH)<sub>2</sub>. and electrochemical precipitation is used to synthesise a composite electrode with optimised electrochemical behaviour [65] [71]. The resultant formation of aggregates is caused by metal complexation within the active mass. Layering faults increase the reactivity of the solid mass when adding Co(OH)<sub>2</sub>, which has an isostructural shape with β-NiOOH and β-Ni(OH)<sub>2</sub>. The Co(OH)<sub>2</sub> creates a disordered structure by occupying layers between layers of the β-Ni(OH)<sub>2</sub>, consequently contributing to the formation of aggregates. It was reported that cobalt can be used as an additive to increase the overpotential of oxygen evolution and to reduce both the oxidising and the reducing potentials of Ni(OH)<sub>2</sub> and [16][64]. It was noted that a composite blend of Cd(OH)<sub>2</sub> and Co(OH)<sub>2</sub>

increases the discharge capacity and coulombic efficiency of Ni electrode by enhancing the reversibility of the electrode's electrochemical reactions and curtailing of the parasitic oxygen evolution [79].

In the same context,  $\text{Co}(\text{OH})_2$  maintains the cycling capacity of a nickel cathode, by enhancing the utilisation coefficient of the  $\text{NiOH}/\text{NiOOH}$  active material.  $\text{Ba}(\text{OH})_2$  demonstrated comparable constructive effects in the presence of lithium ions drawn from the electrolyte [65]. Zinc, Cadmium, and magnesium-containing compounds were found to be slightly effective in blocking the Oxygen Evolution Reaction (OER) compared to  $\text{Co}(\text{OH})_2$  [80]. It was reported that oxidised metal species are less electronically conductive than pure metals in alkaline systems, explaining the need for conductive substances such as carbon black or graphite depending on the electrode production technique[80].

### 2.2.6.3 Structure and Morphology of Nickel-based active material

$\text{Ni}(\text{OH})_2$  in its beta form  $\beta\text{-Ni}(\text{OH})_2$ , is the main active material of the positive electrode in alkaline aqueous batteries [8]. Both Ni oxides and Ni hydride are used as starting active material. Both chemicals are already transformed into  $\beta\text{-Ni}(\text{OH})_2$  since it is the most thermodynamically stable composition of Ni in an alkaline medium, thanks to its low solubility coefficient  $K_{\text{sp}} = 10^{-35}$  [64]. A reversible solid state-nature governs the reaction between  $\beta\text{-Ni}(\text{OH})_2$  and  $\beta\text{-NiOOH}$  in which a proton is intercalated into the structure [64] [70]. Figure 16 shows an illustration of the  $\beta\text{-Ni}(\text{OH})_2$  structure:

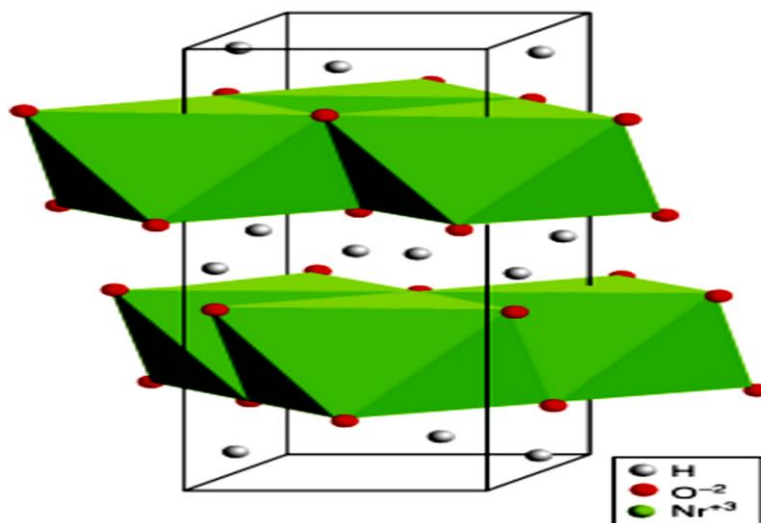


Figure 16: The  $\text{Ni}(\text{OH})_2$  layered crystal structure [64]

The compound is structured in layers as octahedral NiO<sub>6</sub> units with hydrogen atoms embedded in between bound to the oxygen. The NiO<sub>6</sub> units act as a solid structure accommodating the hydrogen atoms occupying the interstitial sites within the structure. β-NiOOH was characterised as an electric semiconductor with average resistance ranging from 10<sup>4</sup> to 10<sup>5</sup> Ω·cm<sup>-1</sup> at room temperature [64].

During the discharge process, the Ni(OH)<sub>2</sub> species act as an electric insulator with resistance values ranging from 10<sup>10</sup> to 10<sup>12</sup> Ω·cm<sup>-1</sup> at room temperature. Deep discharge capacities cannot be attained due to passivation. The formation of insulating Ni(OH)<sub>2</sub> around β-NiOOH affecting the electrochemical reactivity by decreasing the active surface area [64]. The β-NiOOH/ β-Ni(OH)<sub>2</sub> redox reaction is described as a solid-state reaction, the solubility of the species is rather low but involves dissolved intermediates. The kinetics of the aforementioned mechanism determines the performance of the active material dependent on the dissolution rates of the existing species.

The Ni(II)/Ni(III) reaction is affected by electric conductance to the point where the current collector cannot collect the electrons due to the formation of insulating species [81]. The transformation route of the Ni-based material is described through the Bode diagram, shown in Figure 17. It was reported that the two other phases need to be accounted for: γ-H<sub>x</sub>K<sub>y</sub>NiO<sub>2</sub>·H<sub>2</sub>O in the charged state, where x and y are often claimed to be 0.33 and 0.66, respectively, and α-NiOOH in the discharged state [64] [81].

During the overcharge, the H<sub>x</sub>K<sub>y</sub>NiO<sub>2</sub>·H<sub>2</sub>O grows in an interlayer space, allowing the intercalation of soluble species in the electrolyte into the structure. During discharge, an electrode dry-out can occur, besides β-form an α-Ni(OH)<sub>2</sub> can form from H<sub>x</sub>K<sub>y</sub>NiO<sub>2</sub>·H<sub>2</sub>O, which is transformed back to β-Ni(OH)<sub>2</sub> spontaneously overtime in an alkaline medium. It was reported that theoretically, α-Ni(OH)<sub>2</sub> starting material allows a much higher specific capacity than β-Ni(OH)<sub>2</sub> mainly because of the interlayer distance [81] [64].

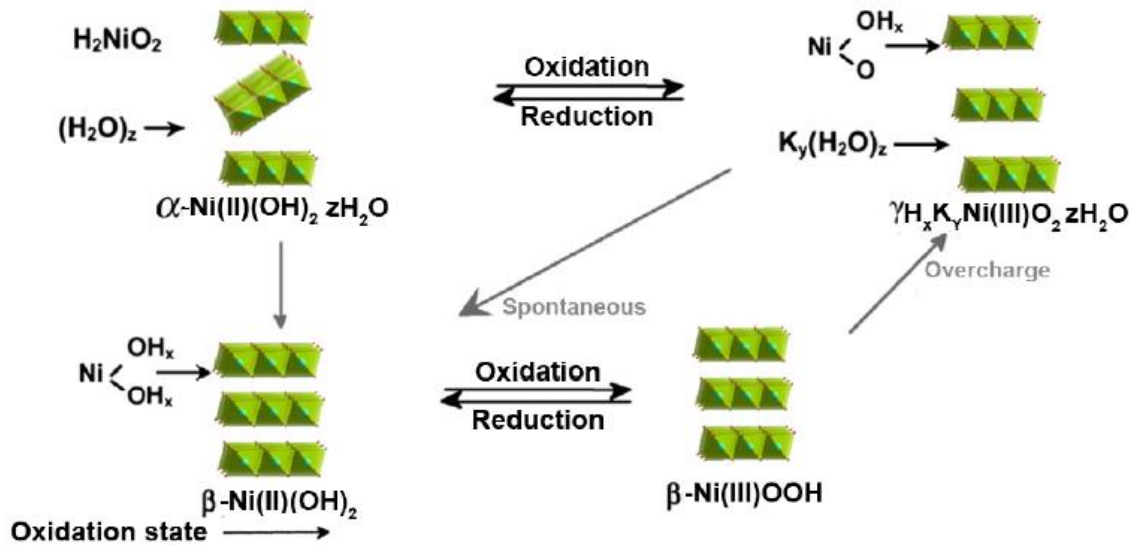


Figure 17: Bode diagram showing transformations among various phases of the nickel hydroxide [64]

Preparation methods can have an impact on and the overall electrochemical performance of the electrode via the incorporation of some additives. Multiple reports indicate that Ni-based material is known for its reversibility and cycling behaviour [81] [64].

Multiple studies have been conducted to gain an in-depth look at optimising the material characteristics of the electrode material to ultimately improve its electrochemical performance. Stacking issues pop out when the normal stacking sequence in the crystal structure is interrupted, causing intercalation issues between the protons and the Ni ions. Approximately, 15 to 20% of stacking issues in the crystal structure are the prevention of the electroactive material from achieving their supposed theoretical energy densities of  $289 \text{ Ah}\cdot\text{kg}^{-1}$  [64].

## 2.3 Ni and Fe Electrode Design and Construction

### 2.3.1 Types of Electrodes

#### 2.3.1.1 Tubular /Pocket Plate Electrodes

An early design of the Ni-Fe batteries was based on pocket-plate electrodes construction. Figure 18 shows a standard pocket-plate design [65]. Granular active material was embedded inside pre-perforated Ni-plated steel sheets or thin Ni sheets filled with palletised active material powder, which is blended with conductive additive, mostly graphite together with other suitable additives. The powder mixture is then pressed into the pocket of the folded steel



sheets closed through the strips along the edges. The pressed pockets holding the active material acts as a current collector [64]. It was stated that the exposure of the current collector to the electrolyte interface leads to an increase in the overpotential of HER. Nickel-plated pockets' influence on the increase in the overpotential is inevitable due to the diffusion mechanism, which makes the design suitable only for low-current density applications. The pocket plate construction is extensively used thanks to its robustness [65].

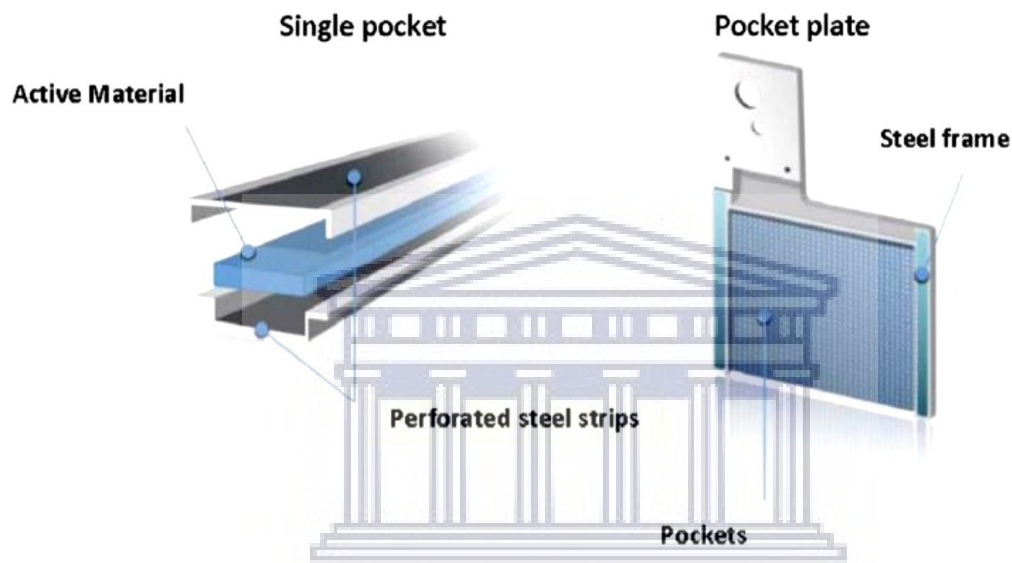


Figure 18: Pocket plate construction [65]

### 2.3.1.2 Sintered Electrodes

The sintering process consists of thermal deposition, in an inert atmosphere, the detached active particles are altered into a homogeneous porous structure through heating below the melting point of iron. Embedded nickel carbonyl powder on a current collector is sintered in an inert atmosphere at 1115 K to produce a porous structure [71]. It stated that various inert atmospheres can be employed, such as argon, nitrogen, or a mixture of all the aforementioned gases. The current collector can be a Ni mesh or Ni-plated stainless steel mesh [65]. Before the sintering process and under dry conditions, a graphite mould is used to embed the nickel powder on the current collector; the process is called dry powder sintering.

Wet sintering is a different process where consistent Ni-based slurry is embedded on a substrate preceding the sintering process. The outcome of these methods produces mechanically stable electrodes characterised by a porosity ranging from 70 to 90% porosity [16]. Vacuum

electrochemical deposition of  $\text{Co}(\text{OH})_2$  and  $\text{Ni}(\text{OH})_2$  can be conducted to occupy the free spaces of the Ni substrates [16] [65]. Sintered electrodes allow a high electrical conductivity due to the crystal structure together with the high mechanical stability. However, sintered electrodes have a high inactive/active weight ratio and engender high production costs [64] [65]. Sintered electrodes have been the dominant technology in the market as they allow higher charge/discharge rates compared to the pocket plate technology [64].

### 2.3.1.3 Paste Type Electrodes

The active material is mixed with the specified additives in the presence of polymer-based binders such as PE or PTFE. The paste is then pasted on a porous substrate made of nickel mesh or nickel foam shaped into the required thickness. The drying phase takes about 24 to 48 hours in a vacuum oven [82][12]. Paste type electrodes show a higher electrochemical performance when compared to the pocket plate electrode and sintered electrodes, mainly in terms of capacity values delivered by the active materials [83]. Moreover, paste-type electrodes are suggested to have lower production costs, so, they are offering an attractive alternative to sintered electrodes [15] [84].

### 2.3.1.4 Pressed- and Roll-Compacted Electrodes

Active materials are blended with conductive substances and other additives, joined with a polymeric binder such as PE, PTFE, or PVDF to develop a mixture [65]. The mixture is then, hot-pressed on an electrically conductive substrate as a current collector, usually in the form of a nickel mesh. Another process is the roll to roll process, where the active material and the nickel mesh roll is fed into a rolling press apparatus [83][85]. The thickness regulation is controlled through the variation of the applied pressure and the space between the two pressing rolls [65].

Some chemicals are used in the mixture as a pore-former additive, such as  $(\text{NH}_4)_2\text{CO}_2$  or NaCl, to enhance the porosity of the pressed electrodes. The latter shows better performance characteristics in terms of cycling longevity under a standard current discharge rate of C/5-10 [65][83].

### 2.3.2 Battery/Cell Design

Engineers designed different types of aqueous batteries, such as cylindrical or rectangular cells. Inside the battery, the cells may be configured in series or parallel. To compensate for electrolyte depletion, some batteries are equipped with a valve-regulator to ensure maintenance operation by refilling the electrolyte chamber [64]. Sealed batteries are designed to handle gases build-up mainly, through recombination systems equipped with catalysts[64].

#### 2.3.2.1 Prismatic Batteries/Cells

It was stated that prismatic batteries design, contained electrodes arranged in different shapes, mainly, rectangular or circular electrodes are assembled by alternating negative and positive electrodes [86].

To prevent short-circuiting and ensuring a good ionic conductivity a separator is placed between two consecutive electrodes. The battery casing may be made from alkali-resistant materials such as polycarbonate. Some battery models equipped with steel casing may be electrically insulated with plastic coatings or moulded in nylon [13].

Prismatic batteries are the most widely distributed design due to their robustness and simple construction. Figure 19 shows a prismatic Ni-Fe battery cross-view.

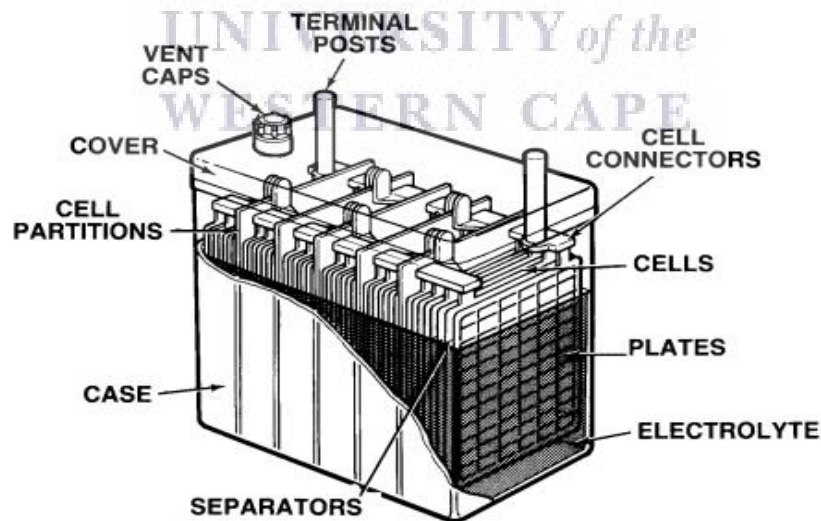


Figure 19: Nickel-Iron prismatic battery

### 2.3.2.2 Cylindrical Batteries/Cells

Cylindrical battery design consists of coiled electrodes a separator in a roll form. The roll is then placed in a cylindrical nickel-plated steel case where the top seal is welded to the positive electrode and the negative electrode is connected to the bottom body of the casing. The electrolyte is jellified into the cylindrical casing at a level equals to that of the electrodes and separator. However, this design is not suitable for Nickel-Iron battery production due to concerns about pressure build-up and excessive gassing during the overcharge. However, this design is considered to be suitable for mass production [13].

### 2.3.2.3 Bipolar Batteries/Cells

The bipolar Ni-Fe battery technology pursues an innovative combination of optimised battery components and design in conjunction with the application of novel mass-production techniques [87].

As shown in Figure 20, a typical bipolar battery includes electrodes with a metallic substrate on which positive active material forms one surface while the opposite surface contains the negative active material. The active masses are adhered by numerous ways on the conductive metal substrate. The electrodes are assembled in a parallel configuration allowing the stacking of a multi-cell battery with electrolyte chamber and separator forming an interface between adjacent electrodes.

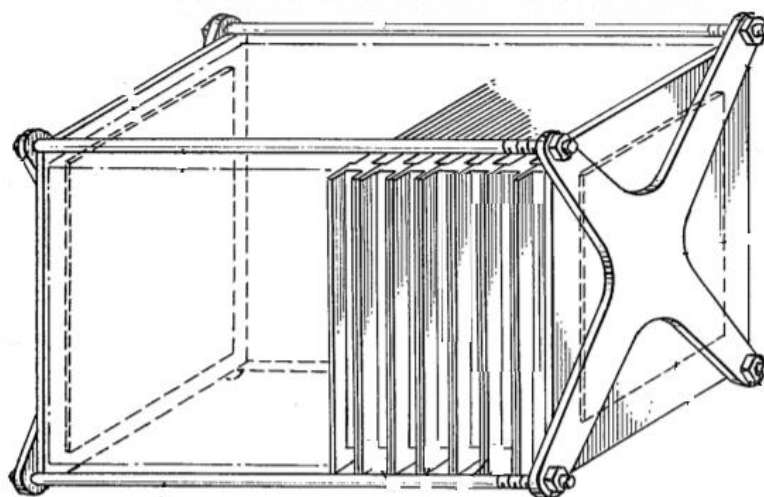


Figure 20 : Schematic of Bipolar battery Construction [88]

Monopolar electrodes are placed at the ends of the stack to provide an electrical connection with the output terminals. The role of using a bipolar battery configuration allows a better power density, nevertheless, the bipolar battery suffers from substrates corrosion and, active material retention problems [88] which prevented the early bipolar versions of the lead-acid battery to achieve commercial success [88].

The bipolar battery has various advantages, it offers less overall weight by reducing the number of parts necessary for the construction, it allows a higher power density due to stackable configuration, in a conventional bipolar design, shown in A2-Figure 21 the electrodes are stacked in a small volume while allowing a high voltage output [89].

As illustrated in, A1-Figure 21, the connectors, straps, and posts, usually used to transfer the current in a monopolar design, are not needed in a bipolar design. The current collectors, located at the end of the battery stack, allow a perpendicular electron flow throughout the stack, ensuring a uniform current and potential distribution. The bipolar design can eventually offer a higher peak power compared to a traditional monopolar design [89].

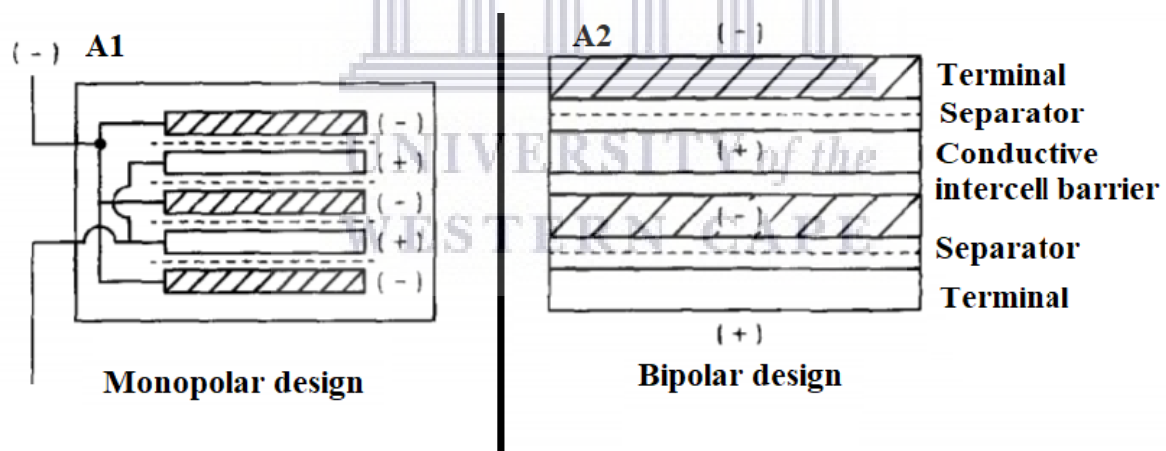


Figure 21 : Comparison of monopolar (A1) and Bipolar (A2) Lead-acid battery design [89]

Among the advantages of the bipolar design, it offers reduced cost, materials, and energy consumption, making the battery environmentally sustainable for energy storage. A comparison of design schematics is illustrated, where unipolar electrodes are used in A1-Figure 22 to form one unit cell, and, bipolar electrodes are used in A2-Figure 22 to form a two-unit cell. This design is considered to be a potential solution to the recent concerns regarding low recycling efficiency and high environmental risk batteries [90]. It was reported that bipolar

sodium-ion-battery used in large-scale energy storage systems offers a low battery cost, better environmental sustainability with regards to the recycling operation. Battery bipolar designs with material selection can help achieve the next-generation energy storage system with high efficiency and green footprint [90].

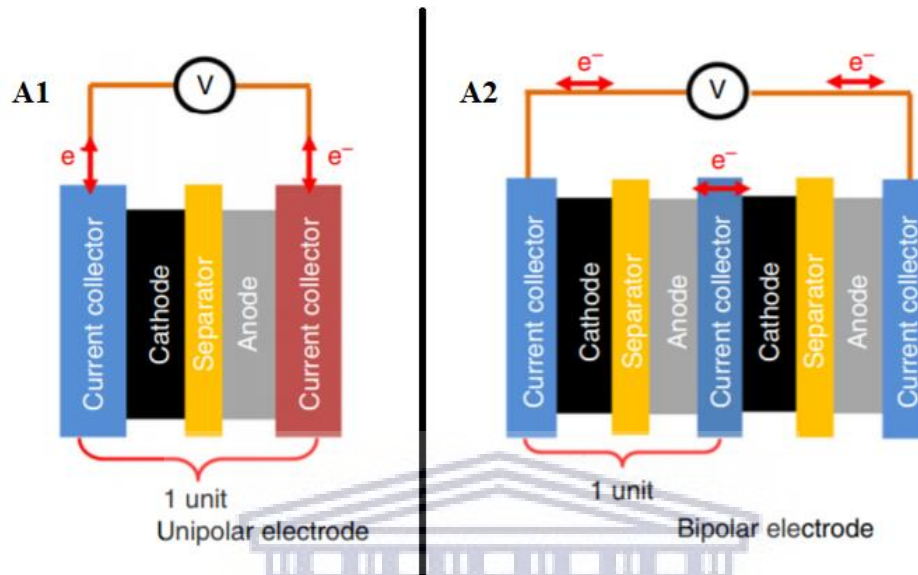


Figure 22 : A1-Schematic of the conventional unipolar electrode structure (one-unit cell) Vs A2-Schematic of the bipolar electrode structure (two-unit cell) [90].

The bipolar design allows solid-state lithium batteries to reduce the package weight and achieve a higher energy density as compared to a monopolar cell [91]. In the redox flow batteries, the polymer-graphite composite bipolar plates participate in the protection against corrosion and ensure good electrical conductivity, while also enabling a stackable construction for scaling up [92].

## 2.4 Summary of Literature Review

According to literature findings, the Ni-Fe battery is a good candidate for a low-cost energy storage systems, this technology is very suitable for stationary applications due to the nature of the abundant metals utilised in its construction [10], to their outstanding safety properties, and long cycle life [10][63]. However, there are several drawbacks to overcome first, such as:

- Significant electrolyte decomposition and the subsequent low coulombic efficiency
- Low utilisation of the electrode active material, in both anode and cathode.
- Inappropriate electrode manufacturing procedures and battery parts assembly.



- Hydrogen evolution reaction occurring at the Fe-based electrode.
- Conventional prismatic battery design.
- Relatively low power and energy density.

This study aims to optimise bipolar electrode production and battery prototype assembly. Some existing drawbacks within the Ni-Fe system were addressed by implementing the below-mentioned steps:

- **Nickel-based electrode material**

Optimisation of the electrode material is mandatory to achieve higher electrochemical performance while preserving the mechanical integrity of the electrode.

In this study, nickel hydroxide active material was sourced from an industrial supplier, using an industrial-grade material with cobalt as impurity. Cobalt hydroxide is found to enhance the electrochemical performance of nickel-based electrodes [93]. It was reported that Cu is responsible for enhancing the Ni–O interaction, resulting in a more stable structure of Ni(OH)<sub>2</sub> and extended cycling life [93]. Which explains the usage of copper as an additive at the electrode material preparation steps.

- **Current Collector**

In prismatic cells, the typical current collector is made from Ni foam or Ni mesh not without their challenges with regards to cost and durability in alkaline systems [10] respectively. Materials such as stainless steel, lead, silver, and carbon–polymer composite foils, have been used in the construction of bipolar electrodes for different batteries, such as lead-acid and nickel-metal hydride [94].

The current collector represents the backbone of the electrode due to its role in ensuring the electrical conductivity and the mechanical integrity of the electrode produced. The use of polymer-graphite composite bipolar plate in this study was one of the main reasons to establish a collaboration with Fraunhofer UMSICHT, since they developed an effective method to produce the bipolar plate on a large scale, essentially for redox-flow batteries applications. These bipolar plate are easy to machine and to weld, solving the important issue of seals and



potential electrolyte leakage [95]. The bipolar graphite plate offers a conductive substrate for electron transfer, which is stable in an alkaline medium and resistant to corrosion [92] and represents a low-cost alternative to metallic nickel substrates [87].

#### - **Binder**

During battery cycling, binders play a critical role in maintaining electrode integrity and preserving adequate contact between the cathode material and the current collector [96]. Polymer binders have electrical insulating and hydrophobic properties and are typically employed to achieve the required mechanical electrode integrity. It was reported that polyethylene powder, particularly the binder manufactured under the trade name Coathylene is used in dry cell batteries and alkaline batteries, due to its thermochemical resistance, adhesive properties and stability in alkaline medium. It was found to increase the electrode strength however an observed decrease in electric conductivity should not be ignored [97].

#### - **Conductive Additive**

Passivation phenomena and insulating behaviour of certain species during battery cycling, such as Ni(OH)<sub>2</sub> lower electrode conductivity. Besides, the electrically insulating nature of the polymeric binder employed to maintain the mechanical electrode stability forms a challenge in the creation of a continuous electrically conductive network that allows electrons to move between the electrochemically active materials and the current collector. In this study, the addition of carbon black or graphite has been employed to increase the electronic conductivity [14] [84].

#### - **Electrode Production Method**

Electrode production techniques available in the literature indicated that pasted type electrodes exhibit reasonable properties for the hot-pressing technique, demonstrating a higher electrochemical performance [83][65].

Thermoplastic composite material such as bipolar plates made from polymer-graphite composite is reformable and repairable; therefore it provides an easy way of fabrication and cost-effectiveness. Laser welding is usually employed in metal welding applications. The

thermoplastic composite material can be joined together using a laser beam where, the laser beam burns some of the polymers along its path and leaves a thin layer of molten polymer, resulting in a weld [42].

#### - **Battery Design**

The prismatic design offers a simple approach to construct batteries, where electrodes are assembled in a free-stand configuration. However, the bipolar design was found to;

- Reduce the overall weight of the battery [87]
- Improve the battery material utilisation [87]
- Reduce the number of parts mandatory for its construction [95]
- Allow a higher power density due to stackable configuration in which it is possible to deliver high voltage output in a small volume [89]

Bipolar designs required bipolar plates, the literature indicated that polymer-graphite composite bipolar plate offers a low-cost, good electrical conductivity, an easy way to machine and weld the adjacent cells, and prevent electrolyte leakage [95].

The implementation of the above-mentioned solutions is expected to achieve, a cost-effective and optimum performing Ni-Fe battery that offers an alternative solution in the field of stationary energy storage.

UNIVERSITY of the  
WESTERN CAPE

### 3 Experimental Methodology

The construction of the Ni-Fe bipolar battery undergoes several steps in its development and assembly process, the Iron electrode material is not being investigated in this study because it was prepared by a co-worker in the project, FeCu<sub>0.25</sub>/FeS based composition is developed and employed in the electrode production [100]. The electrolyte is a solution of 4.5 Molar KOH with 10% of lithium hydroxide additive [15]. This chapter contains various subsections that describe the different phases in the development of the bipolar Ni-Fe battery prototype. Section 3.1 describes the material, equipment, and methods used to develop a free-standing Ni-based electrode for the Ni-Fe battery in which the electrode composition and hot press parameters are optimised. Section 3.2 focuses on the development of bipolar electrodes and their optimised production parameters. Section 3.3 describes the assembly process for bipolar battery, followed by a description of material and electrochemical characterisation techniques in section 3.3

#### 3.1 Development of a free-standing Ni-based Electrode

Guided by the literature findings, the development of a free-standing electrode is an essential step towards the development of the appropriate Ni-based electrode composition. Electrode composition contained a majority of active material, in this case, the nickel hydroxide, representing more than 70%, on average, from the total composition of the electrode material, where the binder and the conductive substances, such as graphite, represent each 10%, and the remaining 10% is distributed on other chemical additives [98].

##### 3.1.1 Material and Chemicals

Table 2 presents a detailed list of chemicals that were used during this research, indicating their supplier and composition.

Table 2: Material and chemicals details

Material/Chemical	Supplier	Comp.	Details
Nickel hydroxide (NiOH <sub>2</sub> )	Bochemie	91 %	Particle size 2.5 µm to 150 µm
Nickel powder (Spherical Ni)	Alfa Aesar	99.8%	400 mesh
Copper powder (Spherical Cu )	Alfa Aesar	99.9%	100 + 325 mesh
Cobalt powder	Sigma Aldrich	99.8%	2 µm
Ni <sub>0.75</sub> Cu <sub>0.25</sub> powder	MEng student, Mr T Tawonezvi	Fe <sub>0.75</sub> Cu <sub>0.25</sub>	90 µm
Graphite	Alfa Aesar	99.9%	Universal grade, -200 mesh
Coathylene HA1592	AXALTA	99.9%	MP=105°C, (LDPE)
Nickel Mesh	Q-Lite Industrial Ltd.	99.9%	1mm aperture size, 1mm thickness
Graphite Bipolar Plate	Fraunhofer Umsicht	99.9%	80 % Graphite, 20 % PP, thickness 0.5mm

### 3.1.2 Equipment and procedures used for the development of a free standing Ni-based electrodes

Based on the various literature resources [68][84][14][10][81][83], the hot press method was employed to produce Ni-based electrodes. This production of a free-standing electrode entails the following;

- Nickel hydroxide, graphite, and coathylene binder are mixed using a blade mixer at room temperature for 2 min. The selection of the composition (80% active material. 10% binder 10% carbon black/graphite) was based on literature findings where the experimental electrode preparation indicates the usage of such proportions as starting point of reference before the incorporation of any other type of chemical additives[98].
- The hot press procedure is described in 3.1.2.2.
- Half of the mixture is transferred into a press mould (see section 3.1.2.1)
- A nickel current collector (Ni mesh) is carefully placed on top of the first half of the material layer.
- The other half of the powder is then added on top of the mesh to cover the two sides of the mesh.
- The mould is subsequently pressed at preselected temperature, pressure, and time.
- The optimisation of the hot press procedure is described in 3.1.2.2

A detailed description of the hydraulic press and the vacuum oven are provided in Appendix B.

### 3.1.2.1 Press Moulds

For the first experimental trials, two press moulds were designed and machined by the workshop at Fraunhofer UMSICHT, Germany. A photo of the produced moulds is included in both Figure 23 and Figure 24.



Figure 23: Face 1 of the press mould Version 1

Figure 24: Face 2 of the press mould Version 1

Cobalt and copper additives were found to enhance the electrochemical performance of the Nickel-based electrode [93]. For this reason, it was deemed appropriate to select industrial-grade material from (Bochemie) containing 91%  $\text{Ni}(\text{OH})_2$  and up to < 3% Cobalt hydroxide as a starting material for the production of Ni electrodes [99]. A commercial Ni-based electrode from Q-lite, China, was used as a benchmark to compare the mechanical stability and the electrochemical performance of the free-standing nickel electrodes produced in this work.

### 3.1.2.2 Hot-press parameters

After the mixing process, the electrode mixtures were spread uniformly on the mould, and then hot pressed on the Ni mesh. The produced electrode thickness was  $0.8 \pm 0.10$  mm, while  $0.15 \pm 0.1$  g.cm<sup>-2</sup> of active material was loaded onto the Ni mesh. The procedure was carried out under the following operating parameters depicted in Table 3.

It should be remembered that the melting point for the Coathelyne is 105° C. The polymer-based binders are treated below their melting point, in order for the electrode material to be linked without affecting the nature of the binder.

Table 3: Operating parameter for electrode hot pressing [100]

Parameter	Compacting Pressure ( kg.cm <sup>-2</sup> )	Temperature (°C)	Time (min)
Value	40	$97 \pm 2.5$	5

Free-standing electrodes provide a flexible and consistent way to perform experimental trials, the flexibility aspect is shown by the fact that small electrodes can fit into lab beakers without the need for cell construction. While trying to optimise the Ni-electrode performance. Ni-CB1, Ni-G1, and Ni-G-Cu1 represent the sample electrode compositions code, illustrated in Table 4.

Table 4 : Nickel-based free-standing electrodes and their compositions

	Ni(OH) <sub>2</sub> w%	Binder w%	Cu w%	Graphite w%	CB w%
Sample code	w%	w%	w%	w%	w%
Ni-Q-lite (Commercial electrode)	--	--	--	--	--
Ni-CB1	80	10	0	0	10
Ni-G1	80	10	0	10	0
Ni-G-Cu1	80	10	5	5	0

## 3.2 Development of bipolar electrode and fabrication process

Guided by the consulted literature, electrodes need to be produced in a bipolar format as illustrated in Figure 25. The background and pre-treatment of the bipolar plate will be provided in section 3.2.1. Section 3.2.2 describes the set of experiments conducted to optimise the hot

press procedure in an attempt to produce mechanically stable, electrochemically active bipolar electrodes with a reproducible appearance. The development of bipolar electrodes is an essential step towards the development of a bipolar battery.

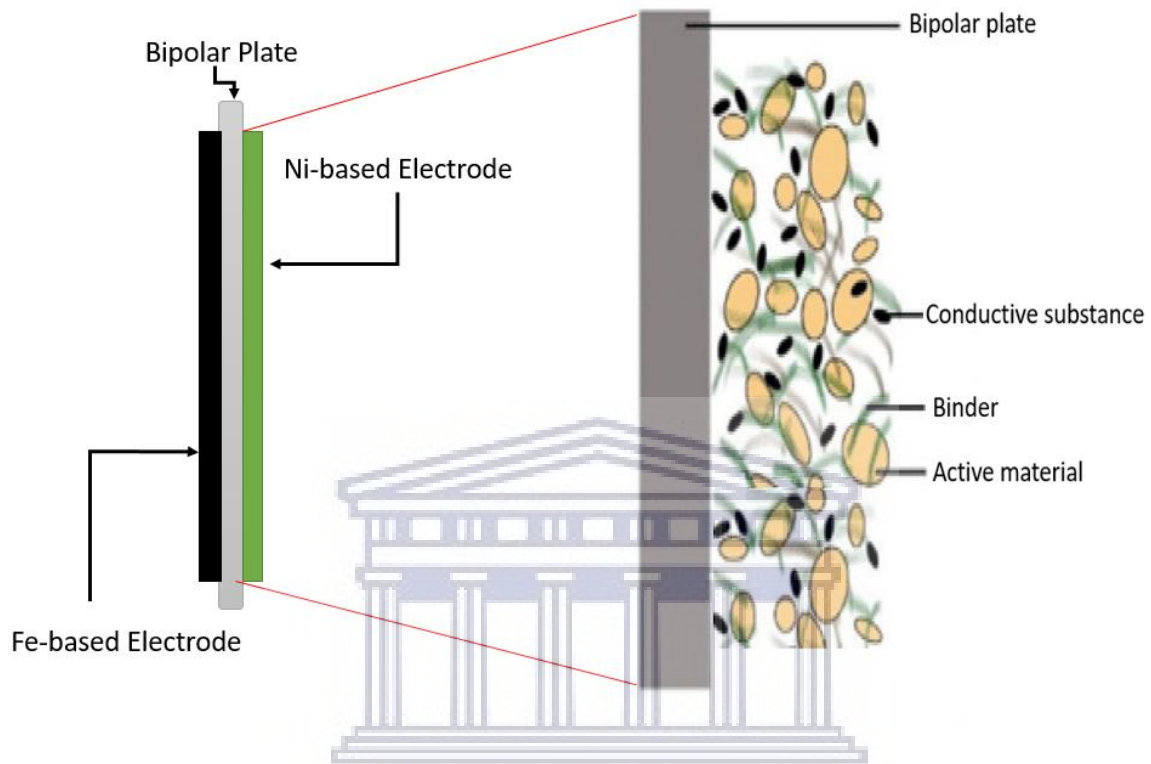


Figure 25: Bipolar electrode configuration

### 3.2.1 The bipolar plate

#### 3.2.1.1 Material properties:

The bipolar plates manufactured by Fraunhofer UMSICHT enable the production of large plates developed for redox-flow battery application. The electrons deliberated at the anode are feeding the cathode reaction at the other side of the bipolar plate. As depicted in Figure 25 the bipolar plates serve as the current collectors on both ends of the stacks. In this case, a laser-welding technique allows for the formation of a sealed connection between the bipolar plate (the thin, electron conductive material) and the surrounding plastic frames [101] (See Figure 26 ). Other applications are being investigated such as in the fuel cell field [101].



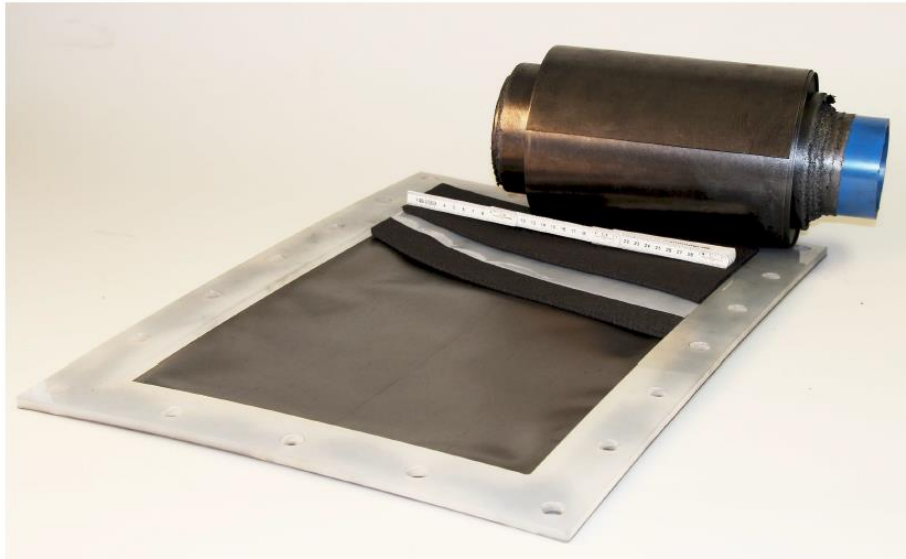


Figure 26 : Bipolar plate roll and sheets in its commercial form [101]

The produced bipolar plates are chemical resistant, mechanically stable, and gas-tight, they allow also subsequent formatting and reshaping [101]. Bipolar plate specifications are illustrated in Table 5.

Table 5 : Bipolar plate specifications [101]

Norm	Elastic modulus	Tensile strength	Filling grade		In-plane conductivity	Through-plane conductivity
DIN EN ISO 527-3	1100 N/mm <sup>2</sup>	7.4 N/mm <sup>2</sup>	80% Graphite	20% PP	250 S/m up to 5000 S/m	Less than in-plane conductivity by a factor of 10 to 100

The bipolar plates were made by Fraunhofer UMSICHT, using a roll to roll production process where the polymer (Polypropylene) constitute 20% of its composition, the rest is graphite (80%) which gives the bipolar plate its electro-conductive properties and make it a good candidate to substitute the normal nickel mesh as the current collector. Due to the potential advantages when using such a bipolar plate, the task was given to integrating the electrochemically active materials (the Ni and Fe based electrodes) with the bipolar plate. The challenge here was to establish and maintain an electrically conductive interface between is to

the relatively smooth surface of the polypropylene – graphite matrix and the electrode materials [102].

### 3.2.1.2 Bipolar plate pre-treatment

Modifying the roughness or the morphology of a substrate via mechanical surface treatments is considered to be an easy way to create irregularities that promote an effective mechanical interlocking between the substrate and the deposited material [103]. To produce durable and effective electrodes, a firm contact between the electrode material and the bipolar plate is desired. Improvements made to the contact between electrode materials and the bipolar plate will reduce electrical resistance and improve dimensional stability.

It appeared challenging to get the powdery electrode material to stick to the relatively smooth surface of the bipolar plate. Different approaches were performed to roughen the surface, starting with mechanical etching using 3200-grade micro-mesh sandpaper. A second approach involved the use of plasma. J. Azevedo et al. [103] reported that the surface energy of a polymeric substrate can be enhanced through plasma activation to strengthen the adhesion between the substrate and the coated material [103]. It appears that the organic material on the surface is oxidised and replaced by polar functional groups. The plasma pistol used in this work is shown in Figure 27.

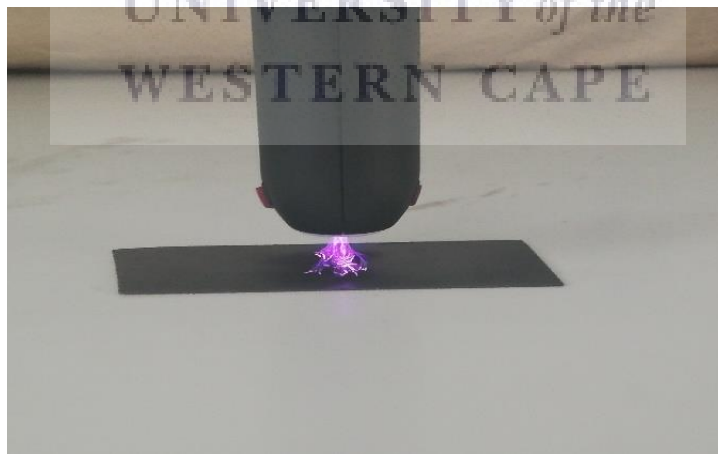


Figure 27: Bipolar plate treatment with the plasma pistol

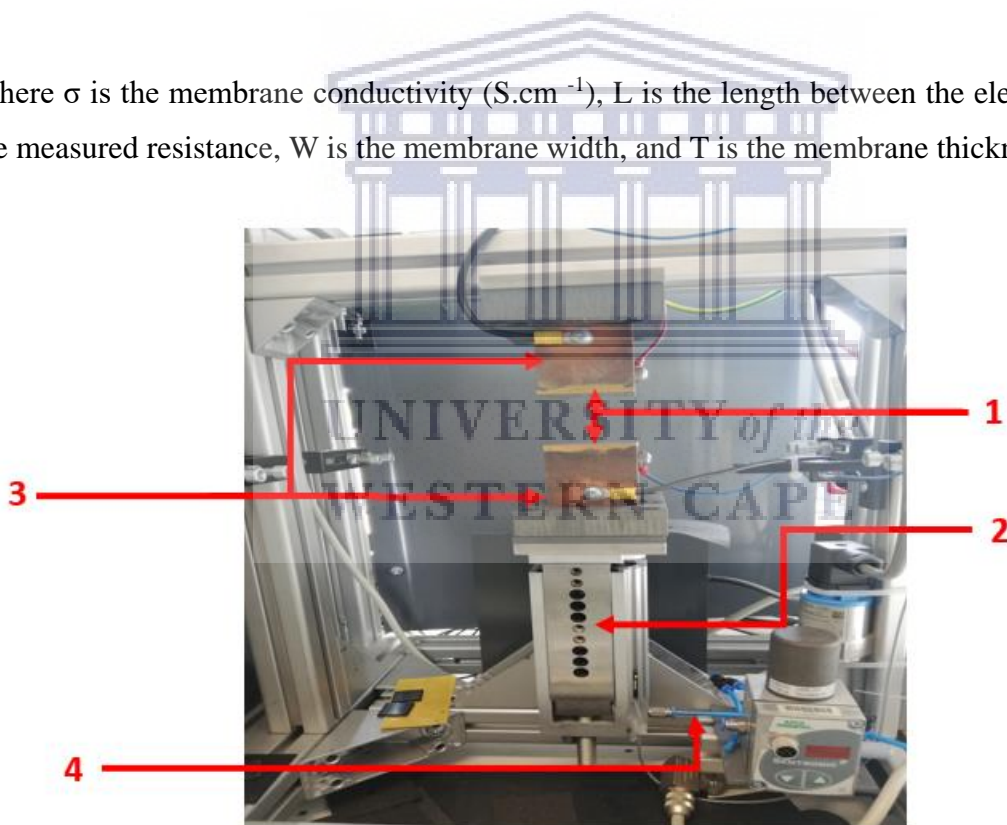
### 3.2.1.3 Conductivity tester

The through-plane conductivity of a bipolar plate sample is critically important because it largely affects the performance of batteries. A two-point probe was used to test the conductivity of electrode samples, as depicted in Figure 28.

Through-plane conductivity measurement is more meaningful than in-plane because electron transfer occurs in the through-plane direction. Because the conductivity of a material is directly linked with Ohmic losses, the conductivity of the bipolar plate or electrode can be calculated based on the measured resistance by the following equation:

$$\sigma = \frac{L}{RWT} \quad \text{Equation 16}$$

Where  $\sigma$  is the membrane conductivity ( $\text{S}\cdot\text{cm}^{-1}$ ),  $L$  is the length between the electrodes,  $R$  is the measured resistance,  $W$  is the membrane width, and  $T$  is the membrane thickness.



- 1 Gold plated surface
- 2 Pneumatic piston
- 3 Copper probes
- 4 Pressurised air tube

Figure 28: Two-point probe for conductivity measurements

### 3.2.2 Bipolar electrode optimisation

The initial attempt included the compression of commercial electrodes into the bipolar plates. The first experimental trials were conducted in A6 DIN bipolar plate format where a commercial nickel electrode (Q-lite, China) was cut and hot-pressed onto the bipolar plate according to the design dimensions. The quality of the electrode was determined based on three parameters; through-plane conductivity, the mechanical integrity of the bipolar plate (Presence/absence of cracks in the structure), and the powder adhesion to the bipolar plate (Presence /absence of material loss due to binder failure).

In the first trials, all operating parameters were kept constant while the hydraulic pressure was changed, according to Table 6.

Table 6 : Influence of Hydraulic Pressure

<b>Electrode processing parameters</b>				
Sample name	A1	A2	A3	A4
Mould version used	V1	V1	V1	V1
Cathode type	Q-lite	Q-lite	Q-lite	Q-lite
Pressing time (min)	5	5	5	5
Pressing temperature (°C)	110	110	110	110
Bipolar plate thickness (mm)	0.5	0.5	0.5	0.5
Hydraulic Pressure (MPa)	50	25	40	60

A second version of the press moulds (see Figure 29 ) was produced, the latter's were made of silicon, as an optimisation step towards producing a high-quality electrode.



Figure 29: Press mould Version 2

In a second trial, all other parameters were kept constant while the operating temperature was changed, the metallic mould was substituted by a silicon one, nickel-based material was mixed with some additives, graphite, and Coathelyne, then hot-pressed onto a bipolar plate using the operating parameters shown in Table 7.

Table 7 : Influence of Pressing temperature

Electrode processing parameters				
Sample name	B1	B2	B3	B4
Mould version used	V2	V2	V2	V2
Cathode type Ni(OH) <sub>2</sub>	In-House Composite	In-House Composite	In-House Composite	In-House Composite
Pressing time (min)	5	5	5	5
Pressing temperature (°C)	125	120	115	110
Bipolar plate thickness (mm)	0.5	0.5	0.5	0.5
Hydraulic Pressure (MPa)	25	25	25	25

In the third trials, the silicon mould was used; all other parameters were kept constant while the pressing time was changed, the operating parameters shown in Table 8.

Table 8 : Influence of Pressing time

<b>Electrode processing parameters</b>				
Sample name	C1	C2	C3	C4
Mould version used	V2	V2	V2	V2
Cathode type Ni(OH) <sub>2</sub>	In-House Composite	In-House Composite	In-House Composite	In-House Composite
Pressing time (min)	10	7	5	2
Pressing temperature (°C)	110	110	110	110
Bipolar plate thickness (mm)	0.5	0.5	0.5	0.5
Hydraulic Pressure (MPa)	25	25	25	25

Following the hot-press operation, the electrodes produced were examined to confirm the fulfilment of the dimensional requirements of the bipolar stack design. The electrode matching to the required dimensions was used in the battery stack assembly process as described in the forthcoming section.

### 3.2.3 Bipolar electrode production for the battery stack

The anode optimisation was conducted by a co-worker, involved in the same project, where his mission was to optimise the anode material to obtain an enhanced iron electrode, the output of his results was adopted, so based on the discharge capacity of both Fe-Cu anode powder (350 mAh.g<sup>-1</sup>) and Ni-based powder mixture (140 mAh.g<sup>-1</sup>), a single cell was designed to have 2.64 Wh cell capacity.

Taking into consideration that the Nickel-based electrode represents the limiting electrode of the cell, additional active mass loading is required compared to the anode. When it stacks, each bipolar electrode must have a precise thickness allowing approximately 8 g on the anode side and 16 g on the cathode to fulfil the design capacity.

The total electrode thickness was set at 3.5 mm, including a 0.5 mm bipolar plate, 1.5 mm anode material, and 1.5 mm cathode material according to the design requirements. The thickness of each side is designed to ensure mechanical stability during the laser welding process. Irregular electrode thickness will lead to compromising the integrity of the cells and engender possible electrolyte leaks if the welded bipolar plate undergoes severe internal stress.

The electrochemical surface area according to the DIN A6 design is set at 119.7 cm<sup>2</sup>. Two

moulds were designed according to the optimisation required during the electrode development. First trials were conducted using a steel machined mould as version 1. The silicon mould V2 is designed to allow 1.5 mm thickness on each side to integrate the separator in the assembly process without shortening the cells and allowing room for the electrolyte to ensure the ionic conductivity.

- Fe-based Electrode :

The iron electrode material was prepared by a co-work in the project, FeCu<sub>0.25</sub>/FeS based composition developed and employed in the electrode production. The Fe-based electrode exhibited a discharge capacity of 350 mAh during experimental tests. Dimensions of the Fe-based electrodes in their bipolar form are depicted in Figure 30.

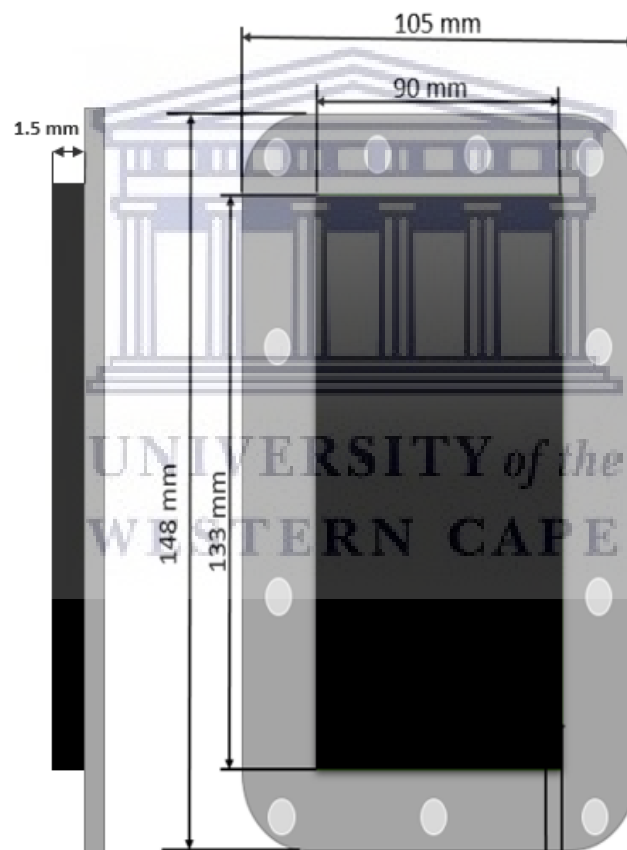


Figure 30: Dimensions of the bipolar Fe-based electrode

- Ni-based Electrode :

Ni-based electrodes were produced in-house using industrial-grade material, Figure 31, shows the dimensions of the bipolar Ni-based electrode.



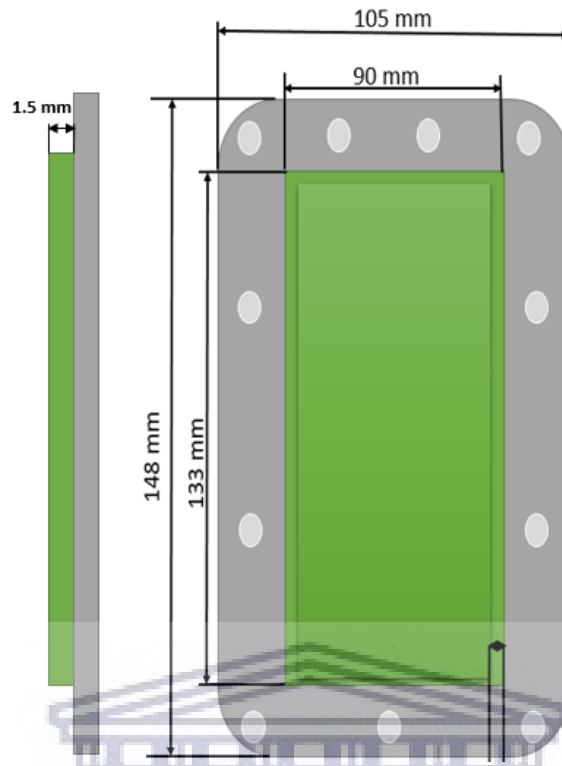


Figure 31: Dimensions of the bipolar Ni-based electrode

### 3.3 Bipolar battery stack assembly and testing

After producing the bipolar electrodes, the assembly process of the battery stack consists of overlaying the bipolar electrodes while introducing the separator frames in between, the layers are put together using a wooden frame, each cell is laser-welded separately before adding the next consecutive cell, after the laser welding the whole stack. Checking the mechanical integrity of the stack is essential before commencing the assembly step, which consists of introducing the copper current collectors together with outer PP frames while using screws to fix the whole battery stack.

#### - Separator :

Alkaline battery systems require a specific type of separators, where low cost and high rate capability is the main wanted qualities. Aspect such as thermal behaviour during discharge, the solubility of the electrode material in alkaline medium, and possible volume expansion during cycling in the Ni-based electrode must be considered[104]. Separator specifications of the Freudenberg separator are illustrated in Table 9.

Table 9 : Freudenberg separator specifications[104]

Specifications	Separator thickness	Fiber diameters	Heat resistance	Hydrolysis resistance
Nonwoven polymer fibers	150–200 $\mu\text{m}$ .	10–20 $\mu\text{m}$	120 °C	Resistant in alkaline medium

The porous separator will allow gas bubbles to migrate through and prevent the internal pressure build-up. Dimensions of the Freudenberg separator are depicted in Figure 32.

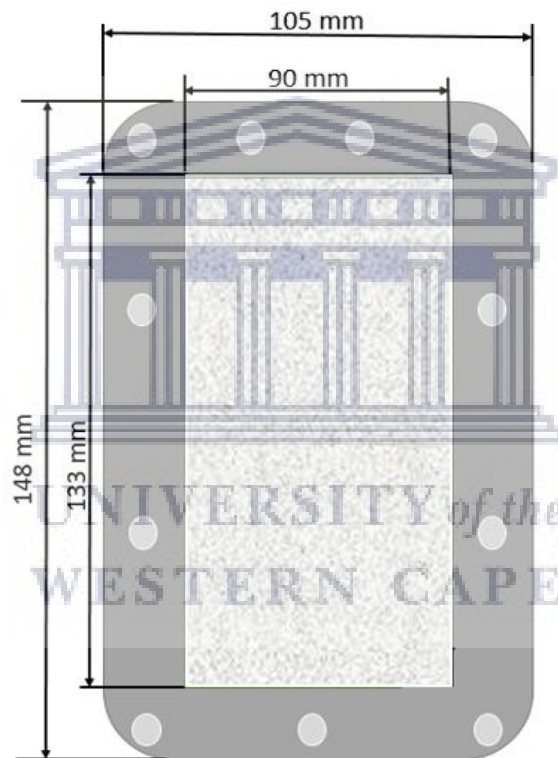


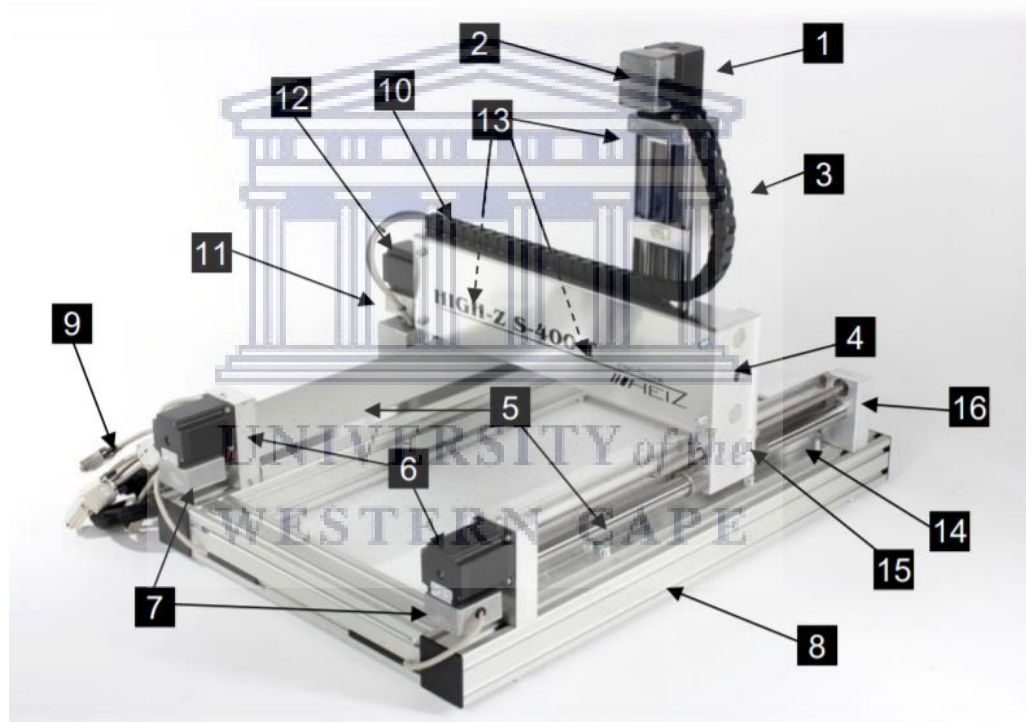
Figure 32 : Dimensions of the Freudenberg separator

### 3.3.1 Laser welding

During the laser welding process, plastic components are joined together through the absorption of laser energy. A bipolar electrodes (lower layer) and a frame components (upper layer) are clamped together, while a laser beam penetrates the upper layer, it is absorbed by the

lower layer which in turn is heated resulting in both parts, forming a bond that is virtually as strong as the base material.

Laser welding has several advantages, such as precise control of the welding area, bonding strength as strong as the base material, and avoiding costly and unnecessary parts, consequently reducing the price of the overall construction. As shown in Figure 33 the machine includes the complete mechanics for the three-dimensional movement of the laser source. The linear carriage-movement takes place via threaded spindles, powered by step motors. Two drives are used on the x-axis. The activation of the step motors, to operate every single axis, is done by using further interfaces. The operation procedure shows how to install, operate, and service a CNC-portal system.



1	Stepper motor of the Z-axis	9	Stepping motor control cable
2	Terminal box of the stepping motor of the Z-axis	10	Energy chain guide
3	Z-axis with carriage	11	Terminal box of the stepping motor of the Y-axis
4	Diode laser in Y-axis with carriage (Y-bridge)	12	Stepper motor of the Y-axis
5	X-axis with carriage	13	Reference switch XYZ
6	Stepper motors of the X-axis	14	Round bar guide
7	Terminal boxes of the step motors of the X-axis	15	Recirculating ball nut

8	Frame	16	floating bearing stopping blocks
---	-------	----	----------------------------------

Figure 33: Diode Laser welding machine

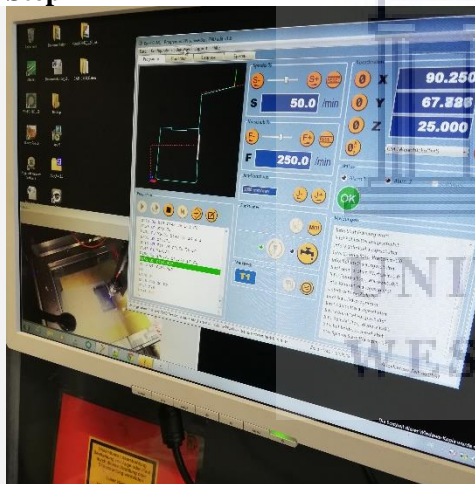
The machine cannot function alone, the following additional components (accessories) are necessary for operation:

- Control, which consists of a PC with the right configuration with struck up control software and a stepper motor control.

Four steps are required to obtain the welded cell on the bipolar plates, photos of the operation steps are summarised in Table 10.

Table 10: Laser welding steps

Step 1



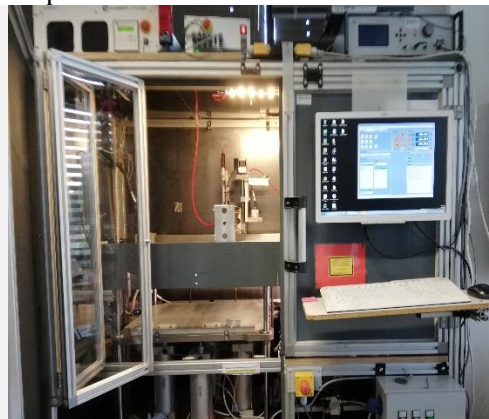
Step 2



Step 3



Step 4



Step one: Set up the Software with the schematics dimensions and program paths of the intended piece to perform the laser welding.

Step two: Place the cell in the right place under the laser source and apply the pressure test to test the adhesion between the glass surface and the cell underneath it.

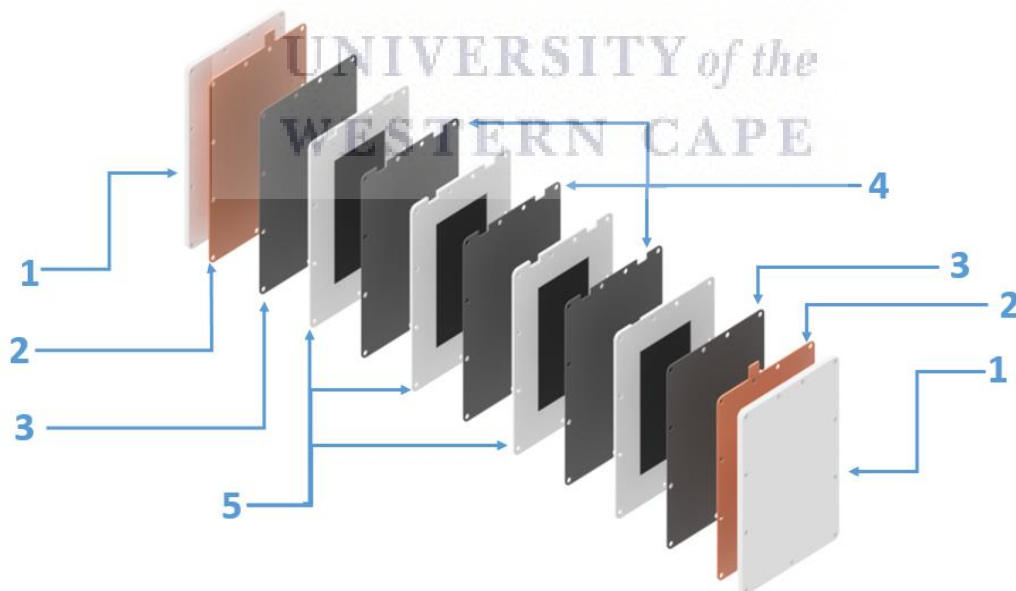
Step three: Start the program and monitor the laser welding operation.

Step four: Wait until the laser welding is done and take the welded piece out of the machine. A closed environment is needed to ensure safety of the operator.

### 3.3.2 Bipolar Ni-Fe battery construction

The battery assembly is the final step. In this step, a bipolar battery is constructed at Fraunhofer UMSICHT facility. Such bipolar Ni-Fe design exploits an innovative combination of optimised battery components and design in conjunction with the application of novel mass-production techniques.

As shown in Figure 34, the exploded view drawing of the bipolar Ni-Fe battery is detailed with the labelled components.



- 1 PP Outer Battery Covers
- 2 Nickel-plated Copper end-plate (Current Collector)

- 3 One-side coated electrodes
- 4 Bipolar electrodes
- 5 PP frames with Separator

Figure 34: Exploded view drawing of BiNiFe Battery

By employing the bipolar battery design, it is possible to save over 80 % of conventional battery materials such as electrolytes, insulating material and cables [87]. The bipolar plate design offers the most cost-effective battery solution. The process flow diagram adapted for the production of the bipolar Ni-Fe battery is shown in Figure 35.

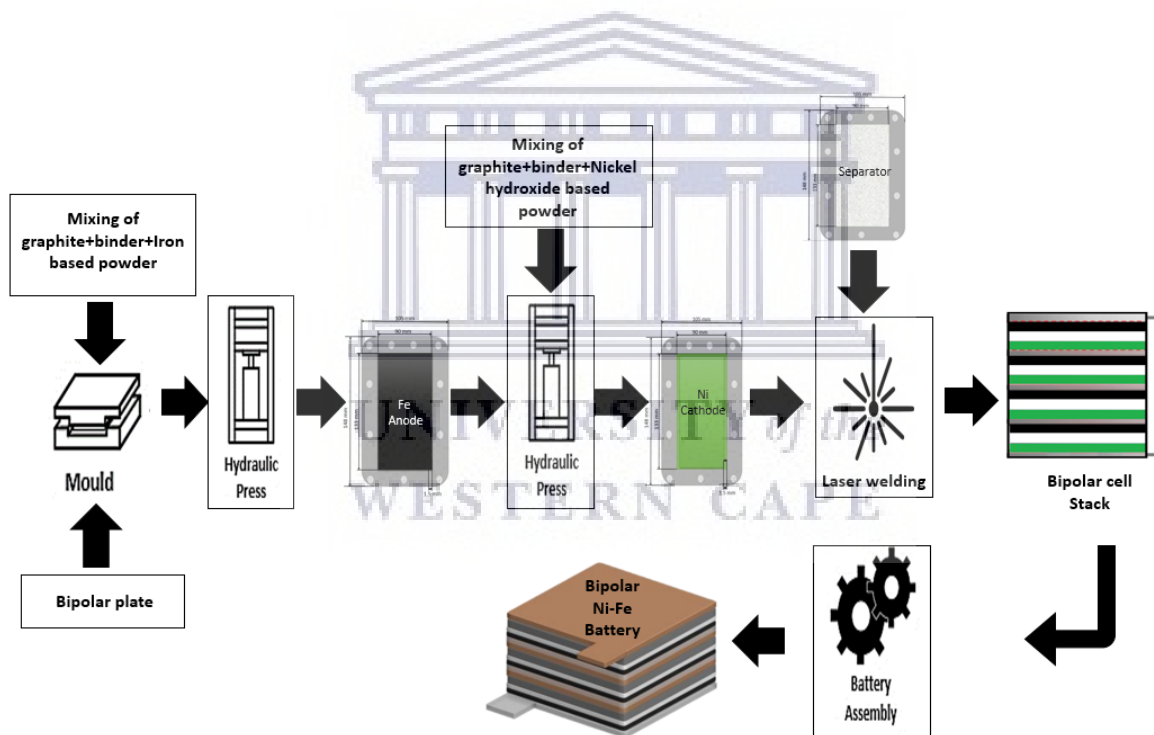


Figure 35: Schematic of Ni-Fe bipolar battery construction process

As shown in Figure 36, a schematic illustration of bipolar Ni-Fe battery prototype production with different process operations.

Electrode materials preparation is the first step towards the production of bipolar electrodes, this step consists of a series of operations, details as following:



- The mixing operation for 5 minutes was performed to provide the homogenisation needed.
- Nickel hydroxide active material was weighed and mixed with binder graphite and additives according to the specified ratios. The same operation was performed for the Fe-based material mixture.

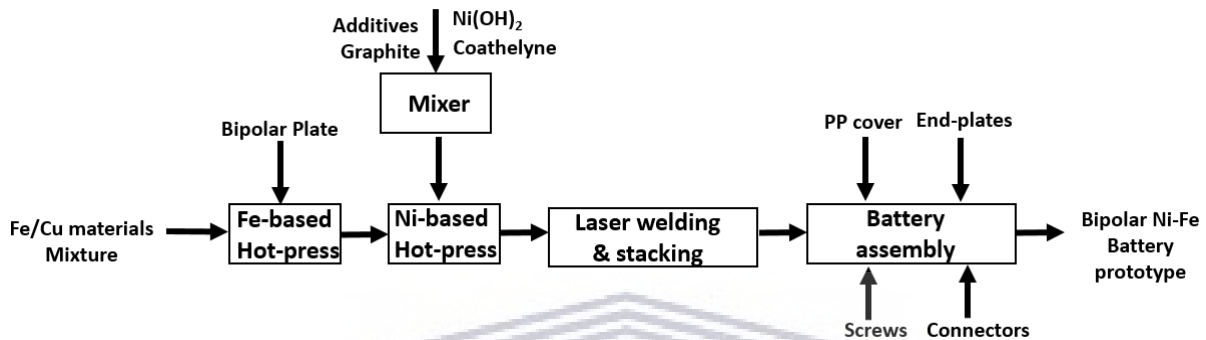


Figure 36: Schematic illustration of bipolar Ni-Fe battery prototype production

- The hot pressing step consists of placing the bipolar plate, then mounting the silicon frame on top, where the Fe-based active material mixture will be placed and manually spread on the mould surface. The hot pressing is performed according to the specific pressing parameters mentioned in (section 3.2.2 ). The Fe-electrode is then flipped on the backside where a second silicon frame is mounted to accommodate the nickel cathode material.
- The Ni-based active material is spread evenly on the mould and pressed into a bipolar form.
- The produced Ni-Fe bipolar electrodes are stacked and laser-welded to form a bipolar cell stack.
- Battery construction includes mounting the current collectors at the end of each side of the stack and placing PP cover to protect the battery from shortening, all components are assembled using M4 screws.



## 3.4 Physical Electrode Material Characterisation

### 3.4.1 X-Ray Diffraction

#### 3.4.1.1 Working Principle

Multiple types of interactions can occur when X-ray photons penetrate matter leading to different absorption and scattering effects. An elastic (coherent) scattering, also called Rayleigh scattering, occurs between the photons and the electrons surrounding the atomic nuclei [105].

As a result, the X-ray photons encroaching on all atoms of an irradiated volume are diffracted in all directions. It was reported that these X-rays are generated by a cathode ray tube, filtered to produce monochromatic radiation, collimated to concentrate, and projected into the crystalline sample [105].

The interaction of the incident rays with the sample formulates constructive interference signals (diffracted X-ray) obeying Bragg's law illustrated in Equation 17.

$$n\lambda = 2d \sin \theta$$

*Equation 17*

Where  $n$  is a positive integer,  $\lambda$  is the wavelength of the incident ray,  $\theta$  is the scattering angle, and  $d$  is the inter-planar distance (in Angstroms). Bragg's law relates the wavelength of electromagnetic radiation to the diffraction angle and the lattice spacing (interplanar distance) in the crystalline structure of the sample. The formulated diffracted X-ray signals are then detected, processed, and counted.

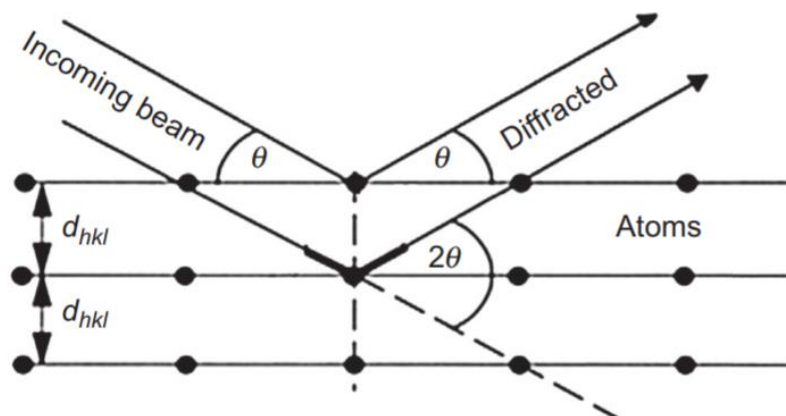


Figure 37: Geometrical condition for diffraction from lattice planes[105]

As shown in Figure 37, a range of  $2\theta$  angles is used to scan the sample, all possible constructive interference signals (diffraction X-ray) of the lattice should be obtained attributable to the random orientation of the crystals. Conversion of the diffraction peaks to d-spacing sanction the identification of the compound(s) in the sample because each compound has a set of unique d-spacing. Typically, the compound identification is attained by comparison of d-spacing with standard reference patterns[105].

#### 3.4.1.2 Procedure for XRD Analysis

The electrode materials were characterised by X-ray diffraction (XRD) using Huber G670 Leaflet as shown in Figure 38, located at Bochum University, Germany. The training was performed to operate the diffractometer under the supervision of a qualified technician, the training also included sample preparation and data collection.

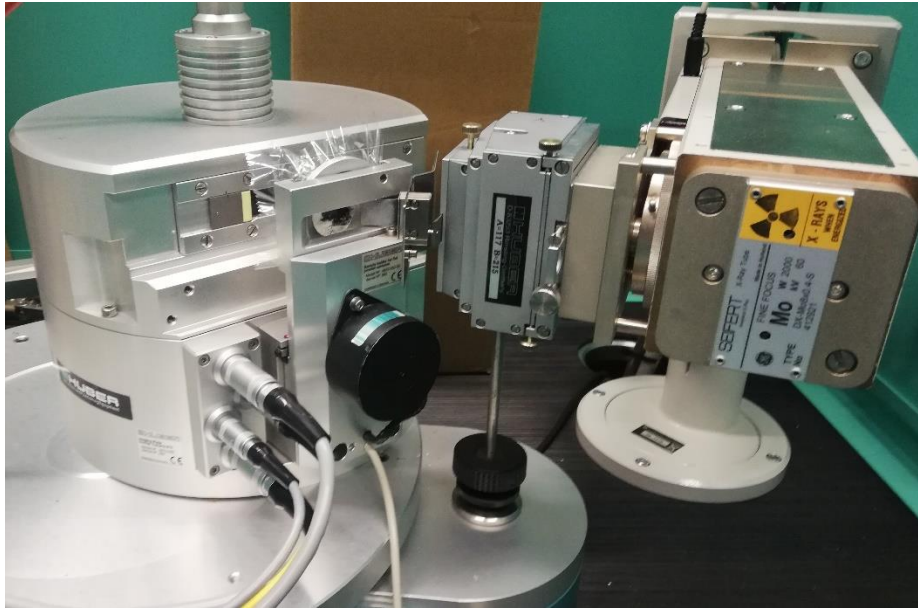


Figure 38: Huber G670 Leaflet -XRD Powder diffraction

## 3.4.2 Scanning Electron Microscopy

### 3.4.2.1 Working Principle

A scanning electron microscope (SEM) is defined as an electron microscope that generates images when a focused beam of high energy electrons hits the surface of the sample and scans it [106]. Information about the surface morphology and composition is generated when the electrons interact with atoms in the sample, generating various signals.

Coupling the frequency of the generated signal with the focus of the electron beam, formulates an image that can be exploited. Detection of secondary electrons emitted by atoms excited by the electron beam. The schematic diagram of a typical SEM is presented in Figure 39.

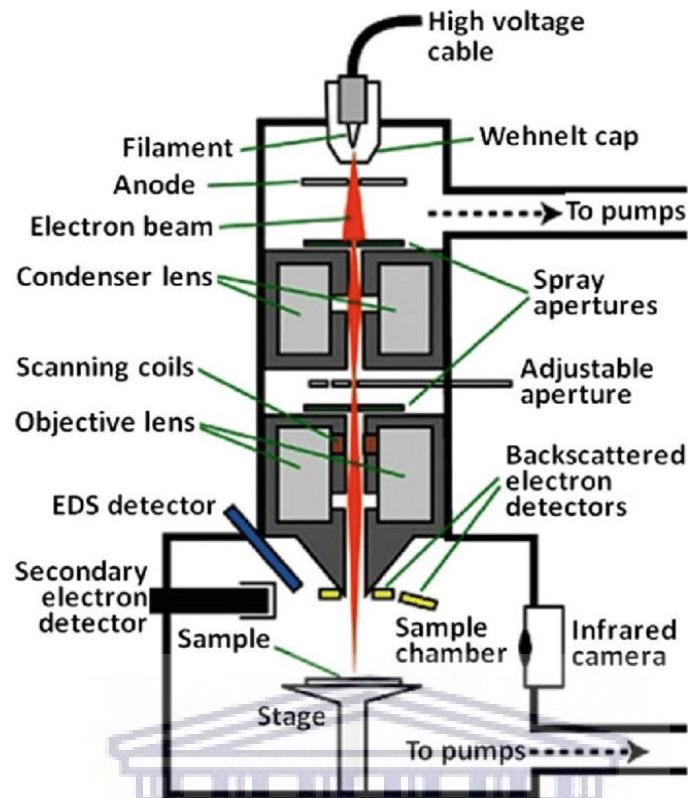


Figure 39: Schematic diagram of an SEM machine

### 3.4.2.2 Procedure for SEM Analysis

Sample preparation is a critical step towards achieving high-quality micrographs, as depicted in Figure 40, three major steps summarise this preparation, step 1, the samples must have an appropriate size to fit perfectly in the specimen chamber, this step includes sample cutting, step 2, then the sample is then mounted on the specimen holder also called specimen stub, Step 3 will be placing the stub into the testing chamber to start the vacuuming phase.

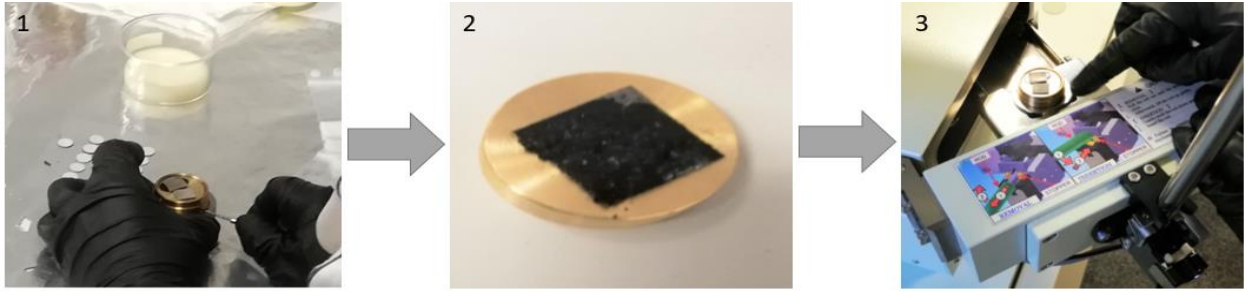


Figure 40 : Steps of sample preparation for SEM analysis

SEMs require a vacuum environment to work properly, without a vacuum, the generated electron beam would encounter interference with air particles in the surrounding atmosphere and even distort the tested sample. In the SEM apparatus used in this study, a standard vacuum pressure of 0.36 mPa was applied by the vacuum pump.

It is worthy of noting that the SEM imaging of all samples must be electrically conductive and electrically grounded, in this case, all samples were electrically conductive, and so no conductive coating was needed.

As shown in Figure 41, the morphologies of all electrodes were examined by a JSM-7500F Field Emission Scanning Electron Microscope (Ruhr-University Bochum) All samples were prepared and measured together with a qualified lab technician.



Figure 41: JSM-7500F Field Emission Scanning Electron Microscope

SEM examination can yield information about the electrode surface morphology when charged and discharged, unveil the influence of the electrochemical process on the stability of the Nickel-based electrode, especially that the later undergoes a swelling mechanism at during cycling .

## 3.5 Electrochemical Characterisation of Electrodes

### 3.5.1 Cycling Voltammetry

#### 3.5.1.1 Working Principal

Cyclic voltammetry (CV) is a technique that investigates the quantitative and qualitative behaviour and reactivity of electrochemical reactions. It allows the immediate identification of the redox potentials of the different electroactive materials examined. Electron transfer, adsorption reactions, and kinetics of the redox reactions are the information that can be collected when performing a CV analysis [107].

Cyclic voltammetry consists of linearly scanning the potential of the working electrode through a zigzag potential waveform. Figure 42 below illustrates the typical potential-time profiles created during the linear sweep and cyclic voltammetry.

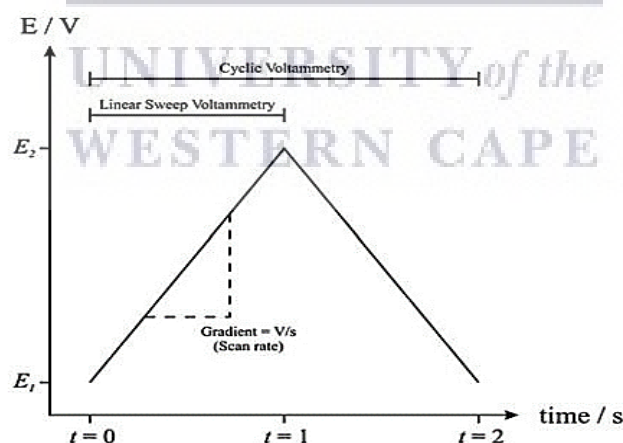


Figure 42: Potential-time profiles generated during the linear sweep and cyclic voltammetry

The scan rate expressed in  $\text{mV} \cdot \text{s}^{-1}$  defines the rate at which the potential is moved from  $E_1$  to  $E_2$ . linear sweep voltammetry is considered when the potential sweep is stopped at  $E_2$  [107].

A full potential cycle is achieved when the potential returns back to potential  $E_1$ , described as



cyclic voltammetry. Multiple cycles can be performed depending on the material studied. The current resulting from the potential screening is measured via the potentiostat. A voltammogram contains the current versus potential plot as shown in Figure 43 called a cyclic voltammogram, CV depending on various factors such as time and chemical and physical properties of the sample [107].

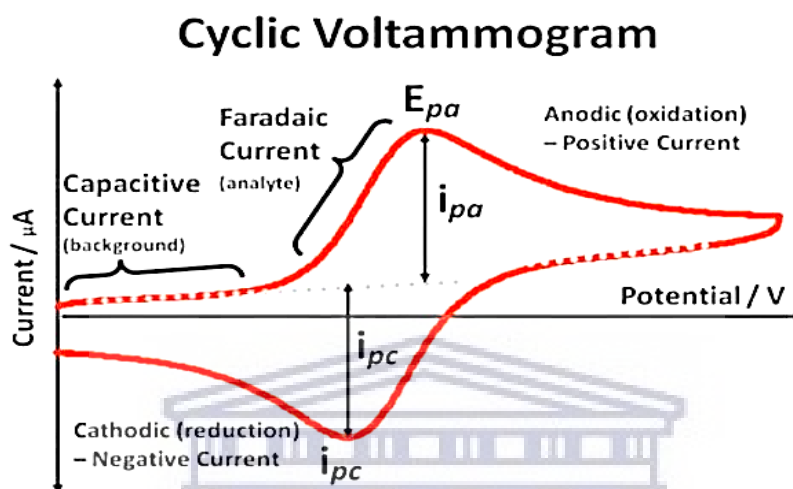


Figure 43: Cyclic voltammogram plot analysis [107]

As shown in Figure 43 the voltammogram illustrates the anodic peak showing the oxidation reaction and the cathodic peak where the reduction takes place. The potential window is set prior to starting the CV considering the standard potentials of electroactive species to be within the set potential window.

### 3.5.1.2 Procedure for Cycling Voltammetry

An Electrolyte solution of 6 M KOH/1 M LiOH is prepared to conduct the CV, The experimental set up is made of three electrodes, the working electrode which is a Ni-based electrode, a Pt electrode as a counter electrode and Hg/HgO as a reference electrode are connected to the ZENNIUM pro potentiostat/galvanostat system depicted in Figure 44 [108].





Figure 44: ZENNIUM pro potentiostat / galvanostat[109]

The ZENNIUM pro is a potentiostat/galvanostat electrochemical workstation equipped with a frequency response analyser unit ranging approximately up to 8 MHz at  $\pm 3$ . The voltage can reach up to  $\pm 28$  V [109]. The power cell multiplexer PMux shown in Figure 45, is connected to the potentiostat/galvanostat to allow multiple cell testing with a maximum current range up to  $\pm 5$  A [109].

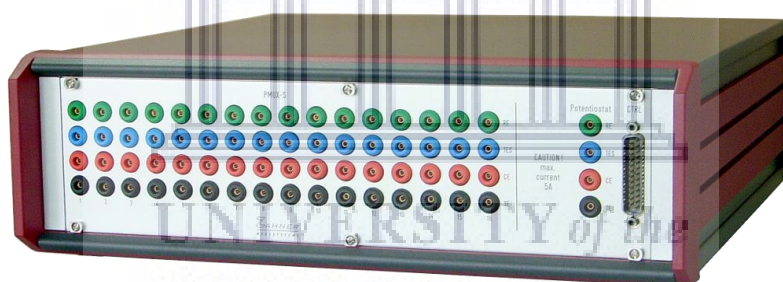


Figure 45: Power cell multiplexer PMux [109]

Figure 46 shows the experimental testing configuration for cycling voltammetry. The three electrodes are immersed in the electrolyte, gas tightness conditions are also important to acquire precise results.

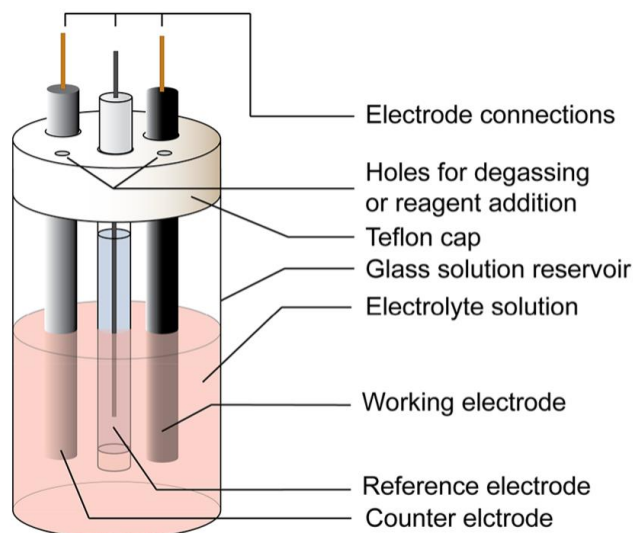
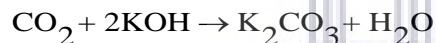


Figure 46: Experimental testing configuration for cycling voltammetry [108]

To prevent side reactions that can interfere with the reaction being studied, the cell must be sealed to inhibit the CO<sub>2</sub> in the air from reacting with KOH, and the reaction is illustrated in the below mentioned Equation 18.



*Equation 18*

This above-mentioned reaction is prevented by using gas tightening accessories. In cases where the gas tightness is not utilised, the electrolyte concentration can be drastically affected. Consequently, the measured results will not be accurate.

Temperature control is also important since the electrolyte conductivity is dependent on the temperature and thus a temperature control is added to the testing set up.

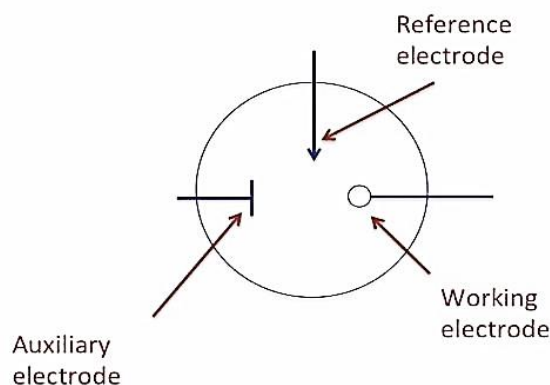


Figure 47: Schematic of the electrode configuration (Top view)

CO<sub>2</sub> is displaced out of the cell using a Nitrogen gas flow introduced into the cell via an in/out tube connection during the test execution to prevent the potassium carbonate generation in the electrolyte.

The electrodes are connected to the potentiostat using connector clips, the measurements are recorded at different scan rates and within a potential range from -1.5 to 1.5 V.

### 3.5.2 Galvanostatic Charge/Discharge

#### 3.5.2.1 Working Principle

Galvanostatic charge/discharge cycling consists of exposing the working electrode to constant current where the potential is determined against a standard potential of a reference electrode as a function of time [110]. The initial current applied in the electrode is usually lower than the limiting current, consequently, the voltage is suddenly decreased due to the ohmic potential effect ( $I \cdot R$  loss), then, due to the mass transport limitations, the concentration of the reactants is lowered at the electrode surface leading to an overpotential [110].

The diffusion mechanism cannot deliver the required current flow when the current is higher than the limiting current so, the electrode potential keeps increasing until it reaches the next reaction potential. Oxidation/reduction occurs at a constant rate during the galvanostatic cycling, following the anodic/cathodic applied current.

The electrode potential evolves with time as the concentration of the reactant species and product species changes at the electrode surface. When the concentration of the reactant at the

electrode surface is almost equal to zero, the amount of the reactant can be insufficient to accommodate all the electrons generated by the constant current flux. Consequently, the voltage will move to more anodic or cathodic values.

The profile of the curves is governed by the electrochemical reversibility of the active material on the working electrode. As shown in Figure 48, Different types of chronopotentiometry curves are illustrated, when the current applied is shifted from anodic to cathodic reaction, the anodic product formation takes place, but when the reaction moves to the cathodic direction, the cathodic products are increased.

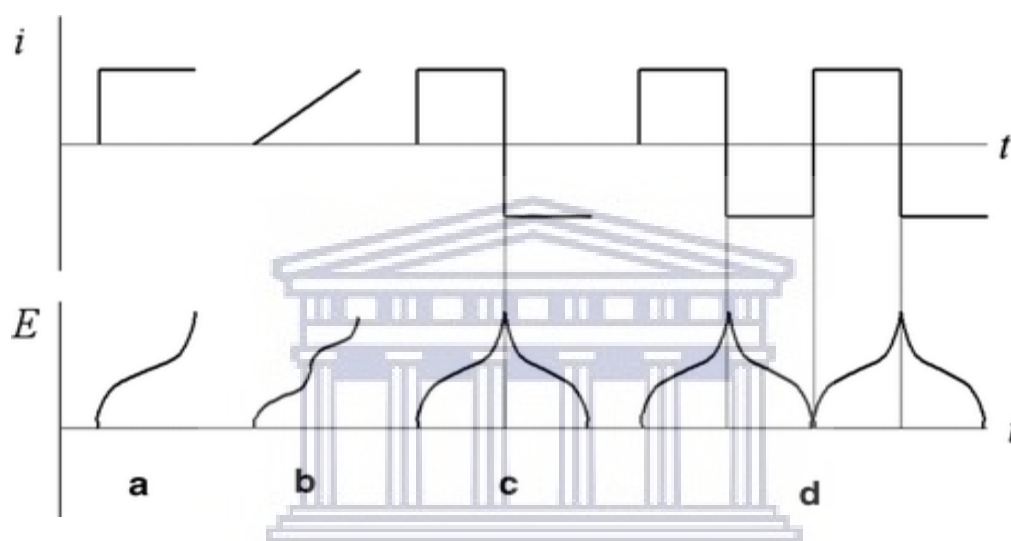


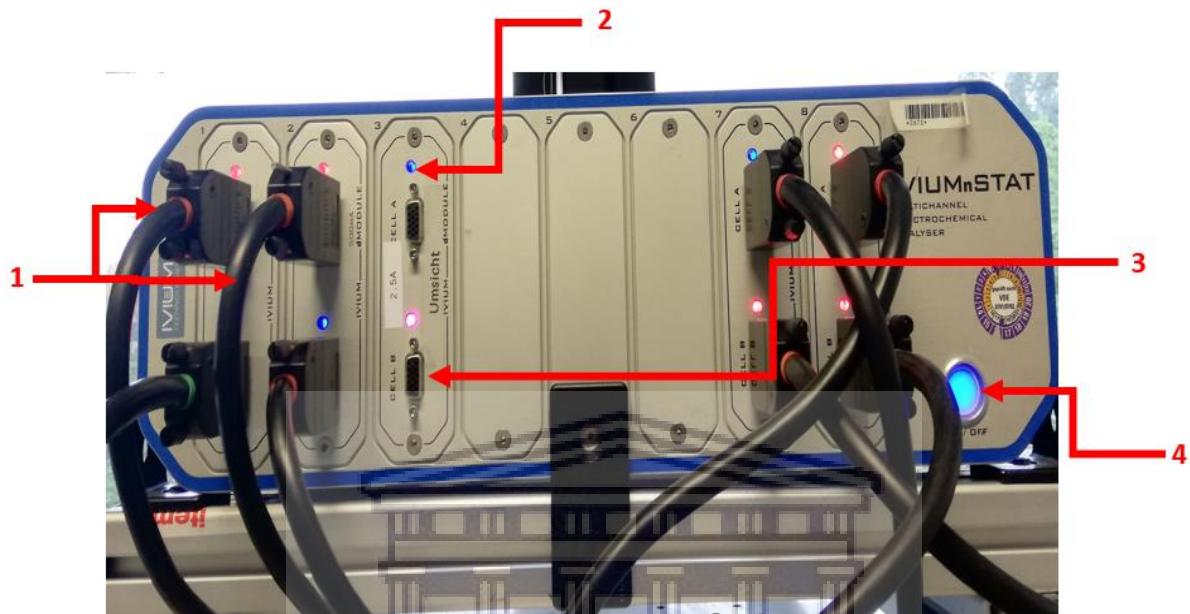
Figure 48: Different types of chronopotentiometry experiments: (a) constant current chronopotentiometry, (b) linearly rising current chronopotentiometry with linearly, (c) current reversal chronopotentiometry and (d) cyclic chronopotentiometry [110]

Galvanostatic measurement techniques are performed to characterise the properties of the electrochemically active materials by applying a cyclic galvanostatic program to evaluate the energy efficiency, the specific capacity, and lifetime stability of the produced electrode or the battery stack. Typical charge /discharge curves of the Ni-Fe cell, are obtained at a rate of 0.2C, [60]. The total capacity of the active material stored in the electrodes can be calculated during the discharge cycle of the battery at a 0.2C rate and expressed in terms of  $\text{mAh}\cdot\text{g}^{-1}$  or  $\text{C}\cdot\text{g}^{-1}$ . When the electrode reaches an equilibrium state, the accepted charge can be equivalent to as many as several moles of active mass. The various steps of the redox reactions can be characterised and identified using the galvanostatic charge /discharge curves during the electrochemical process.

### 3.5.2.2 Equipment for Galvanostatic Analysis

- **Hardware and software for Galvanostatic Analysis**

In order to conduct the galvanostatic cycling measurement, an IVIUM battery testing system is used as illustrated in Figure 49.



- 1- Cables
- 2- Channel Power and Signal LED
- 3- Channel plug
- 4- Power On/Off

Figure 49: Front panel of the IVIUM battery testing station

- **Software**

The host computer software of IVIUM battery testing station consists of integrated measurement and data analysis software.

### 3.5.2.3 Procedure for Galvanostatic Analysis

- **Start-up and Operation**

Start-up: set steps on the battery channel, start channels work according to the setting step: including constant current discharge, constant current charge, constant voltage charge, constant current constant voltage charge, constant power discharge, rest, cycle, etc.

- End: The working channel will automatically stop after completion of all settings of the steps, while users can request the program to be stopped whenever.
- Resume: for resuming a stopped channel, use “resume restoring the original testing process and maintaining data.
- Jump: the users can force a stop in the current step of the channel and jump the target steps to continue the test.
- Move: the user can move the current step to the target channel, and the original stops.
- Channel info: Query the situation of the working channel;
- Open Data: for working channel data (Voltage, current, capacity, and cycles) for real-time display.

In the step set column, users can set up the testing process, meanwhile set “the record condition” and “protect param” and other restrictions. The types of step utilised include a total of ten: Constant Current (C\_C) Charge, Constant Current (C\_C) Discharge, Constant Voltage (C\_V) Charge, Constant Power (C\_P) Discharge, Constant Resistance (C\_R) Discharge, CC\_CV Charge, Rest, Pause, Cycle, End, Step over conditions including current, time, voltage, capacity and change in the voltage ( $-\Delta V$ ).

- C\_C charge: the parameter of the current must be set; the user can set the step over conditions according to different requisites of the test.
- C\_C discharge: The parameter of current must be set; the user can set the step over conditions according to different requisites of the test.
- C\_C charging: the parameter of voltage must be set; the user can set the step over the conditions according to different requisites of the test.

The above-mentioned programs are the most employed programs for galvanostatic analysis.

- **Electrochemical Activation**

Throughout the whole activation/formation period, the cells were placed in a water bath at a temperature of  $25 \pm 2$  °C. Cells were connected to a battery management device where they undergo a series of charge/discharge cycles for X (10-20) cycles until a steady capacity was attained, each cycle comprised of:

- a) A rest step of 30 minutes
- b) A charge step at current, of  $(I=50 \text{ mA.g}^{-1}$  with voltage limit,  $V_{\text{max}}=1.65 \text{ V/Cell}$ )
- c) A discharge at current, of  $(I=50 \text{ mA.g}^{-1}$  with voltage limit,  $V_{\text{min}}=0.8 \text{ V/Cell}$ )
- d) A rest step for 30 minutes

- **Cycling Test**

Throughout the whole test period, the cells were placed in a water bath at a temperature of  $25 \pm 2 \text{ }^\circ\text{C}$ . Cells were connected to a device where they undergo a series of discharge cycles for 40 cycles, each cycle comprised of:

- a) A rest step of 30 minutes
- b) A charge step at current, in amperes, of  $I=100 \text{ mA.g}^{-1}$  with voltage limit,  $V_{\text{max}}=1.65 \text{ V/Cell}$
- c) A discharge at current, in amperes, of  $I=100 \text{ mA.g}^{-1}$  with voltage limit,  $V_{\text{min}}=0.8 \text{ V/Cell}$
- d) A rest step for 30 minutes

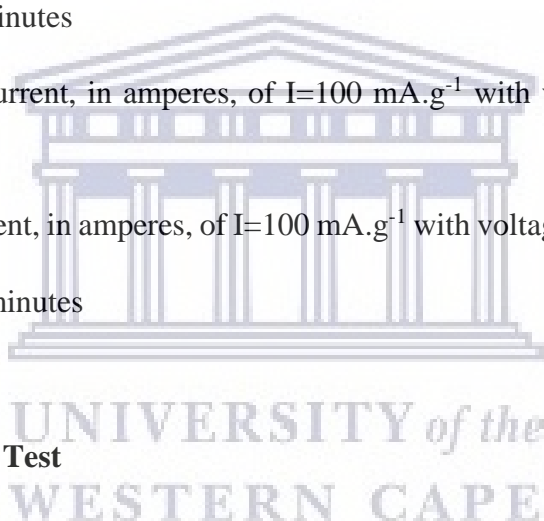
- **Charge Retention Test**

Throughout the test period, the cells were placed in a water bath at a temperature of  $25 \pm 2 \text{ }^\circ\text{C}$ . The cells were connected to a charging device. The charge step comprised of:

- a) A charge step at current, in amperes, of  $I=100 \text{ mA.g}^{-1}$  with voltage limit,  $V_{\text{max}}=1.65 \text{ V/Cell}$

After fully charging, the cells were stored for 10 days. After this storage period, the cells were discharged, the discharge step comprised of:

- b) A discharge at current, in amperes, of  $I=100 \text{ mA.g}^{-1}$  with voltage limit,  $V_{\text{min}}=0.8 \text{ V/Cell}$
- c) A charge step at current, in amperes, of  $I=100 \text{ mA.g}^{-1}$  with voltage limit,  $V_{\text{max}}=1.65 \text{ V/Cell}$





- **Polarisation Test**

Throughout the whole activation/formation period, the cell was placed in a water bath at a temperature of  $25 \pm 2$  °C. Cells were connected to a battery management device where they underwent a charge step and then discharge at a specific current for 5 seconds with the voltage output measured at each specific current, each cycle comprised of:

- a) A rest step of 30 minutes
- b) A charge step at current, in amperes, of  $I=1000 \text{ mA.g}^{-1}$  for 90 mins
- c) A discharge at current, in amperes, of ( $I=200-2500 \text{ mA.g}^{-1}$ ) for 5 seconds
- d) A rest step for 30 minutes



## 4 Results and Discussion

This chapter contains various subsections that discuss the different results of the development of the bipolar Ni-Fe battery prototype. Section 4.1 discusses the results generated of the free-standing Ni-based electrode. Section 4.2 illustrates the optimisation results generated by the optimisation of the bipolar electrodes by discussing the material and electrochemical characterisation results. Section 4.3 describes the outcome of the assembly process of bipolar battery prototype, cycling results followed by post-mortem analysis.

### 4.1 The development of a free-standing Ni-based Electrode

Table 11 shows the electrode composition and specific discharge capacity for 4 different electrodes. The electrodes all weighed 16g of active material mixture and were charged and discharged for 60 times at 100mA as an activation step.

Table 11 : Nickel electrodes composition and performance

Sample code	Ni(OH) <sub>2</sub>	Binder	Cu	Graphite	CB	Capacity mAh.g <sup>-1</sup>		Mechanical stability
	w%	w%	w %	w%	w %	10 <sup>th</sup> cycle	60 <sup>th</sup> cycle	
Ni-CB1	80	10	--	--	10	60	45	Inadequate, materials loss and electrode degradation
Ni-G1	80	10	--	10	--	127	111	Reasonable, no noticeable physical electrode deterioration
Ni-G-Cu1	80	10	5	5	--	141	131	Reasonable, no noticeable physical electrode deterioration
Ni-Q-lite (Commercial electrode)	--	--	--	--	--	90	71	Inadequate, Electrodes starts to disintegrate after 60 cycles

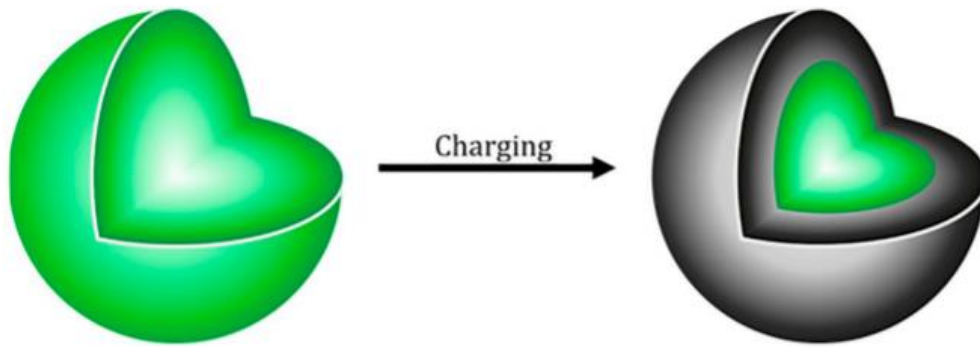


Figure 50: Schematic of nickel hydroxide colour change after the first charging process [111]

Figure 50 shows a theoretical schematic of the active material change that undergoes after the first charging process, the colour difference between the electrode loaded with precursor active material and activated  $\text{Ni}(\text{OH})_2$  electrode after cycling, the active material surface undergoes an oxidation reaction during charge, subsequently, the starting active material colour changes from green to black indicating that the nickel hydroxide is converted to nickel oxyhydroxide as verified by the experimental trials depicted in Figure 51.

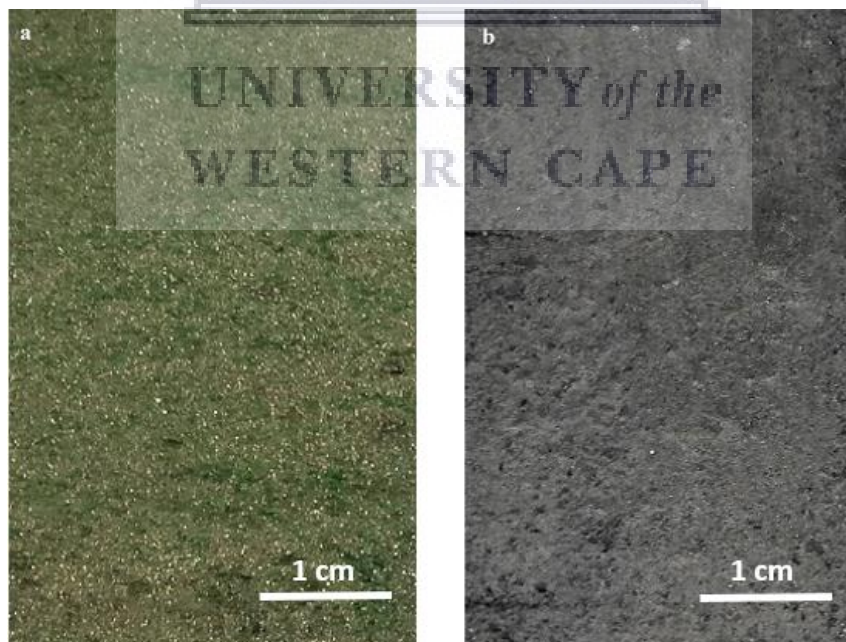


Figure 51 : Ni-G1 electrode surface (a) before and (b) after the first charge

The flaky appearance of the Ni-CB1 electrode surface can explain the poor mechanical stability of the electrode. Substituted of carbon black by graphite with relative large grain size (mean particle size of 125  $\mu\text{m}$ ) assisted to create a far more stable structure. The graphite appears to play an important role in maintaining the electrode's mechanical integrity during the cyclic swelling of the  $\text{Ni}(\text{OH})_2$  and  $\text{NiOOH}$  components respectively. The transformation of  $\text{Ni}(\text{OH})_2$  (green) and  $\text{NiOOH}$  (black) is observed after the first charging process as depicted in

Figure 52 shows the electrode surfaces of Ni-CB1 and Ni-G1. The electrode with CB (Ni-CB1) appears to have a rough surface while the electrode with graphite (Ni-G1) appears more smooth and solid.

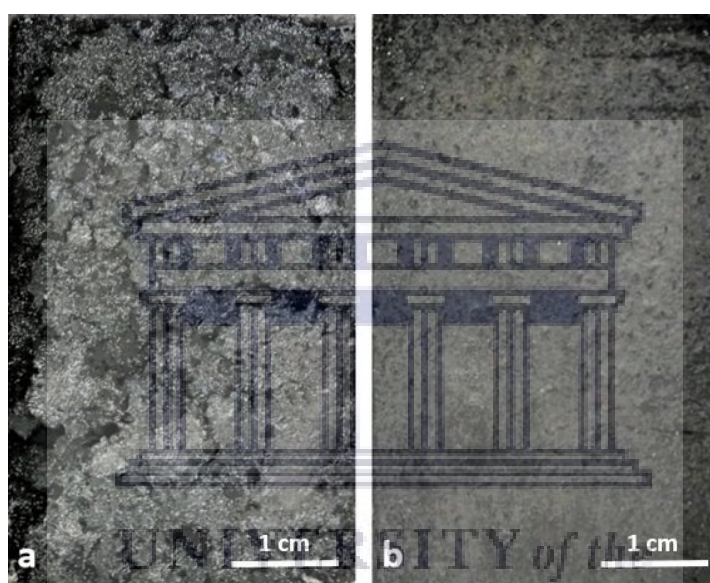


Figure 52 : Photos of the Nickel-based electrode surface after cycling (a) Ni-CB1, (b) Ni-G1

The electrode with 10% Carbon Black (CB) was mechanically unstable and showed the poorest performance. When the CB was substituted for Graphite a substantially more stable electrode was obtained with reasonable charge/discharge performance and stability of 127 and 111 after 10 cycles and 60 cycles respectively (Ni-G1). The results obtained were compared with previous trials on Ni-CB1, which depicted that graphite has the potential to stabilise the mechanical structure of the electrode due to its structure and thereby improve the discharge capacity of the  $\text{Ni}(\text{OH})_2$  by inhibiting the active mass losses during cycling.

The demonstrated specific discharge capacity of the industrial-grade nickel hydroxide is considered to be better than the Q-lite electrode material and represented the base case to further improve the cathode capacity and enhance the utilisation of the  $\text{Ni}(\text{OH})_2$  active material.

Further modification of this electrode with 5% Cu-powder yielded the most active electrode with a charge/discharge performance of 141 and 131 after 10 cycles and 60 cycles respectively (Ni-G-Cu1). For comparison, the charge/discharge performance of the commercially available electrode was measured to be 90 and 71 after 10 cycles and 60 cycles respectively, a rather poor performance for a commercially available electrode. The demonstrated low specific discharge capacity may be the result of lower conductivity of the material resulting in poor utilisation of the Ni(OH)<sub>2</sub> active material.

Specific discharge capacity calculation:

$$\text{Specific discharge capacity} = \frac{\text{applied current (mA)} \times \text{discharge time (hours)}}{\text{A loading mass (g) of the active material}}$$

As shown in, Table 11 specific discharge capacity increases with an increase in weight percentage addition of copper powder. As shown in Figure 53, the addition of copper powder 5 wt. %, showed a higher capacity. Based on the results obtained it was therefore concluded that the optimum electrode composition to apply is the one with 5 wt.% copper powder, 55 wt.% Graphite, 80% Ni(OH)<sub>2</sub>, and 10% Coathelyne the optimum percentage needed to improve the utilisation of Ni(OH)<sub>2</sub> active material in this current research.

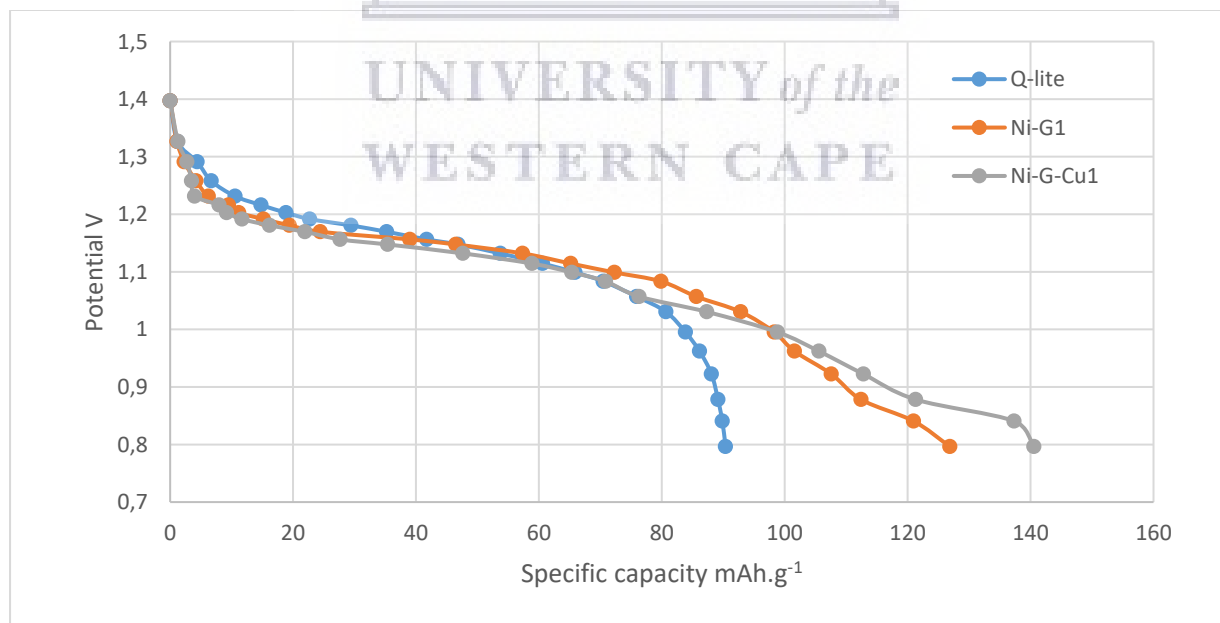


Figure 53 : Discharge curves of Q-lite commercial electrode, Ni-G1 and Ni-G-Cu1 from 1.4 to 0.8 V at 100 mAh.g<sup>-1</sup>

The active material selected was then cycled for 60 cycles to test the stability of the active material. The results were also compared with the active material without the addition of copper

powder. While the Ni-G-Cu1 electrode demonstrated a 10 % increase in discharge capacity after 60<sup>th</sup> cycles, the Ni-G1 electrode was fairly stable after the 60<sup>th</sup> cycle.

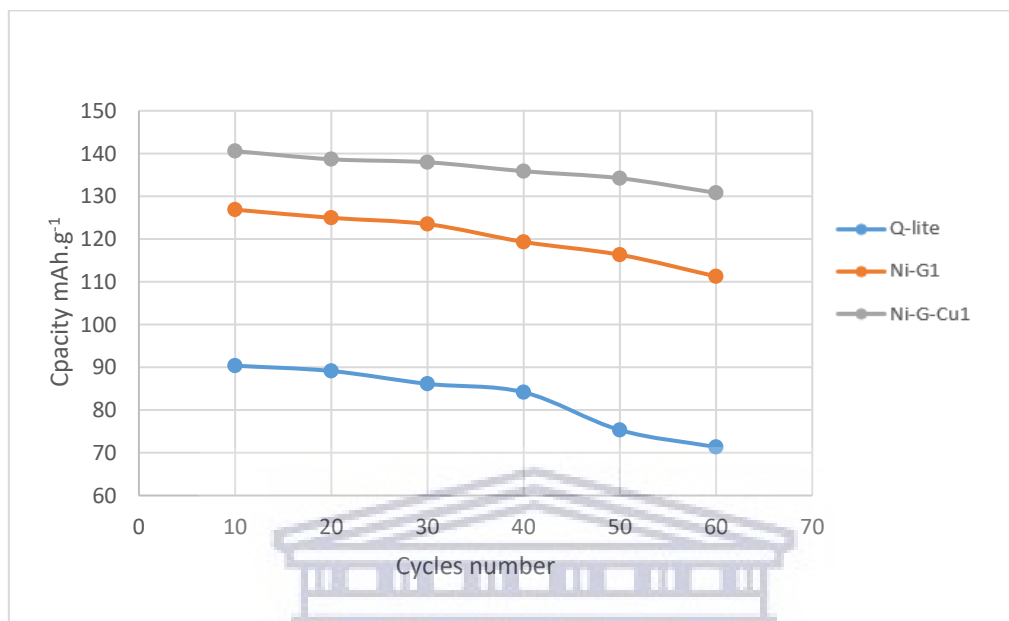


Figure 54: Capacity loss measurements during cycling

It was observed that a significant decrease in capacity of the Q-lite commercial electrode occurs after the 40<sup>th</sup> cycle from 90 to 71 mAh·g<sup>-1</sup>. As depicted in Figure 54, it showed a higher capacity loss in comparison with the Ni-G1 electrode with 119 mAh·g<sup>-1</sup> at the 40<sup>th</sup> cycle and 111 mAh·g<sup>-1</sup> by the 60<sup>th</sup> cycle. While the Ni-G-Cu1 showed a higher specific capacity of the Ni-G1 electrode, it was also found that the copper content has a limited impact on the capacity fade and maintenance of stable electrochemical performance. the capacity losses measurement occurring from 10 to 60 cycles, it was reported that capacity losses are persistent in nickel-based electrode [13].

#### 4.1.1 X-Ray Diffraction results analysis

The objective of performing an XRD analysis on the electrode material is to help us identify the charge and discharge products of nickel electrode, in theory, charge and discharge products can confirm the redox reaction taking place during the cycling.

To determine the crystalline phase and structure the XRD analysis was performed to confirm



the presence of charge and discharge products of the nickel hydroxide electrode in comparison with the precursor material. XRD patterns confirmed important structural differences, the Ni(OH)<sub>2</sub> Bochemie sample shows a net degree of structural order, which is identified by well-defined peaks. As shown on the diffractogram depicted in Figure 55, the Ni(OH)<sub>2</sub> Bochemie sample is made of the  $\beta$ -phase, as the first peak is located at about 23° [112].

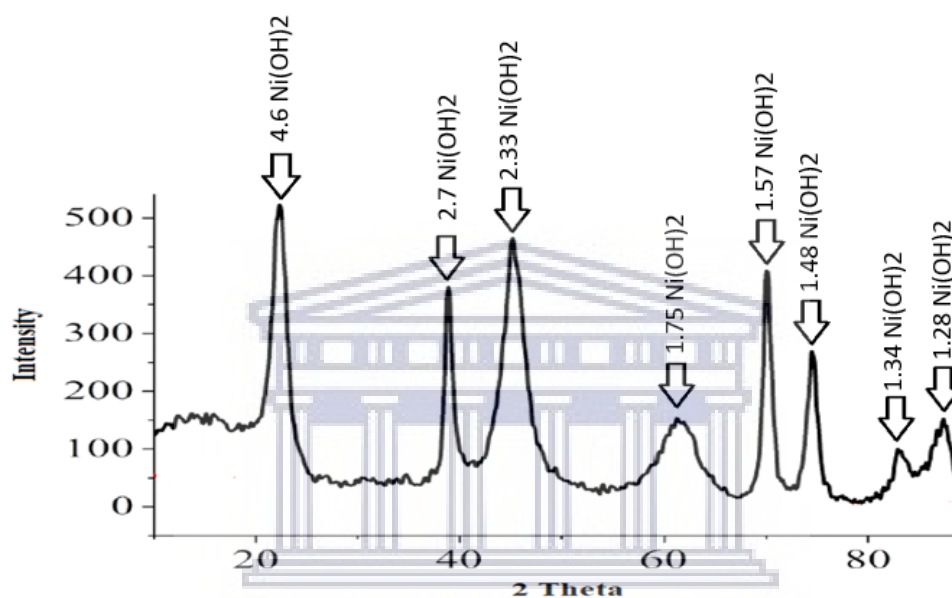


Figure 55: XRD patterns of Ni(OH)<sub>2</sub> powders from Bochemie [112]

The two phases structure of the Ni(OH)<sub>2</sub>, namely,  $\alpha$ -Ni(OH)<sub>2</sub> and  $\beta$ -Ni(OH)<sub>2</sub> crystallise in a hexagonal system, where, the C-axis accommodate the brucite-type layered Ni(OH)<sub>2</sub>. The particular difference between  $\beta$ -Ni(OH)<sub>2</sub> and  $\alpha$ -Ni(OH)<sub>2</sub> nest in layers stacking along the C-axis [113].  $\beta$ -Ni(OH)<sub>2</sub> layers are ideally stacked along the C-axis with an inter-lamellar distance of 4.6 Å, but the inter-lamellar distance of the  $\alpha$ -Ni(OH)<sub>2</sub> layers is about 8 Å [113].



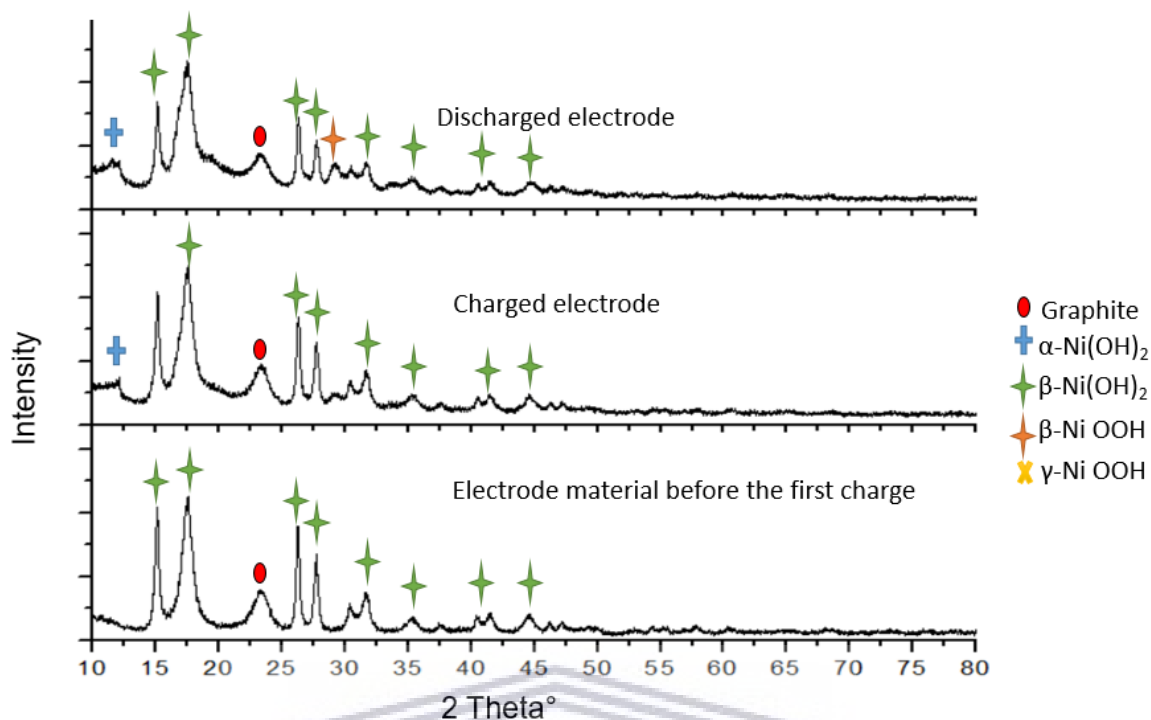


Figure 56: XRD patterns of charged and discharged Ni-G1 electrode in comparison with electrode material before the first charge

Figure 56 shows the 3 XRD patterns, Ni-G1 was investigated to help confirm the presence of charge and discharge products. The base diffractogram, represents the precursor material, where most of the peaks corresponded to the  $\beta$ -Ni(OH)<sub>2</sub>. The identifying peaks were situated respectively at 15° (001), 18° (001), 26°(001), 31°(100), 32°(100), 41°(101), and 45°(102). At 29°, there is a  $\beta$ -NiOOH peak indicating that the electrochemical charge took place [113].

For the charged electrode, the  $\alpha$ -Ni(OH)<sub>2</sub> was identified via a low peak situated at 12°, this may occur via a dehydration reaction according to the bode diagram [81]. In theory, the charging process consists of an oxidation reaction, in which the  $\beta$ -Ni(OH)<sub>2</sub> is transformed into  $\beta$ -NiOOH [113].

Peaks for  $\beta$ -NiOOH and  $\beta$ -Ni(OH)<sub>2</sub> can be identified both on the charged and discharged electrode samples, indicating a low material utilisation [113].

It was reported that various attempts were conducted to investigate and to determine the reaction nature between  $\beta$ -NiOOH and  $\beta$ -Ni(OH)<sub>2</sub>, and based on the X-ray diffraction patterns it was found that the reaction is heterogeneous. Both  $\beta$ -Ni(OH)<sub>2</sub>, and  $\beta$ -NiOOH were present during charge or discharge [114]. Which found to be the opposite according to the XRD results performed on the Ni-G1 sample, after first charge only.

### 4.1.2 Scanning Electrode Microscopy analysis

As shown in Figure 57, the results of SEM have revealed that the Bochemie Ni(OH)<sub>2</sub> powder demonstrates a fragment-like morphology and no distinct shapes can be identified [112].

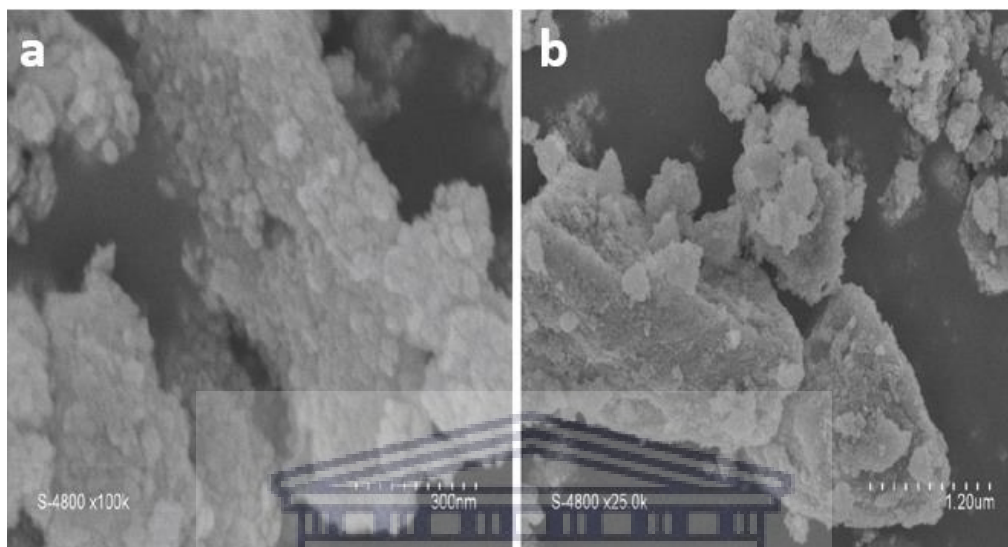


Figure 57: SEM images of Ni(OH)<sub>2</sub> Bochemie Powder (a) 300 nm scale, (b) 1.2 μm scale [112]

The morphology of the particles was investigated before and after galvanostatic cycling using SEM micrographs. SEM micrographs of the charged electrode are illustrated in Figure 58 different magnifications were used to investigate the material, it was found that a granular structure and agglomerates are identified as  $\beta$ -NiOOH [81].

Cracks were identified clearly in micrographs depicted in Figure 58 showing a particle crack which suggests that a swelling mechanism is developed during the charging process, allowing smaller particles to form with cycling [81].

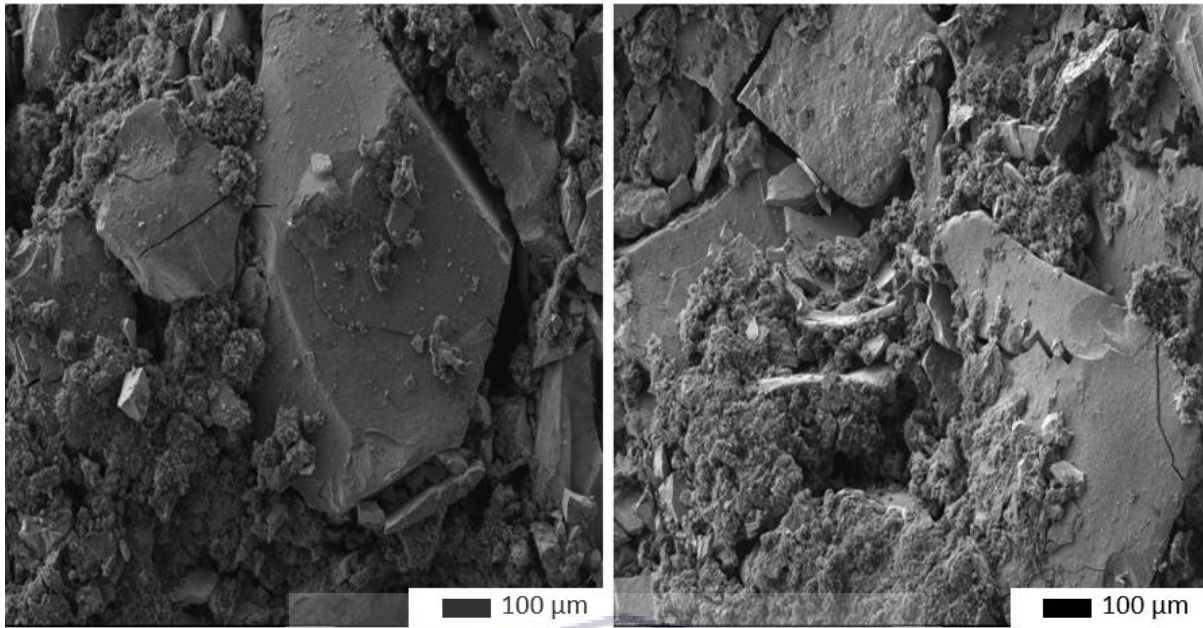


Figure 58: SEM micrographs of the same charged Nickel-based electrode at similar magnification

The growth in particle size is mainly due to lattice extension and intercalation issues between the protons and the Ni ions. Stacking is caused when the normal stacking sequence in the crystal structure is interrupted, Approximately, 15 to 20% of issues preventing the electroactive material from achieving their supposed theoretical energy densities of  $289 \text{ Ah}\cdot\text{kg}^{-1}$  are caused by stacking in the crystal structure [64].

SEM micrographs of the discharged electrode are illustrated in Figure 59, different magnifications were used to investigate the material, and it was found that irregular shard-like particles were observed, with smaller agglomeration surrounding the  $\beta\text{-NiOOH}$  crystal, they were identified as  $\beta\text{-Ni(OH)}_2$  confirming low material utilisation during the discharge, which leads to limited specific capacity [64].

Crystallographic and micro-morphological transformations occurring in the charge and discharge process are the main causes of the capacity loss mechanism of the active material [115].

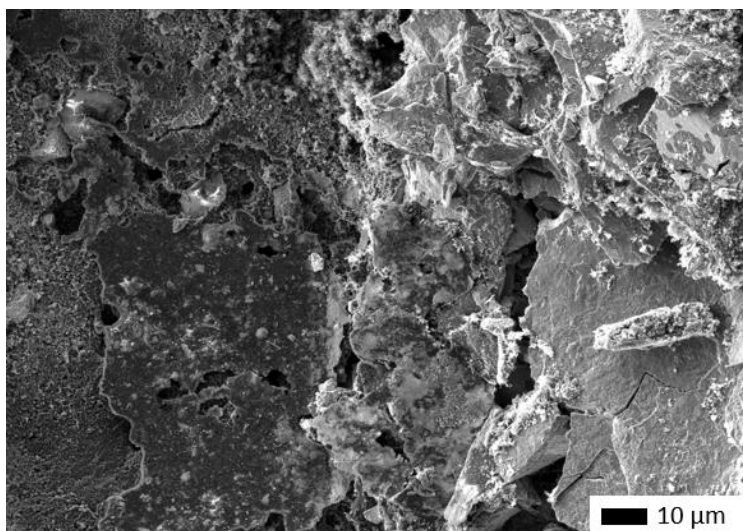


Figure 59: SEM micrographs of a discharged Nickel-based electrode

Despite electrode expansion and active material cracks, it was reported that there is no evidence of important internal resistance caused by this issue. It appears that the conductivity of the nickel composite electrode may not be the controlling factor in electrode failure [115].

### 4.1.3 Electrochemical Characterisation results

#### 4.1.3.1 Cyclic voltammetry Analysis

The electrodes were activated for 50 cycles at a scan rate of  $200 \text{ mV}\cdot\text{s}^{-1}$  vs. the Hg/HgO (Reference electrode) in 6 M KOH/1LiOH electrolyte. The activation step was performed to expel any impurities residing in the electrode surface and to stabilise the electrochemical response of the electrode [100].

Cyclic voltammetry was used to quantify the charge/discharge of electrodes and the reversibility of the electrode reaction. When the difference value between the oxidation and reduction potential ( $E_{\text{O}}-E_{\text{R}}$ ) is small, it signifies that the reaction is highly reversible. Where  $E_{\text{O}}$  represents the oxidation potential and  $E_{\text{R}}$  represents the reduction potential [116].

To quantify the reversibility of the electrode reaction the cyclic voltammograms were analysed to establish the difference value between the oxidation potential ( $E_{\text{O}}$ ) and the reduction

potential ( $E_R$ ) [116].

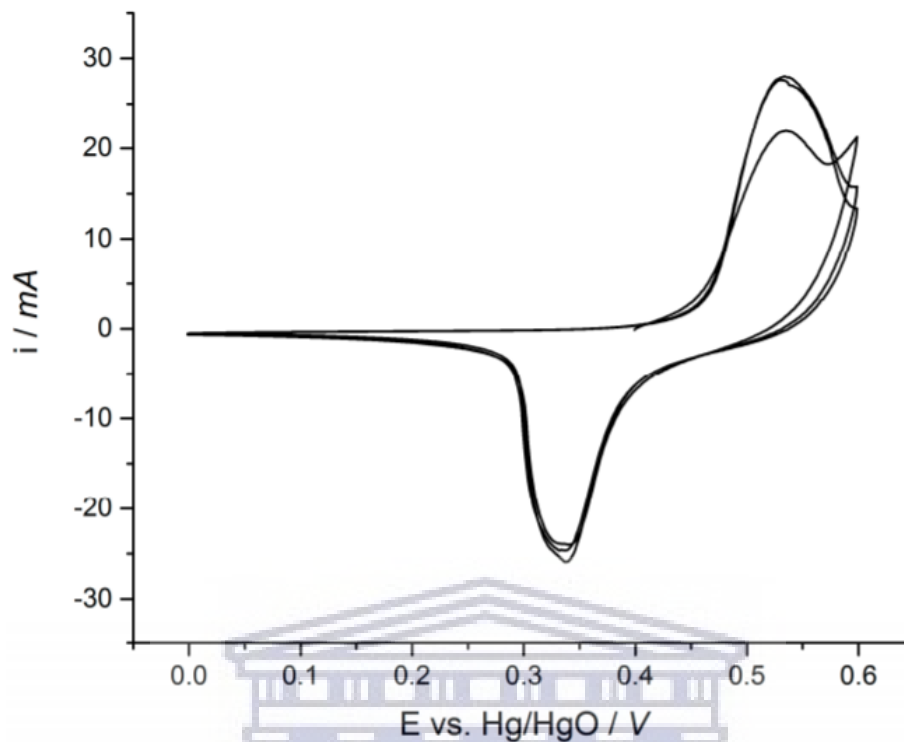


Figure 60: Typical cyclic voltammogram of a Ni(OH)<sub>2</sub> electrode at 4 different scan rates [117]

Figure 60 shows the typical cyclic voltammogram of a Ni(OH)<sub>2</sub> electrode. The sweep of the CV from 0.00 to +0.25 V indicates negligible activity. While sweeping towards more positive potential a current peak takes place at +0.55 V indicating an oxidation of the nickel hydroxide precursor material as the transformation of  $\beta\text{-Ni(OH)}_2$  to  $\beta\text{-NiOOH}$ . Beyond these potential values, oxygen evolution reaction starts [117].

Cycling back towards negative potential, a reduction peak is observed at around +0.32 V, indicating the reversible reaction and the transformation of  $\beta\text{-NiOOH}$  to of  $\beta\text{-Ni(OH)}_2$  [117].

- Oxygen evolution reaction

During the charging process of the nickel hydroxide electrode, the oxygen evolution reaction (OER) may take place, under certain conditions.

The required potential to split water must be higher than its thermodynamic value of 1.23 V (vs RHE) Due to the high overpotential of the oxygen evolution reaction (OER). It is considered as a side reaction, and one of the major issues of the Ni-based battery today [118].



Oxygen gas bubbles trapped within the Nickel oxyhydroxide lattice may cause electrode degradation by causing internal expansion stresses on the porous nickel pasted electrode subsequently affecting the electrochemical performance of the battery [119].

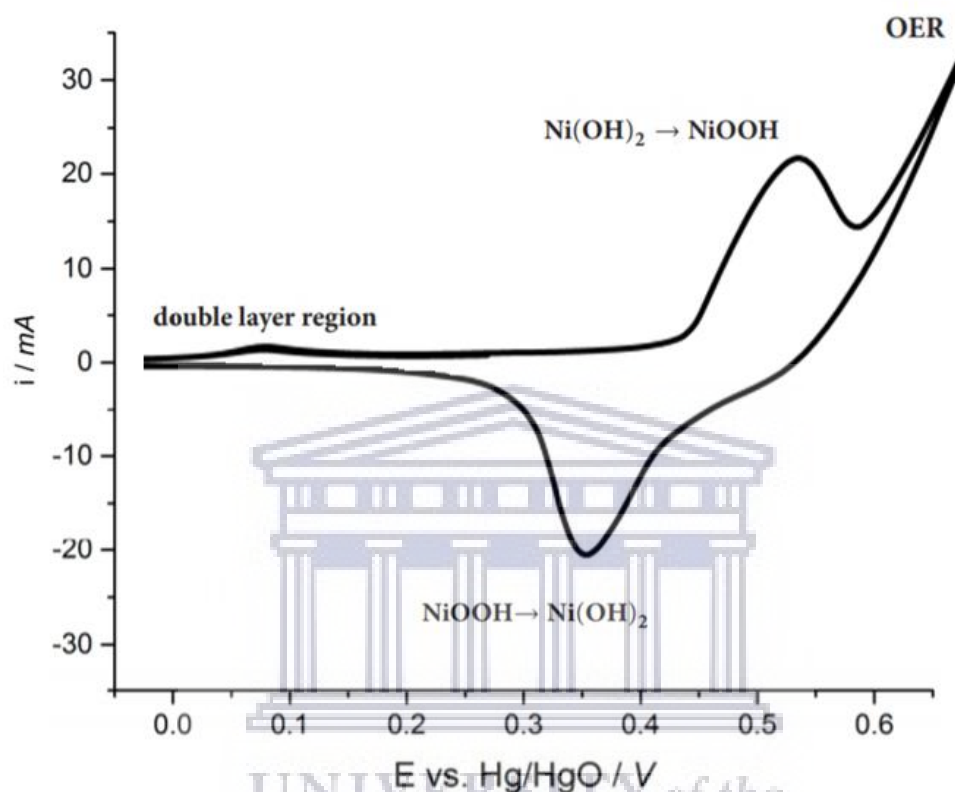


Figure 61 : Cyclic voltammogram of Ni-G1 electrode

Figure 61, shows a cyclic voltammogram of a Ni-G1 electrode. The sweep of the CV from 0.00 to +0.25 V indicates negligible activity with a minor oxidation observed at +0.8 V, maybe be caused by impurities from the industrial-grade material. While sweeping towards more positive potential an current peak takes place at +0.54 V indicating an oxidation of the nickel hydroxide precursor material as the transformation of  $\beta\text{-Ni(OH)}_2$  to  $\beta\text{-NiOOH}$ . Towards more positive potential the current values rises suggesting the beginning of oxygen evolution reaction [117]. Cycling back towards negative potential, a reduction peak is observed at around +0.35 V, indicating the reversible reaction and the transformation of  $\beta\text{-NiOOH}$  to  $\beta\text{-Ni(OH)}_2$ .

In the cyclic voltammogram of the Ni-G1, which was made from the same spherical  $\text{Ni(OH)}_2$ , it can be seen that the oxidation current peak of the active material is well separated from the oxygen evolution current peak [120].

The charge-discharge process of  $\text{Ni(OH)}_2/\text{NiOOH}$  is better understood as a proton intercalation/de-intercalation solid-state reaction in which the exchange of both protons and electrons are controlled by the bulk solid diffusion of protons [121] [122]. In a battery, the electrochemical reaction of  $\text{Ni(OH)}_2$  progresses mainly between  $\beta\text{-Ni(OH)}_2$  and  $\beta\text{-NiOOH}$ . In order to improve the electrochemical behaviour and increase the specific discharge capacity of the  $\text{Ni(OH)}_2$  electrode, additives such as metal cations are currently being added to  $\text{Ni(OH)}_2$ . The formation of  $\gamma\text{-NiOOH}$  can be suppressed effectively by adding a known percentage of copper additive to  $\beta\text{-Ni(OH)}_2$  [123].

#### 4.1.3.2 Charge/Discharged Galvanostatic Analysis

Electrochemical characterisation technique such as galvanostatic cycling was used to investigate the mechanism of a redox process.

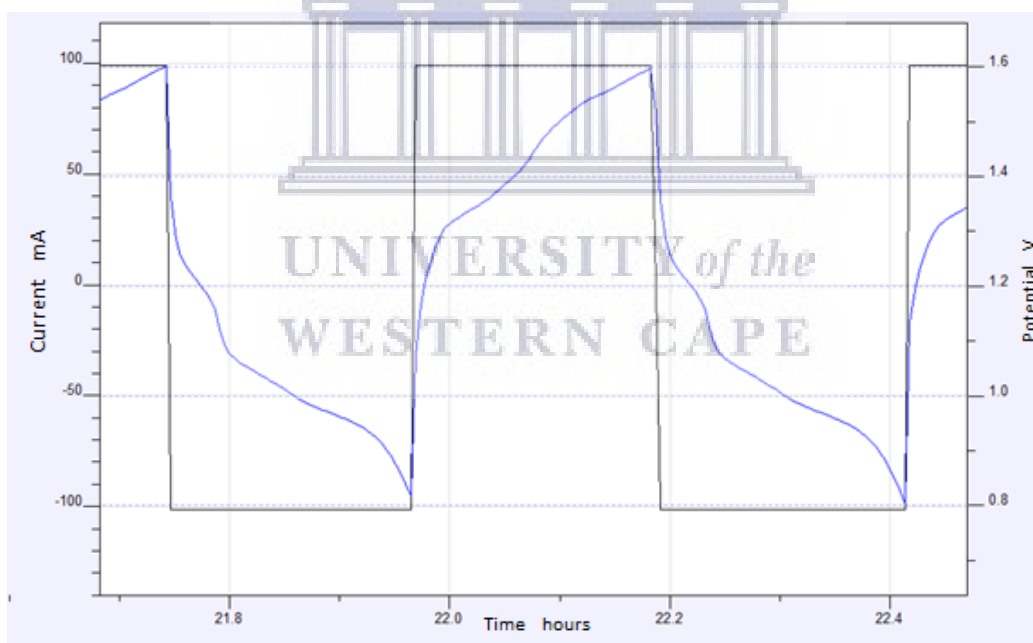


Figure 62: Activation cycling of Ni-G-Cu1 electrode at 100 mA between 1.6 and 0.8 V

The activation phase starts with galvanostatic cycling under a low current 10 mA between 0.8 and 1.6 V. As illustrated in Figure 62 the first discharge time lasted for 0.2 hours but the next discharge curve demonstrated a capacity loss, where similarly the discharge time lasted for approximately 0.2 hours. The noted capacity for the first and the second cycle is 20 mAh.



The activation step is very important in the optimum performance of the Ni-Fe battery. For battery systems like Nickel-Iron battery, an S-shape response is expected [14].

The constant current excitation signal and voltage response are shown in Figure 63 as a function of time after twenty cycles under constant current of 500 mA, the charging and the discharging potential are respectively 1.6 and 0.8 V.

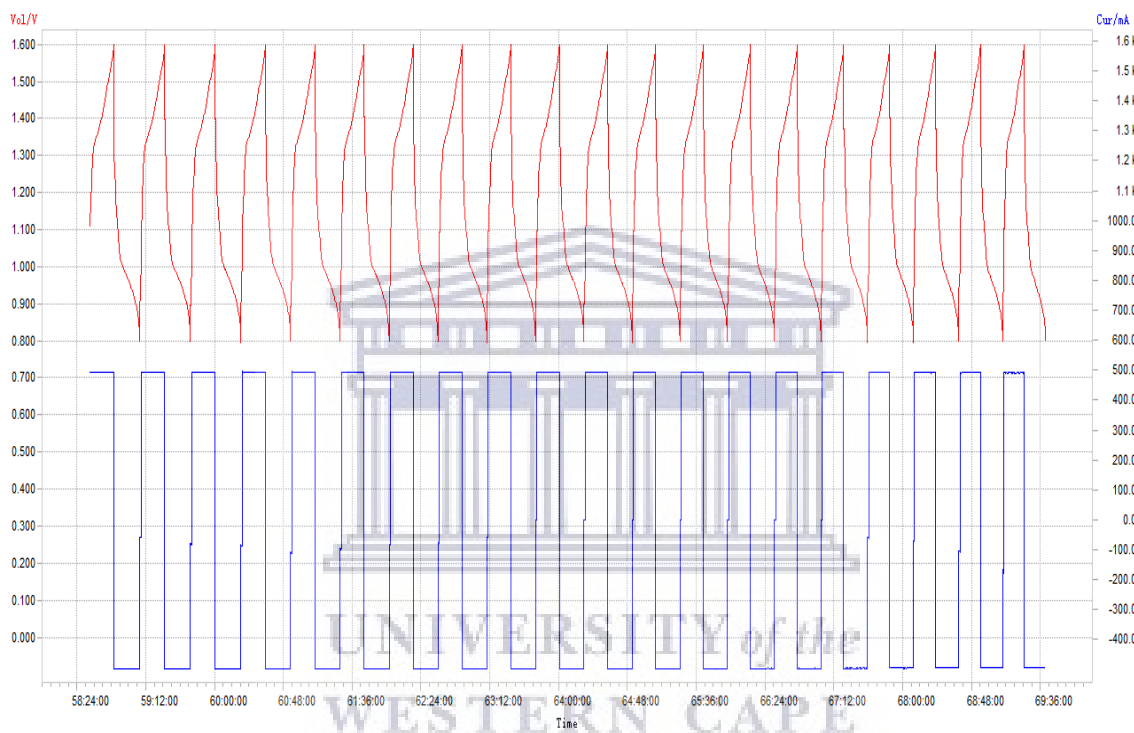


Figure 63: Galvanogram of the Nickel-Iron cell during 20 cycles at 500 mA

The typical 2 steps discharge curve of a Nickel-Iron cell is depicted in Figure 64, where the lower cut-off voltage is set to 0.8 V [124].

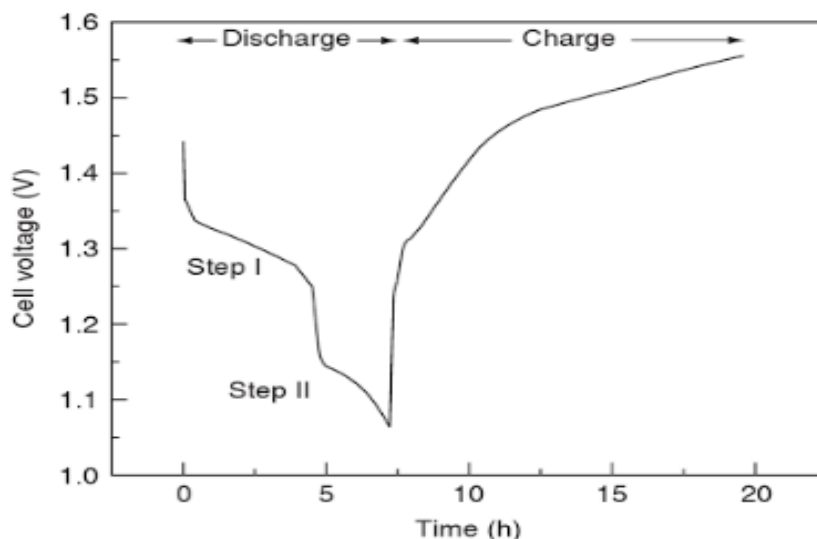


Figure 64 : Typical two step discharge of the Nickel-Iron cell[124]

The potential of the electrode changes from open-circuit potential to an approximately constant value, until the concentration of the redox species at the electrode is depleted. When these species are depleted at the electrode surface, the potential rapidly shifts to a potential ability to sustain the applied current. This abrupt shift is identified as the transition time. When one redox species is present, the potential shifts to a value that causes either the supporting electrolyte or the solvent to be reduced/oxidised [124]. Figure 65 shows a screen shot of the 100<sup>th</sup> charge-discharge curve of the Ni-G-Cu electrode. Two-step discharge can be identified in all the graphs indicating a good reversibility performance of the active material in line with findings in literature [124].

The active material prepared from Bochimie nickel hydroxide with copper additive showed a superior specific capacity and a lower capacity reduction upon cycling [93]. Claims that the resistance of active mass change during the discharge process engendering higher cathodic values at constant current.

A1, A2, A3, and A4 are electrode samples produced with the same composite electrode material, to study the swelling phenomena in a free-standing electrode where the nickel electrode is subjected to cycling for over that 60 times at a constant current of 200 mA. The dimensions of the electrodes before and after cycling are shown in Table 12.

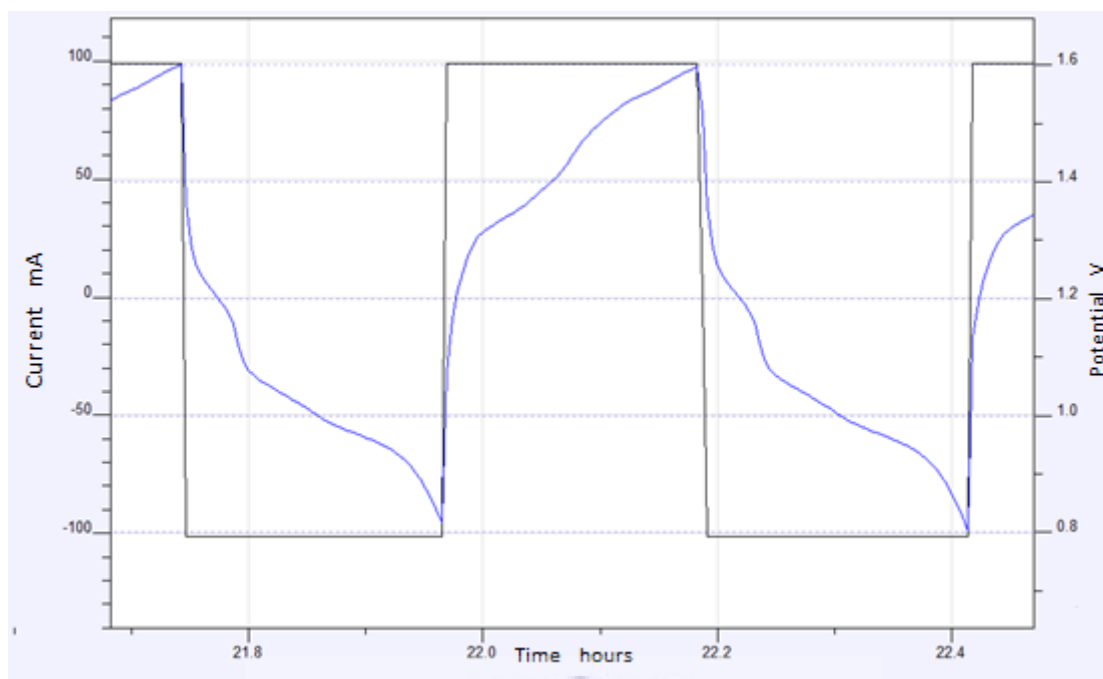


Figure 65: Galvanostatic cycling of Ni-G-Cu1 electrode at 100 mA between 1.6 and 0.8 V

Table 12: Swelling Measurement of various composite electrodes

Name of the electrode	Thickness before cycling (mm)	Thickness after cycling (mm)	Electrode expansion (%)
A1	1.67	1.82	109
A2	1.73	1.81	105
A3	1.68	1.79	107
A4	1.70	1.96	115

The average expansion was 109 %, indicating that in a free-standing position, where the electrode is tested and cycled out of the bipolar battery, the Ni-G1-Cu1 electrode shows a consistent swelling.

As shown in Figure 66, the surface of a fresh nickel-based electrode exhibits a regular structure, with visible cracks or layer morphology. Figure 67 illustrates the nickel-based electrode cycled at a potential ranging from 0.8 to 1.6 V, manifested two distinct regions of the electrode respectively, Region 1: shows an upper fragment of the electrode material surface separated from the basic structure of the electrode. Region 2: Shows the exposed inner material of the

electrode due to a possible material loss occurring during the cycling process.

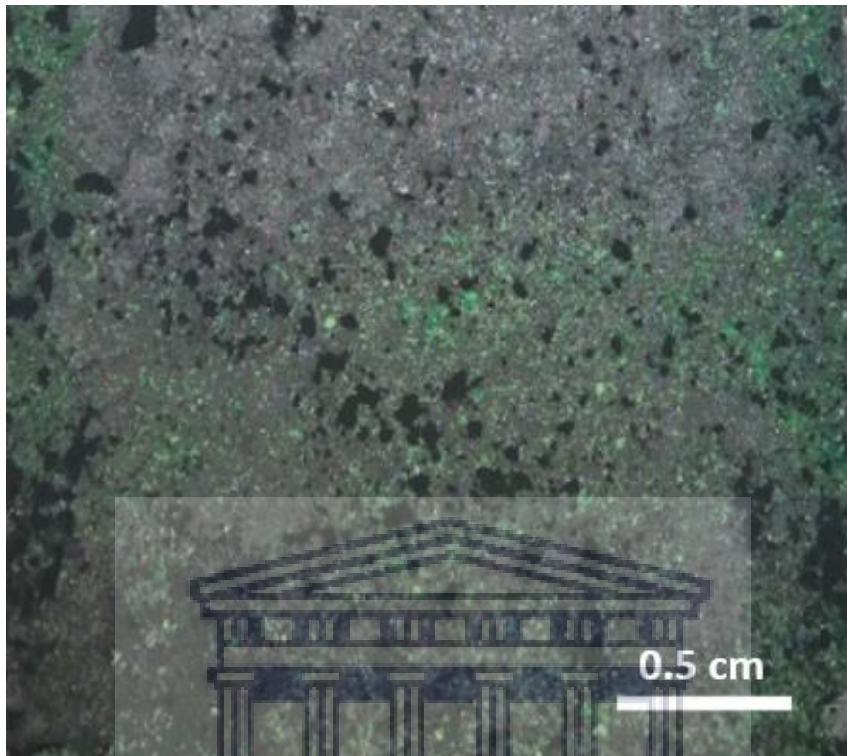


Figure 66 : Surface of a fresh Nickel-based electrode

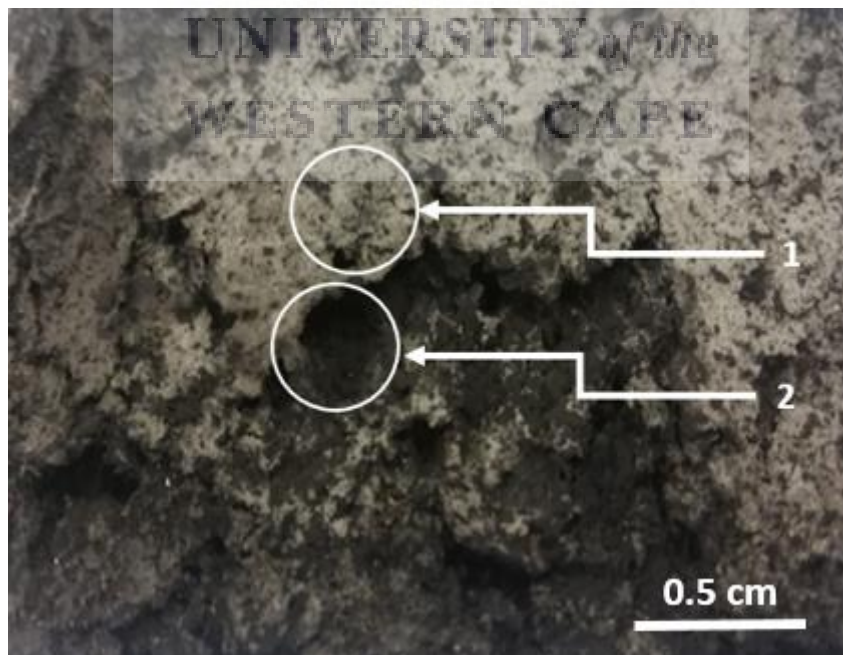


Figure 67 : Photo of the Nickel-based electrode after cycling

## 4.2 The development of the bipolar electrode and its fabrication process

The first experimental trials were conducted in A6 DIN bipolar plate format where a commercial nickel electrode (Q-lite, China) was cut and hot-pressed onto the bipolar plate according to the design dimensions as shown in Table 13. Hot-pressing parameters were optimised, namely the influence of hydraulic pressure, the pressing temperature and the pressing time. The quality of the electrode was determined based on three parameters; (1) through plane conductivity, (2) the mechanical integrity of the bipolar plate, and (3) the powder adhesion to the bipolar plate.

### 4.2.1 Pre-treatment results of the bipolar plates

Plasma etching or activation was also investigated to prepare the electrode surface for bonding, where the surface of the bipolar plate was treated using a plasma pistol.

This experiment led to a slight overall change in the roughness parameters of the bipolar plate, confirmed through the confocal laser scanning microscopy test results as shown in Figure 68 , Figure 69 .

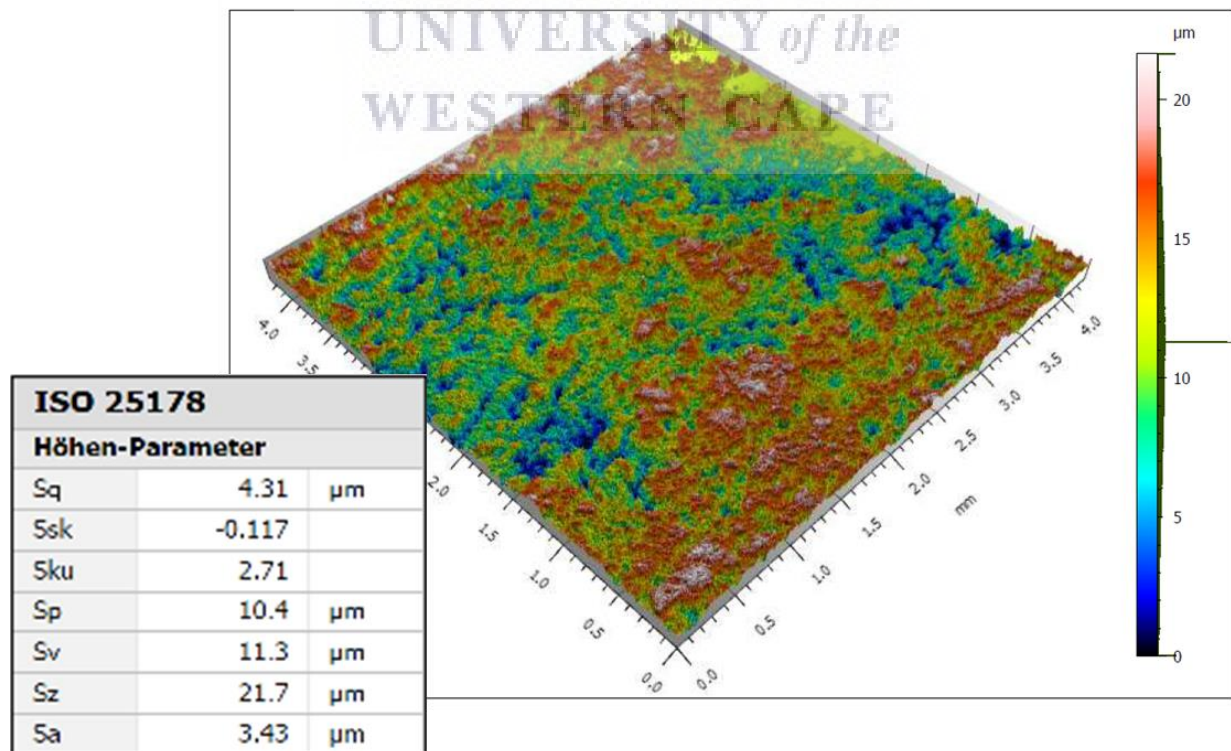




Figure 68: CLSM results of a non-treated bipolar plate

The “Sq” value represents the root mean square value of ordinate values within the definition area. It is equivalent to the standard deviation of heights. The Sq value of the original non-treated sample was  $4.31\mu\text{m}$ , while the treated bipolar plate showed an increase of  $1.15\mu\text{m}$  when compared to the non-treated sample. This result shows that the plasma treatment of the bipolar plate managed to increase this roughness parameter. Ssk which is the Skewness parameter, both samples showed a negative Ssk value. When the Ssk value is  $< 0$ , this means that the height distribution is skewed above the mean plane. The difference between the two samples with regard to this parameter is of 0.02. Sa which is the arithmetical mean height is higher in the etched sample indicating that the later has a rougher surface area than the non-treated plate, with a difference of  $0.93\mu\text{m}$ .

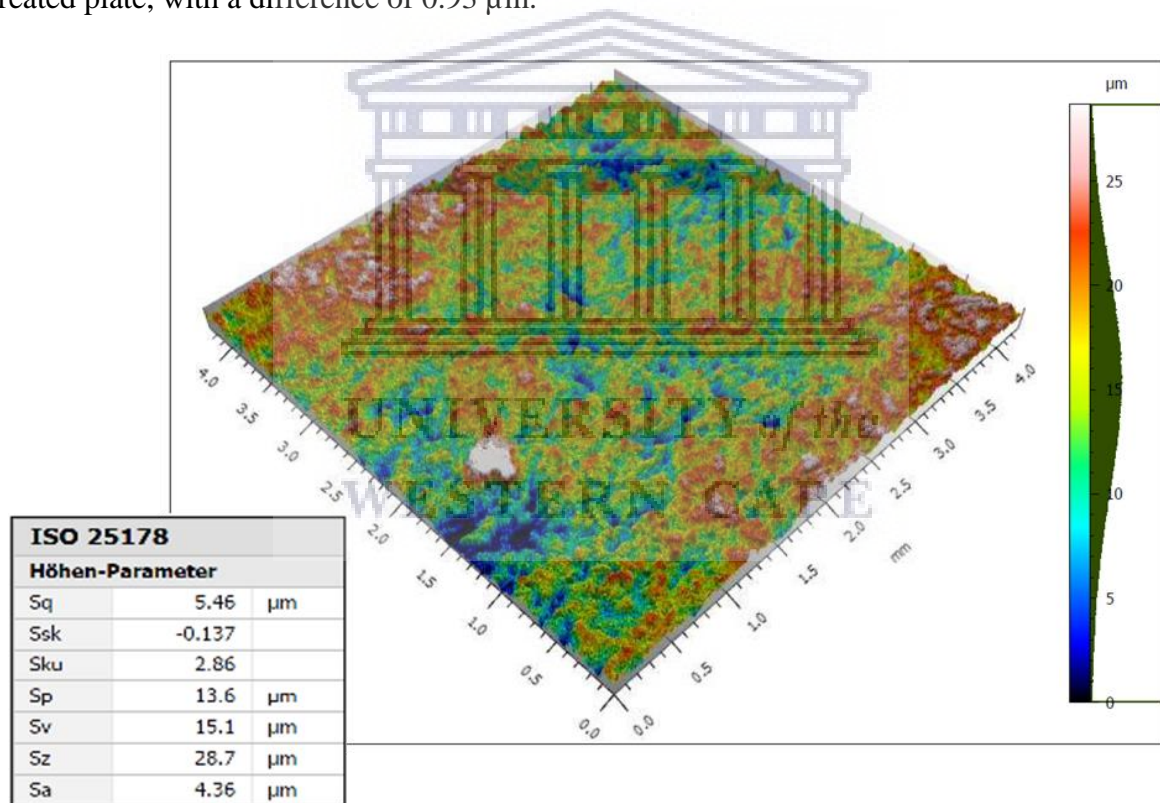


Figure 69: CLSM results of a plasma-treated bipolar plate

All bipolar plates are treated with 3200-grade micro-mesh sandpaper before loading the active material to enhance the overall adhesion.

## 4.2.2 Mould optimisation results

Electrode reproducibility was verified using digital callipers to measure the total thickness of the electrode after the hot-pressing process. Two batches of electrodes were produced during the experimental trials. BiNiFe 01 batch was produced using manual loaded stainless steel frames. The electrode thickness for each electrode is provided in Figure 70. The average thickness of the electrodes was found to be 0.3 mm above the target value of 3.5mm. More concerning was the relatively large spread between the thickness of the various electrodes (between 3.55 and 4.23mm)

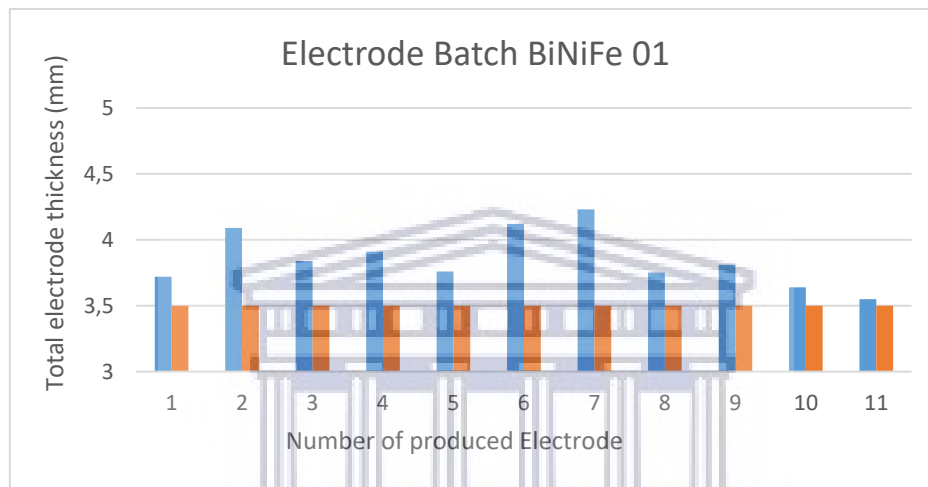


Figure 70: Overall electrode thickness compared to the design requirements for batch 01 in which a SS frame was used

BiNiFe 02 batch was produced using silicon frames yielding a significantly improved consistency in the thickness of the produced electrodes as depicted in Figure 71.

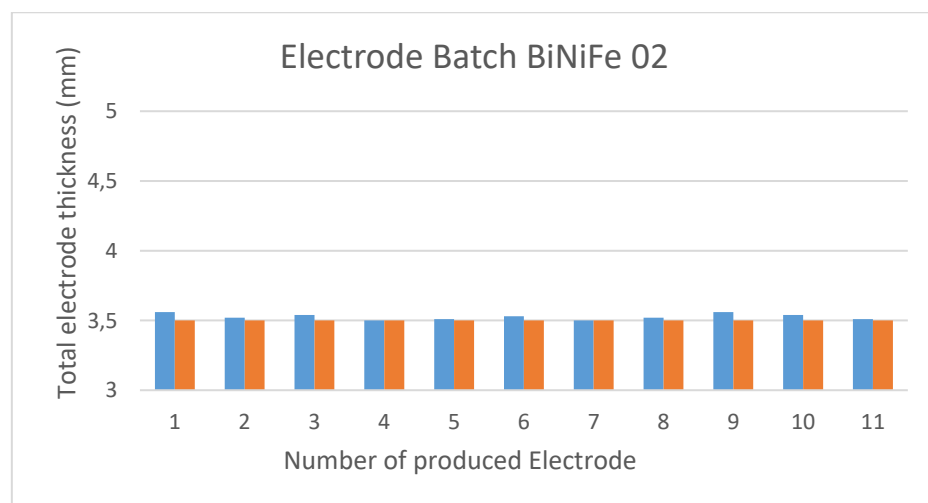




Figure 71: Overall electrode thickness compared to the design requirements for batch 02 in which a silicon frame was used,

The average thickness of the 11 electrodes in batch 02 was only 0.02mm above target value with a spread between 3.5 and 3.54mm. The improvement could largely be prescribed to the improved heat management when the thermally insulating silicon mould was used and the better compressibility of silicon compared to the SS, allowing for a better distribution of the powder when subjected to pressure. The improved dimensional reproducibility of the electrodes marked an important achievement, essential in the development towards the bipolar battery.

### 4.2.3 Hot-pressing optimisation results

Table 13: Initial electrode processing parameters and their impact on electrode properties

<b>Electrode processing parameters</b>				
Sample name	A1	A2	A3	A4
Mould version used	V1	V1	V1	V1
Cathode type	Q-lite	Q-lite	Q-lite	Q-lite
Pressing time (min)	5	5	5	5
Pressing temperature (°C)	110	110	110	110
Bipolar plate thickness (mm)	0.5	0.5	0.5	0.5
Hydraulic Pressure (MPa)	50	25	40	60
<b>Electrode properties and features</b>				
Adhesion to the BP	Poor adhesion	Reasonable adhesion	Poor adhesion	Poor adhesion
Mechanical integrity	Severe deformation and cracks	Mild deformation, no visible cracks	Severe deformation and cracks	Severe deformation and cracks
Conductivity (S·cm <sup>-1</sup> )	0.12	0.25	0.1	0.2
Sample A1	Sample A2	Sample A3	Sample A4	

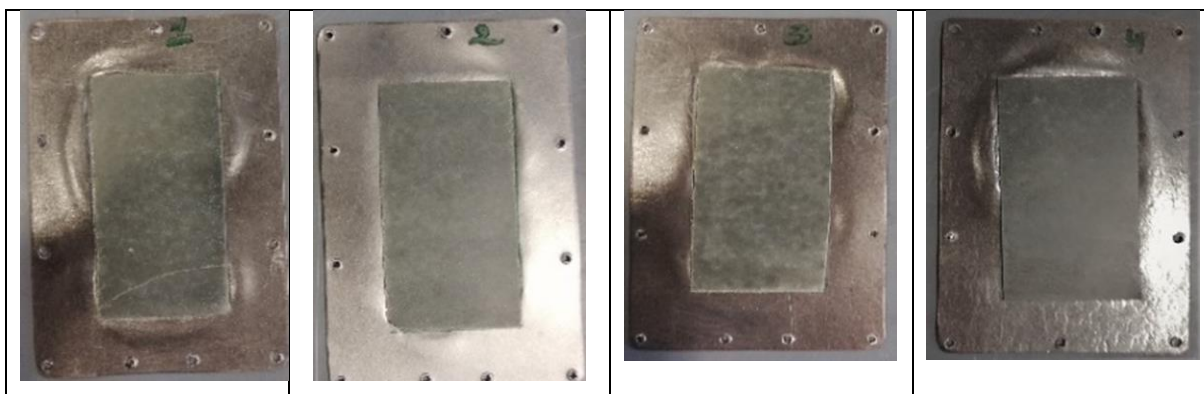


Table 13 indicates that the only set of process parameters yielding an electrode with acceptable properties is the combination used for the production (A2). Correct pressing conditions are essential to prohibiting thermal retraction after the hot-pressing step.

Further electrode production optimisation was performed to develop in-house made electrodes with adequate conductivity and stable mechanical properties. The results in

Table 14 shows the impact of pressing temperature while

Table 15 shows the impact on pressing duration.

Table 14: Variation of pressing temperature and its impact on electrode properties

<b>Electrode processing parameters</b>				
Sample name	B1	B2	B3	B4
Mould version used	V2	V2	V2	V2
Cathode type Ni(OH) <sub>2</sub>	In-House Composite	In-House Composite	In-House Composite	In-House Composite
Pressing time (min)	5	5	5	5
Pressing temperature (°C)	125	120	115	110
Bipolar plate thickness (mm)	0.5	0.5	0.5	0.5
Hydraulic Pressure (MPa)	25	25	25	25
<b>Electrode properties and features</b>				
Adhesion to the BP	Reasonable adhesion	Reasonable adhesion	Reasonable adhesion	Reasonable adhesion
Mechanical integrity	Mild deformation no visible cracks	Mild deformation no visible cracks	No deformation no visible cracks	No deformation no visible cracks

Conductivity ( $S \cdot cm^{-1}$ )	1.62	1.84	3.7	6.8
Electric resistivity: ( $\Omega \cdot cm$ )	0.617	0.543	0.27	0.147

The batch of electrodes including B1 B2, and B3 and B4 was produced with constant operating parameters apart from varying only the pressing temperature. The temperature range was kept below the melting point of the binder, in an effort to keep the mechanical integrity of the produced electrodes and to ensure all the functional capacity of the binder, stabilising the loading of the active material.

It was found that high temperatures have a major impact on the overall resistivity of the electrode, as shown in

Table 14, increasing the pressing temperature led to a higher resistivity value, this could be explained by the fact that the polymeric nature of the binder influences the electrical conductivity of the electrode. It appears that the electrical conductivity is reduced with increasing hot-press temperature. Consequently, B4 sample was selected to proceed to further optimisation steps.

The batch of electrodes including C1 C2, and C3 and C4 was produced with constant operating parameters apart from varying only the pressing time. The maximum duration was set at 10 min, exceeding this time range, the bipolar plate showed sever and irreversible damage to its structure with visible deformation.

Table 15 : Variation of pressing time and its impact on electrode properties

<b>Electrode processing parameters</b>				
Sample name	C1	C2	C3	C4
Mould version used	V2	V2	V2	V2
Cathode type Ni(OH) <sub>2</sub>	In-House Composite	In-House Composite	In-House Composite	In-House Composite
Pressing time (min)	10	7	5	2
Pressing temperature (°C)	110	110	110	110
Bipolar plate thickness (mm)	0.5	0.5	0.5	0.5
Hydraulic Pressure (MPa)	25	25	25	25
<b>Electrode properties and features</b>				
Adhesion to the BP	Reasonable	Reasonable	Reasonable	Reasonable

	adhesion	adhesion	adhesion	adhesion
Mechanical integrity	No deformation no visible cracks	No deformation no visible cracks	No deformation no visible cracks	No deformation no visible cracks
Conductivity ( $S \cdot cm^{-1}$ )	2.7	3.2	6.8	1.7
Electric resistivity: ( $\Omega \cdot cm$ )	0.37	0.312	0.147	0.588

As shown in

Table 15 it was found that 5 min of pressing time exhibited the optimum results, as indicated by the conductivity measurement. The min time of 2 min was not sufficient to melt the binder and link all the mixture ingredients.

The third process variable involved in the hot –press procedure is the exerted pressure. Table 16 shows the electrode properties as function of the hydraulic pressure applied.

Table 16: Variation of hydraulic pressure and its impact on electrode properties

<b>Electrode processing parameters</b>				
Sample name	D1	D2	D3	D4
Mould version used	V2	V2	V2	V2
Cathode type	In-House Composite	In-House Composite	In-House Composite	In-House Composite
Pressing time (min)	5	5	5	5
Pressing temperature ( $^{\circ}C$ )	110	110	110	110
Bipolar plate thickness (mm)	0.5	0.5	0.5	0.5
Hydraulic Pressure (MPa)	25	24	22	20
<b>Electrode properties and features</b>				
Adhesion to the BP	Reasonable adhesion	Reasonable adhesion	Reasonable adhesion	Reasonable adhesion
Mechanical integrity	Mild deformation no visible cracks	Mild deformation no visible cracks	No deformation no visible cracks	No deformation no visible cracks
Conductivity ( $S \cdot cm^{-1}$ )	6.8	1.28	1.37	1.48

Electric resistivity: ( $\Omega$ .cm)	0.147	0.781	0.729	0.675
---------------------------------------	-------	-------	-------	-------

As shown in Table 16 the batch of electrodes including D1, D2, and D3 and D4 was produced at constant operating parameters while varying only the hydraulic pressure. The hydraulic pressure range was kept below the point of irreversible deformation of the bipolar plate. It was found that decreasing the pressure has an impact on the overall resistivity of the electrode, as shown in decreasing the applied pressure led to a higher resistivity value, this is explained by the fact that higher pressure value keeps the particles in a compact form facilitating the electrical conductivity.

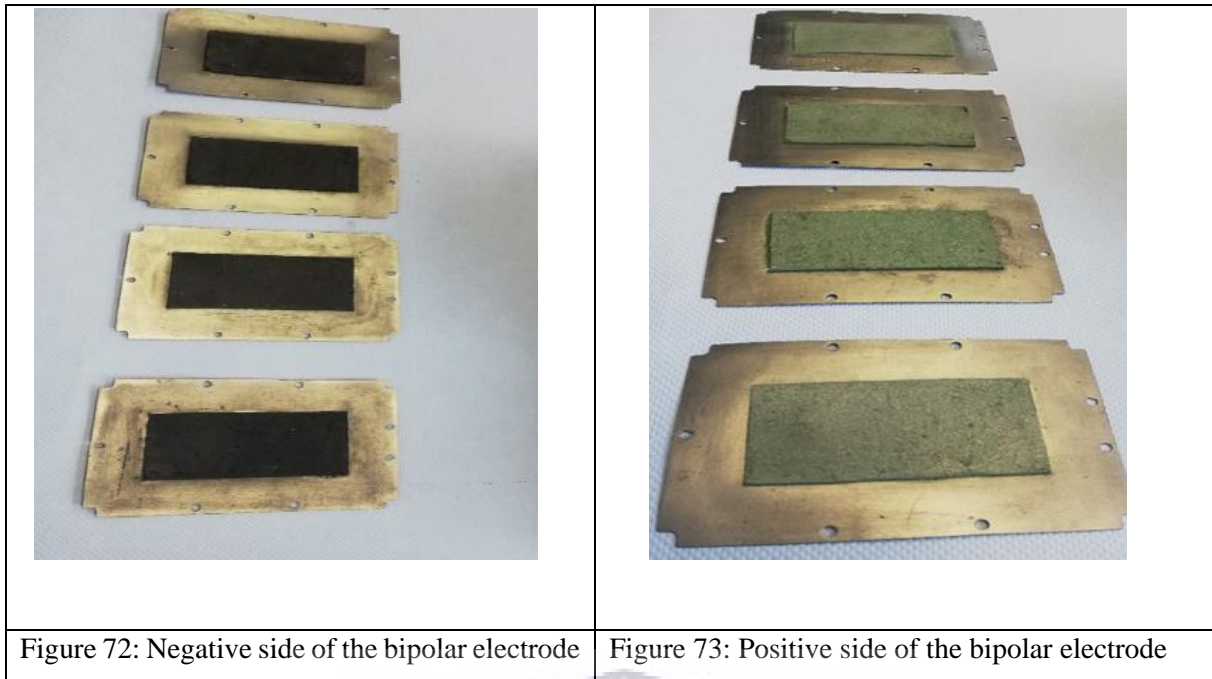
Table 17 shows the optimised value concluded from the experimental trials towards achieving mechanical stable and electroactive bipolar electrode.

Table 17 : Optimised pressing parameters

Parameters	Pressure (MPa)	Temperature ( $^{\circ}$ C)	Time Min
Value	25	110	5

It is worth noting that the iron electrode were pressed onto the bipolar plate before the Nickel-base electrode, it was found that during the experimental trials that the iron based electrode shows a significant retraction at the bipolar plate surface .

Figure 72 and Figure 73 show the final results of the produced electrodes, where both of the anode and the cathode exhibit a reasonable adhesion to the bipolar plate, with no visible cracks on the substrate.



### 4.3 The stack assembly and testing

During the assembly of each layer, the edges of the bipolar electrodes were laser welded together with plastic frames using the equipment described in section 2.x. The frames were machined from PP sheet and equipped with a highly porous separator obtained from Freudenberg, a German-based company specialised in separator materials. The space between two consecutive electrodes forms an electrolyte chamber ensuring ionic conductivity throughout the stack.

The final step of the bipolar Nickel-Iron battery assembly consists of fixing the nickel-coated copper endplates. The experimental procedure is detailed in Appendix C.

#### Battery prototype assembly steps

The production of the bipolar battery prototype was performed following three steps as illustrated in Figure 74.



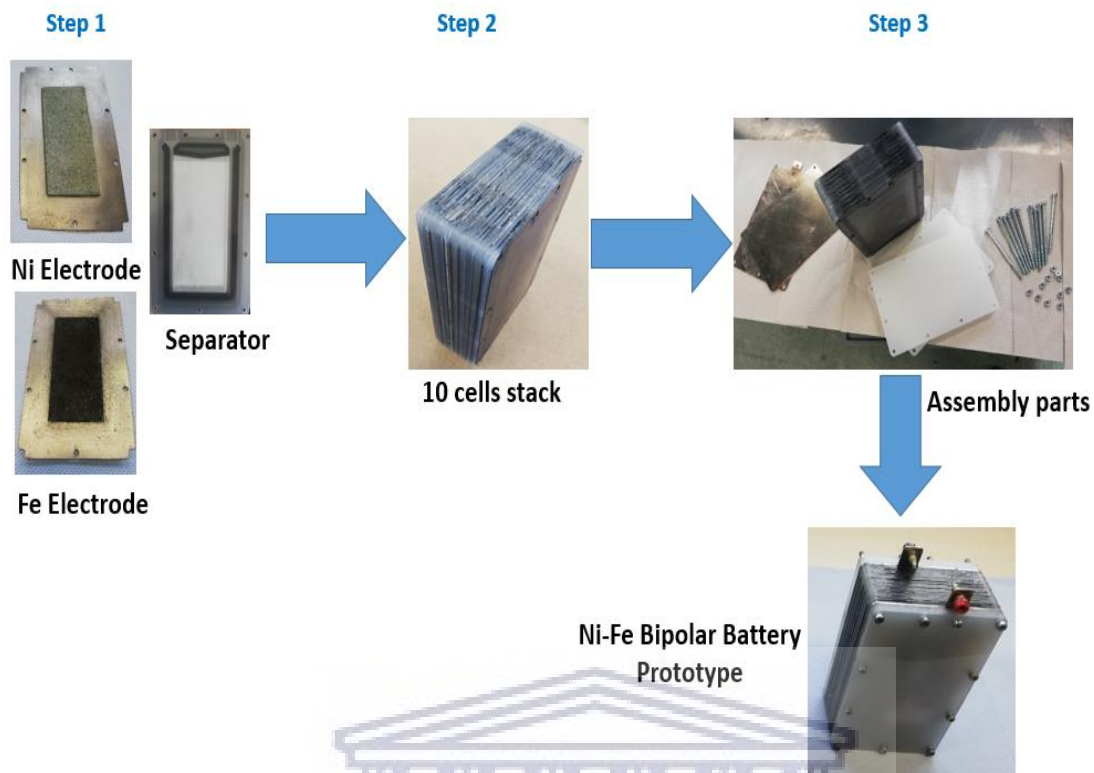


Figure 74: Assembly diagram for the bipolar Ni-Fe battery

- Step 1: A sufficient number of identical bipolar electrodes are produced using the optimised hot-press technique. In addition, a one-sided cathode and a one-sided anode are produced each on one bipolar plate. The polypropylene frames are cut using a CNC machine
- Step 2: A separator is placed into the PP frames which is subsequently laser-welded onto a bipolar electrode. Once a hermetic seal is formed, the next separator and PP frame are introduced and welded onto the first electrode till all bipolar plates are sealed into one stack of cells.
- Step 3: Finalising the assembly of all battery parts, including the screws, the endplates (Current collector), and the outer PP cover. A detailed description of the electroplating process is depicted in Appendix C.

The bipolar battery prototype was assembled with three different specifications, where the prototype consisted of one single cell with a nominal voltage of 1.2 V, the second prototype consisted of two cells with a nominal voltage of 2.4 V and the third prototype consisted of ten

cells providing 12 V. Prototype specifications are listed in Table 18

Table 18: Electrode specifications

	Single-cell DIN A6	Double cell DIN A6	Ten Stack DIN A6
Stack design parameters			
Achieved Capacity (mAh.g <sup>-1</sup> of FeCu)	350	350	350
Total capacity per 7g FeCu electrode (mAh)	2450	2450	2450
Achieved Capacity (mAh.g <sup>-1</sup> of Ni-G1-Cu1)	140	140	140
Total capacity per 15.7g Ni(OH) <sub>2</sub> electrode (mAh)	2200	2200	2200
Stack design potential (V)	1.2	2.4	12
Stack design capacity (Wh)	2.64	5.28	26.4
Stack performance parameters			
Measured stack potential (V)	1.2	2.4	6
Measured capacity (mAh)	1046	1178	NA*
Measured stack capacity (Wh)	1.255	2.827	NA*

\* Integral structure of the stack was compromised

Figure 75 shows an image of the 3 NiFe battery prototypes that were assembled with electrodes produced as described earlier. All cells were laser welded yielding leak free prototypes;

- Prototype 1 consisting of an Fe-based anode- and a Ni-G-Cu-based cathode
- Prototype 2, consisting of 1 fully bipolar electrode sandwiched between and an Fe-based anode- and a Ni-G-Cu-based cathode
- Prototype 3, consisting of 9 fully bipolar electrode sandwiched between and an Fe-based anode- and a Ni-G-Cu-based cathode.

The bolts and nuts, visible in Figure 75 are required to maintain the electrical contact between the end plates and the bipolar electrodes.



Prototype 1

Prototype 2

Prototype 3

Figure 75: Upscale of Ni-Fe Battery prototypes

Table 18 shows the various battery and electrode specifications. It is clear that the design potential (V) for prototype 1 and 2 was reached but at only 50% of the designed capacity. High internal resistance, inaccessibility of the electrolyte, trapping of gasses could have prohibited the battery from reaching the designed capacity and further research is required to improve the battery stack further. Prototype 3 did not reach the design potential. A crack in the bipolar plate would result in a loss of potential. It is expected that some of the bipolar cells were compromised due to excessive force in tightening the screws. This can be prevented by measuring the tightness, that can be determined dynamically, when the screw is tightened, or statically, after the screw has been tightened, by measuring the torque with a torque wrench.

Figure 76 illustrates 10 cycles of charge and discharge performance at constant current of 350 mA for prototype 1. The galvanostatic cycling of the prototype shows a discharge time of 3.0 hours, delivering a total capacity of 1046 mAh.

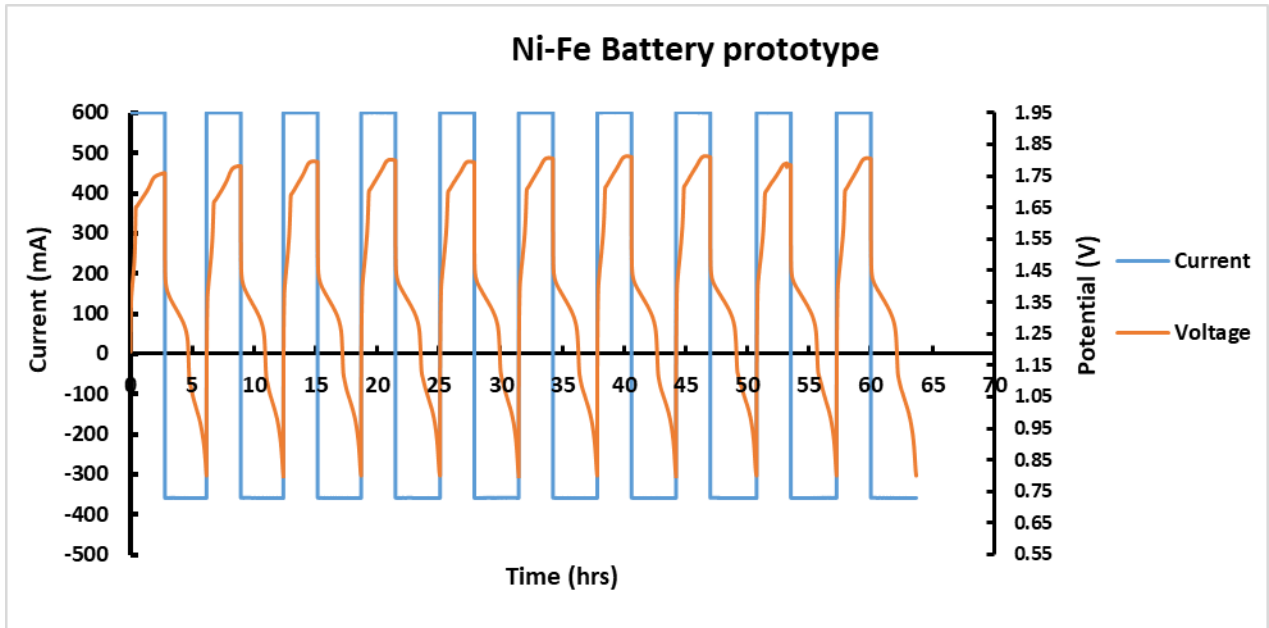


Figure 76: Galvanostatic cycling of the bipolar Ni-Fe battery prototype

- **Prototype 1 Post-mortem analysis**

To investigate the issues faced when testing the battery prototype, a post-mortem analysis was conducted to understand in depth the operating performance of the prototype and evaluate the probable causes for the low electrochemical performance in some cases.



Figure 77: Post-mortem photo of bipolar prototype Components

- Battery current collectors:

Nickel-plated copper endplates were used as a current collector. The manufacturing process is described in Appendix C. The post mortem analysis revealed that the thin layer of nickel was removed and the copper plate was exposed as the current collector.

The in house produced nickel coating was not adequate for long term usage, which suggests that the approximately 10 micrometre nickel layer deposited onto the copper endplate was not enough to withstand alkaline exposure and cycling conditions. The electroplating process must be optimised for better quality electrodes. Investigating the root causes for this deterioration fall outside the scope of this thesis. However, it is recommended to use a commercially available nickel plate for future prototypes.

- Contact and adhesion:

The contact between the current collector and bipolar electrode was not equal all over the surface due to material build-up and electrode thickness difference.

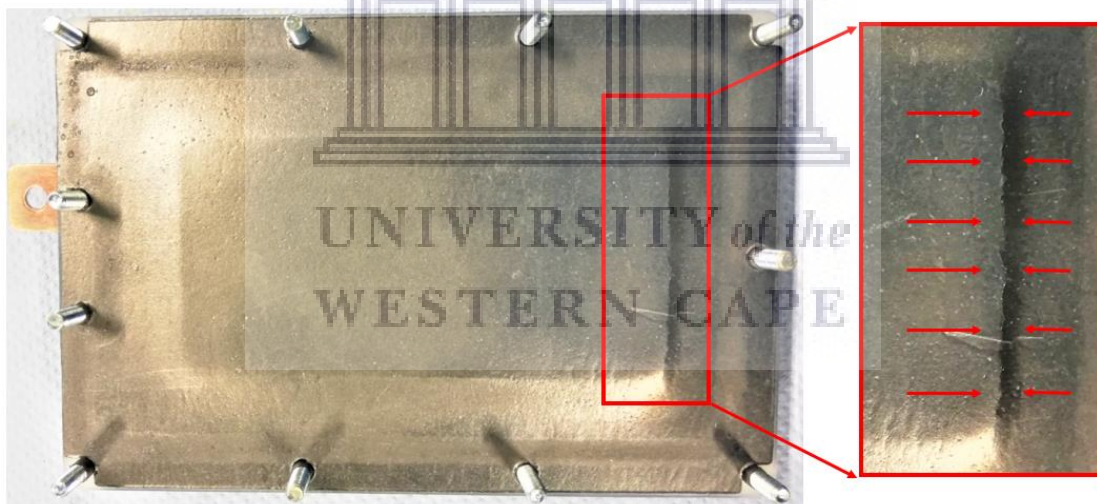


Figure 78 : Photo of the bipolar electrode cracks

As shown in Figure 78, the backside of one end-plate electrode, usually in contact with the current collector, demonstrated visible cracks on its structure, which indicate the build-up of internal mechanical stress within the welded cells, compromising the cell tightness and causing electrolyte leakage out of the electrolyte chamber. One of the envisaged solutions to reduce this phenomenon is to expand the electrolyte chamber to allow the expansion of the nickel based electrode.



- Battery electrolytes:

It was noted that during testing, a bigger electrolyte chamber is needed to ensure better ionic conduction and prevent kinetic limitations for ion transport in electrolyte.

- Separator :

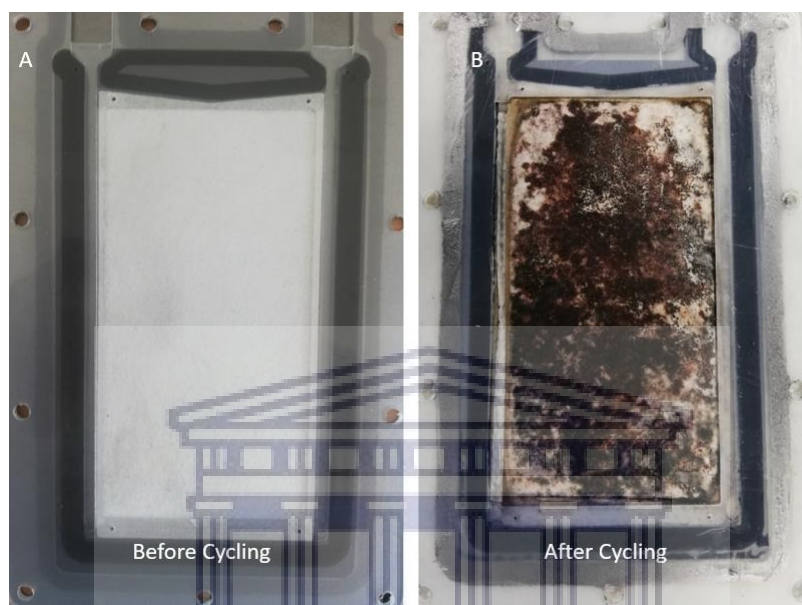


Figure 79 : Photo comparison of battery separator (A) before and (B) After cycling

As shown in Figure 79, the material transport of the active material between the two electrodes caused a material deposition on top of the separator causing a blockage that extended during battery cycling. Before battery cycling, (A) the fresh separator exhibited a clear surface with no visible stains, after cycling, (B) the post mortem analysis showed that the material deposited on the two side of the separator is blocking the separator surface, due to a possible electrode swelling on the Ni cathode, also some iron oxides residue on the Fe anode side.

## 5 Conclusions

This research was carried out in an attempt to develop a cost-effective Ni-Fe battery prototype that could potentially be used in large-scale energy storage systems.

Nickel Mesh and industrial grade Ni(OH)<sub>2</sub> powder was used to produce prototype electrodes. These electrodes were characterised by physical characterisation techniques such as XRD, and SEM. Cyclic voltammetry and galvanostatic cycling were performed to study reversibility of the electrochemical reactions. The electrochemical performance of the first prototype electrodes was confirmed at 90mAh/g nickel. Binder materials and conductive additives were used to improve the energy storage performance. It was found that the addition of 10% graphite instead of Carbon Black did not only improve the overall conductivity but also the stability of the electrodes by preventing swelling during charging.

Subsequently, with the addition of 5% copper, both stability and specific capacity were further improved, the latter reached an optimised performance of 140 mAh.g<sup>-1</sup> Ni.

After this cathode material composition optimisation, the hot press method was selected in an attempt to adhere the active material onto the graphite loaded polymer current collector, the “bipolar plate”. Plasma etching was applied in an attempt to improve surface adhesion. When an increase in the roughness was finally confirmed, a far more practical technique using sandpaper had proven to be effective and adopted going forward. The optimal hot press temperature, pressure and press time were established and found to be 110°C, 25 MPa and 5 minutes.

Reproducibility of the electrode was greatly enhanced when the Stainless steel mould was replaced by silicon. The new mould allowed the project team to produce multiple electrodes with minimal variation in thickness. Initially, electrode thickness from a pool of 10 sample ranged from 3.55mm to 4.36mm. After the silicon mould was used this range was reduced to 3.50- 3.54mm.

Subsequently, 3 NiFe batteries prototypes were produced using laser welding technique developed by the Fraunhofer UMSICHT Institute. All prototypes were leak free. The charge and discharge behaviour of the battery stacks were analysed, followed by a post mortem



analysis charged and discharged.

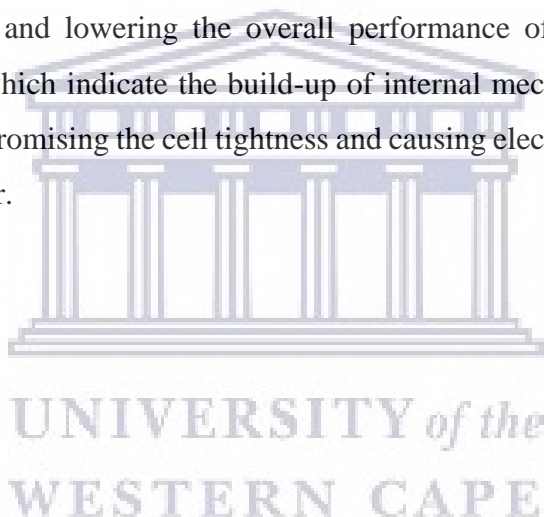
The bipolar design was proven as a working concept. Although the stability of the electrodes were improved during the course of the project, further research is necessary before stacks can be produced which could be considered economically viable.

## 6 Recommendations

Based on the observations and deductions made throughout the process of achieving the aim and objectives of this study, several recommendations can be made that would necessitate further study to improve the current findings. The recommendations made for future studies are as follows:

- Modifying synthesis methods of the electrode materials to nanostructure particles will allow more electrochemical surface area which will contribute to the capacity enhancement. One of the promising technologies is electro-spinning, Nano-sized active material can be sprayed into a conductive net made using a highly conductive polymer, creating electrical pathways within the electrode.
- Optimisation of the battery design by increasing the electrolyte chamber volume. It was noted during this study that the volume of the electrolyte inside the chamber is not sufficient, the space between the two consecutive cells does not allow for intensive gassing while charging at high rates. It was observed that the cells lose too much electrolyte in a short lapse of time. This issue requires a continuous filling of the electrolyte to ensure a stable performance of the battery stack.
- Trying other commercial active material and testing for its electrochemical performance in the battery. In this study, the usage of industrial-grade nickel hydroxide could be the reason for limited performance especially when it comes to the capacity fade and degradation of the electrochemical performance such as cycling capability.

- Developing a formation set up for a Fe-based electrode to enhance the overall performance of the battery. This will allow the iron-based electrodes to gas freely before being introduced in the bipolar stack, which will prevent a major gassing when being cycled inside the stack.
- The in-house electroplating did not yield a stable Ni coating, due to an alkaline corrosion, where the outer layer showed a weak resistance to such alkaline environment. Use of commercially available Ni-plated Cu plates, or solid Ni should be considered.
- The separator fabric showed a deposition of the electrochemical species moving between the two consecutive cells, eventually this deposition led to an increase of the internal resistance and lowering the overall performance of the battery stack. The expansion of the which indicate the build-up of internal mechanical stress within the welded cells, compromising the cell tightness and causing electrolyte leakage out of the electrolyte chamber.



## References

- [1] Iea, "World Energy Outlook 2007," World energy outlook, 2007.
- [2] A. Poullikkas, "Implementation of distributed generation technologies in isolated power systems," *Renew. Sustain. Energy Rev.*, vol. 11, no. 1, pp. 30–56, 2007.
- [3] F. S. Fabiani Appavou, Adam Brown, Bärbel Epp, Duncan Gibb, Bozhil Kondev, Angus McCrone, Hannah E. Murdock, Evan Musolino, Lea Ranalder, Janet L. Sawin, Kristin Seyboth, Jonathan Skeen, *Renewables in Cities - 2019 Global Status Report*. 2019.
- [4] F. Díaz-González, A. Sumper, O. Gomis-Bellmunt, and R. Villafáfila-Robles, "A review of energy storage technologies for wind power applications," *Renew. Sustain. Energy Rev.*, vol. 16, no. 4, pp. 2154–2171, 2012.
- [5] R. Dell, "Energy storage 128;148; a key technology for global energy sustainability," *J. Power Sources*, vol. 100, no. 1–2, pp. 2–17, 2001.
- [6] T. U. Daim, X. Li, J. Kim, and S. Simms, "Evaluation of energy storage technologies for integration with renewable electricity: Quantifying expert opinions," *Environ. Innov. Soc. Transitions*, vol. 3, pp. 29–49, 2012.
- [7] D. Anderson and M. Leach, "Harvesting and redistributing renewable energy: On the role of gas and electricity grids to overcome intermittency through the generation and storage of hydrogen," *Energy Policy*, vol. 32, no. 14, pp. 1603–1614, 2004.
- [8] I. Hadjipaschalis, A. Poullikkas, and V. Efthimiou, "Overview of current and future energy storage technologies for electric power applications," *Renew. Sustain. Energy Rev.*, vol. 13, no. 6–7, pp. 1513–1522, 2009.
- [9] N. K. C. Nair and N. Garimella, "Battery energy storage systems: Assessment for small-scale renewable energy integration," *Energy Build.*, vol. 42, no. 11, pp. 2124–2130, 2010.
- [10] A. H. Abdalla, C. I. Oseghale, J. O. G. Posada, and P. J. Hall, "Rechargeable nickel – iron batteries for large- scale energy storage," pp. 1–6, 2016.
- [11] J. Omar et al., "Aqueous batteries as grid scale energy storage solutions," 2016.
- [12] C. Kao, Y. Tsai, and K. Chou, "Synthesis and characterization of the iron / copper composite as an electrode material for the rechargeable alkaline battery," *J. Power Sources*, vol. 196, no. 13, pp. 5746–5750, 2011.
- [13] T. B. and D. Linden, *Linden's handbook of batteries*, McGraw-Hill Professional.
- [14] L. Huang, J. Yang, P. Liu, D. Zhu, and Y. Chen, "Copper / Iron Composite Anode prepared by in situ co- precipitation with Excellent High-rate and Low-temperature Performance for Rechargeable Nickel-Iron Battery," vol. 13, pp. 7045–7056, 2018.
- [15] A. K. Manohar, S. Malkhandi, B. Yang, C. Yang, G. K. Surya, and S. R. Narayanan, "A High-Performance Rechargeable Iron Electrode for Large-Scale Battery-Based Energy Storage," vol. 159, no. 8, pp. 1209–1214, 2012.
- [16] K. Vijayamohanam, T. S. Balasubramanian, and A. K. Shukla, "Rechargeable alkaline iron electrodes," vol. 34, pp. 269–285, 1991.
- [17] P. Hayes and J. Arevalo, *Energy storage*, vol. 4. 2015.
- [18] J. Baker, "New technology and possible advances in energy storage," *Energy Policy*, vol. 36, no. 12, pp. 4368–4373, 2008.

- [19] S. M. Schoenung, "Characteristics and technologies for long-vs. short-term energy storage," United States Dep. Energy, no. March, p. 46 pp., 2001.
- [20] B. Multon, J. Peter, B. Multon, J. P. Le, B. Multon, and J. Peter, "Le stockage de l' énergie électrique . Moyens et applications To cite this version : HAL Id : hal-00674068," 2012.
- [21] L.- Janvier, H. Ibrahim, A. Ilinca, and J. Perron, " Solutions de stockage de l'energie eolienne, Rapport interne," no. 418, pp. 1–80, 2006.
- [22] IUPAP, "Report on Research and Development of Energy Technologies Edited By Iupap Working Group on Energy," 2004.
- [23] "Impasses and controversies of hydroelectricity," vol. 21, no. 59, pp. 139–154, 2007.
- [24] B. Dursun and B. Alboyaci, "The contribution of wind-hydro pumped storage systems in meeting Turkey's electric energy demand," *Renew. Sustain. Energy Rev.*, vol. 14, no. 7, pp. 1979–1988, 2010.
- [25] J. Eyer, "Energy Storage for the Electricity Grid : Benefits and Market Potential Assessment Guide A Study for the DOE Energy Storage Systems Program," no. February, 2010.
- [26] J. K. Kaldellis and D. Zafirakis, "Optimum energy storage techniques for the improvement of renewable energy sources-based electricity generation economic efficiency," *Energy*, vol. 32, no. 12, pp. 2295–2305, 2007.
- [27] "Pumped hydroelectric energy storage and spatial diversity of wind resources as methods of improving utilization of renewbal energy sources, Jonah G . Levine," 2007.
- [28] R. A. Huggins, *Energy Storage* .
- [29] ESA, "Compressed Air Energy Storage (CAES)," vol. 2, no. 2, pp. 106–112, 2014.
- [30] E. Drury, P. Denholm, and R. Sioshansi, "The value of compressed air energy storage in energy and reserve markets," *Energy*, vol. 36, no. 8, pp. 4959–4973, 2011.
- [31] H. Ibrahim, A. Ilinca, and J. Perron, "Energy storage systems-Characteristics and comparisons," *Renew. Sustain. Energy Rev.*, vol. 12, no. 5, pp. 1221–1250, 2008.
- [32] P. Denholm, E. Ela, B. Kirby, and M. Milligan, "The role of energy storage with renewable electricity generation," *Energy Storage Issues Appl.*, no. January, pp. 1–58, 2011.
- [33] H. Chen, T. N. Cong, W. Yang, C. Tan, Y. Li, and Y. Ding, "Progress in electrical energy storage system: A critical review," *Prog. Nat. Sci.*, vol. 19, no. 3, pp. 291–312, 2009.
- [34] S. Succar and R. Williams, "Princeton Environmental Institute,Princeton University ,Energy Systems Analysis Group Compressed Air Energy Storage : Theory , Resources , And Applications For Wind Power Acknowledgments," *Princet. Environ. Inst. Rep.*, vol. 8, no. April, p. 81, 2008.
- [35] D. J. Swider, "Compressed air energy storage in an electricity system with significant wind power generation," *IEEE Trans. Energy Convers.*, vol. 22, no. 1, pp. 95–102, 2007.
- [36] F. Report, "EPRI-DOE Handbook of Energy Storage for Transmission & Distribution Applications," *Power*, vol. 2, no. December, p. 512, 2003.
- [37] P. Nikolaidis and A. Poullikkas, "A comparative review of electrical energy storage systems for better sustainability," vol. 97, no. 3, pp. 220–245, 2017.
- [38] D. Fernandes, F. Pitié, G. Cáceres, and J. Baeyens, "Thermal energy storage: 'How previous findings determine current research priorities,'" *Energy*, vol. 39, no. 1, pp. 246–257, 2012.
- [39] S. van der Linden, "Bulk energy storage potential in the USA, current developments and future

- prospects,” *Energy*, vol. 31, no. 15, pp. 3446–3457, 2006.
- [40] S. M. Hasnain, “Review on sustainable thermal energy storage technologies, part I: Heat storage materials and techniques,” *Energy Convers. Manag.*, vol. 39, no. 11, pp. 1127–1138, 1998.
- [41] A. Sharma, V. V. Tyagi, C. R. Chen, and D. Buddhi, “Review on thermal energy storage with phase change materials and applications,” *Renew. Sustain. Energy Rev.*, vol. 13, no. 2, pp. 318–345, 2009.
- [42] Z. Bin, “Solid oxide fuel cell (SOFC) technical challenges and solutions from nano-aspects,” *Int. J. energy Res.*, vol. 31, no. August 2007, pp. 135–147, 2009.
- [43] N. Maruoka, K. Sato, J. I. Yagi, and T. Akiyama, “Development of PCM for recovering high temperature waste heat and utilization for producing hydrogen by reforming reaction of methane,” *ISIJ Int.*, vol. 42, no. 2, pp. 215–219, 2002.
- [44] M. Medrano, A. Gil, I. Martorell, X. Potau, and L. F. Cabeza, “State of the art on high-temperature thermal energy storage for power generation. Part 2-Case studies,” *Renew. Sustain. Energy Rev.*, vol. 14, no. 1, pp. 56–72, 2010.
- [45] D. Laing, C. Bahl, T. Bauer, D. Lehmann, and W. D. Steinmann, “Thermal energy storage for direct steam generation,” *Sol. Energy*, vol. 85, no. 4, pp. 627–633, 2011.
- [46] L. F. Cabeza and H. Mehling, *Review on thermal energy storage with phase change : materials , heat transfer analysis and applications*, vol. 23. 2003.
- [47] F. Bai, Y. Wang, Z. Wang, Y. Sun, and A. Beath, “Economic evaluation of shell-and-tube latent heat thermal energy storage for concentrating solar power applications,” *Energy Procedia*, vol. 69, pp. 737–747, 2015.
- [48] P. Simon, Y. Gogotsi, U. P. Sabatier, I. U. De France, and B. Saint Michel, “Materials for electrochemical capacitors,” pp. 845–854.
- [49] M. S. Whittingham, “Materials Challenges Facing Electrical Energy Storage,” vol. 33, no. April, pp. 411–421, 2008.
- [50] N. Amaro, J. M. Pina, J. Martins, and J. M. Ceballos, “A Study on Superconducting Coils for Superconducting Magnetic Energy Storage ( SMES ) Applications,” vol. 2, no. 1, pp. 449–456.
- [51] W. Rucklcs and W. V Ihssenzahl, “Superconducting Magnetic Energy Storage.”
- [52] D. U. Sauer and G. Fuchs, “Technology Overview on Electricity Storage Overview on the potential and on the deployment,” no. June, 2012.
- [53] J. Lefebvre et al., “Renewable Power-to-Gas : A technological and economic review,” 2015.
- [54] M. Jentsch, T. Trost, and M. Sterner, “Optimal use of Power-to-Gas energy storage systems in an 85% renewable energy scenario,” *Energy Procedia*, vol. 46, pp. 254–261, 2014.
- [55] E. Energy and S. Systems, No Title .
- [56] F. Report, “EPRI-DOE Handbook of Energy Storage for Transmission & Distribution Applications,” no. December, 2003.
- [57] A. Z. Weber, M. M. Mench, J. P. Meyers, P. N. Ross, J. T. Gostick, and Q. Liu, “Redox flow batteries : a review,” pp. 1137–1164, 2011.
- [58] W. Paper, “Executive summary.”
- [59] F. Pan and Q. Wang, “Redox Species of Redox Flow Batteries : A Review,” no. November, pp. 20499–20517, 2015.

- [60] D. Linden and T. B. Reddy, Handbook of batteries, McGraw-Hill Professional.
- [61] R. Article, "A brief review on key technologies in the battery management system of electric vehicles," 2018.
- [62] P. M. Utc, "All About Batteries," 2018, © Adafruit Industries.
- [63] H. Zhao, Q. Wu, S. Hu, H. Xu, and C. Nygaard, "Review of energy storage system for wind power integration support," Appl. Energy, vol. 137, pp. 545–553, 2015.
- [64] P. Bernard and M. Lippert, Nickel e Cadmium and Nickel e Metal Hydride Battery Energy Storage. Elsevier B.V., 2015.
- [65] C. Chakkaravarthy, "The nickel / Iron battery," vol. 35, pp. 21–35, 1991.
- [66] S. L. Medway and C. A. Lucas, "In situ studies of the oxidation of nickel electrodes in alkaline solution," vol. 587, pp. 172–181, 2006.
- [67] L. Angeles, "(12) Patent Application Publication (10) Pub. No.: US 2015/0086884 A1," vol. 1, no. 19, 2015.
- [68] N. C. Æ. G. Mengoli, "Electrochemical investigations on composite iron electrodes," pp. 949–959, 2007.
- [69] M. K. Ravikumar, "Nickel / iron," vol. 51, pp. 29–36, 1994.
- [70] B. Hariprakash, S. K. Martha, M. S. Hegde, and A. K. Shukla, "A sealed , starved-electrolyte nickel – iron battery," pp. 27–32, 2005.
- [71] W. Ferrando, W. W. Lee, and R. A. Sutula, vol. 12, pp. 249–265, 1984.
- [72] R. D. Armstrong and I. Baurhoo, "65°C The response on a disc electrode under repetitive sweep conditions is shown in Fig. 1, together with the corresponding response on a gold ring," vol. 34, no. i, pp. 41–46, 1971.
- [73] D. Owen, "The Electrochemistry of Iron in 1M Lithium Hydroxide Solution at 22 ~ and 200~," vol. 120, no. 3, pp. 317–324, 1973.
- [74] "their Capacity and Stability in Rechargeable Alkaline Batteries Morphology and Phase Changes in Iron Anodes Affecting their Capacity and Stability in Rechargeable Alkaline Batteries," 2018.
- [75] M. Pourbaix, "Atlas of Electrochemical Equilibria in Aqueous Solutions."
- [76] W. M. Latimer, "The oxidation states of the elements and their potentials in aqueous solutions." Prentice-Hall, inc., New York, pp. xiv, 1 l., 352 p., 1938.
- [77] T. S. Balasubramanian, K. Vijayamohanam, S. State, and S. C. Unit, "Mechanisms of the discharge of porous-iron electrodes in alkaline medium," vol. 23, pp. 947–950, 1993.
- [78] D. Chen, J. Cheng, Y. Wen, J. Pan, G. Cao, and Y. Yang, "Study of Nickel-Plated Monolithic Porous Carbon as a Substrate for Nickel Hydroxide Electrode," vol. 8, pp. 6467–6477, 2013.
- [79] D. M. Constantin, E. M. Rus, L. Oniciu, and L. Ghergari, "The influence of some additives on the electrochemical behaviour of sintered nickel electrodes in alkaline electrolyte," pp. 188–197, 1998.
- [80] H. A. Company and E. D. Division, "Microcalorimetric study of the self-discharge of the NiOOH ] Ni ( OH ) z electrode in a hydrogen environment," vol. 22, pp. 409–414, 1992.
- [81] A. Van Der Ven, D. Morgan, Y. S. Meng, and G. Ceder, "Phase Stability of Nickel Hydroxides and Oxyhydroxides," pp. 210–215, 2006.



- [82] K. Huang and K. Chou, "Microstructure changes to iron nanoparticles during discharge / charge cycles," vol. 9, pp. 1907–1912, 2007.
- [83] C. A. Caldas, M. C. Lopes, and I. A. Carlos, "The role of FeS and  $\frac{1}{2} \text{NH}_4 / \text{CO}_3$  additives on the pressed type Fe electrode," no. January, pp. 108–112, 1998.
- [84] C. Kao and K. Chou, "Iron / carbon-black composite nanoparticles as an iron electrode material in a paste type rechargeable alkaline battery," vol. 195, pp. 2399–2404, 2010.
- [85] J. Mrha, Z. Zkbranskfr, and V. Koudelka, "Plastic bonded electrodes for nickel-cadmium accumulators ii. basic electrochemical parameters of the nickel oxide electrode," vol. c, pp. 239–250, 1979.
- [86] A. Datta and R. Cited, "Mai muuttunut piu miu minim vui," vol. 2, 2018.
- [87] S. E. Dr.-Ing. Anna Grevé Fraunhofer-Institut für Umwelt-, "BiNiFe development of a Low-Cost Bipolar Ni-Fe Battery for Energy Storage," 2019. .
- [88] S. M. D. Wally E. Rippel and both of C. B. Edwards, Pasadena, "Bipolar battery construction," 4,275,130, 1981.
- [89] K. R. Bullock, "Progress and Challenges in Bipolar Lead-Acid Battery Development," vol. 142, no. 5, pp. 1726–1731, 1995.
- [90] T. Liu, Y. Zhang, C. Chen, Z. Lin, S. Zhang, and J. Lu, "recyclable sodium ion battery," Nat. Commun., no. 2019, pp. 1–7.
- [91] Y. Gambe, Y. Sun, and I. Honma, "Development of Bipolar All-solid-state Lithium Battery Based on," pp. 10–13, 2015.
- [92] M. Park, J. Ryu, W. Wang, and J. Cho, "Material design and engineering of next-generation flow-battery technologies," Nat. Publ. Gr., vol. 1, pp. 1–18, 2016.
- [93] W. Zhang, W. Jiang, L. Yu, Z. Fu, W. Xia, and M. Yang, "Effect of nickel hydroxide composition on the electrochemical performance of spherical Ni ( OH ) 2 positive materials for Ni – MH batteries," Int. J. Hydrogen Energy, vol. 34, no. 1, pp. 473–480, 2009.
- [94] H. Karami, M. Fazlollah, and M. Shamsipur, "Short communication A novel dry bipolar rechargeable battery based on polyaniline," vol. 124, pp. 303–308, 2003.
- [95] N. J. Lee et al., "Development of Carbon Composite Bipolar Plates for Vanadium Redox Flow Batteries," vol. 33, no. 11, pp. 3589–3592, 2012.
- [96] G. Zhou et al., "An Aqueous Inorganic Polymer Binder for High Performance Lithium – Sulfur Batteries with Flame-Retardant Properties," 2017.
- [97] N. (CA) Josef Daniel-Ivad, "Rechargeable alkaline manganese cell with cathode consistency compensation," US 7,718,305 B2, 2010.
- [98] J. Omar, G. Posada, P. J. Hall, J. Omar, and G. Posada, "Towards the development of safe and commercially viable nickel – iron batteries : improvements to Coulombic efficiency at high iron sulphide electrode formulations," J. Appl. Electrochem., vol. 46, no. 4, pp. 451–458, 2016.
- [99] Bochimie, "Nickel hydroxide MSDS," 2015.
- [100] T. Tawonezvi, "Development of a Composite Iron-Matrix Electrode for Nickel-Iron Battery Energy Storage Systems," Cape Peninsula University, 2019.
- [101] L. Kopietz, J. Girschik, P. Schwerdt, J. Burfeind, A. Grevé, and C. Doetsch, "Redox-flow batteries," no. May, 2018.

- [102] J. Azevedo, T. Seipp, J. Burfeind, C. Sousa, A. Bentien, and J. P. Araújo, “Photoelectrochemical redox flow battery,” *Nano Energy*, 2016.
- [103] N. M. André et al., “ed us cr t,” *J. Adhes.*, vol. 0, no. 0, 2017.
- [104] P. Kritzer and J. Anthony, “Nonwovens as Separators for Alkaline Batteries An Overview,” 2007.
- [105] J. Epp, 4 - X-ray diffraction 40;XRD 41; techniques for materials characterization. Elsevier Ltd, 2016.
- [106] D. Stokes, Principles and practice of variable pressure/environmental scanning electron microscopy (VP-ESEM). Chichester, U.K: Wiley., 2008.
- [107] T. J. Davies, Æ. C. E. Banks, and Æ. R. G. Compton, “Voltammetry at spatially heterogeneous electrodes,” pp. 797–808, 2005.
- [108] K. J. Rountree, B. D. Mccarthy, E. S. Rountree, T. T. Eisenhart, and J. L. Dempsey, “A Practical Beginner ’ s Guide to Cyclic Voltammetry,” 2017.
- [109] www.zahner.de, “ZAHNER-elektrik GmbH & Co. KG.” .
- [110] J. Y. Pyun, S.I., Shin, H.C., Lee, J.W. & Go, Electrochemistry of insertion materials for hydrogen and lithium. Springer., 2012th ed. Springer, 2012.
- [111] J. H. L. Hadden, M. P. Ryan, and D. J. Riley, “Electrochemistry Communications Examining the charging behaviour of nickel hydroxide nanomaterials,” *Electrochem. commun.*, vol. 101, no. November 2018, pp. 47–51, 2019.
- [112] V. Kotok, V. Kovalenko, and V. Malyshev, “Comparaison of oxygen evolution parameters,” vol. 71, pp. 12–19, 2017.
- [113] L. Bing, Y. Huatang, Z. Yunshi, Z. Zuoxiang, and S. Deying, “Cyclic voltammetric studies of stabilized a -nickel hydroxide electrode,” pp. 277–280, 1999.
- [114] P. Oliva et al., “Review of the structure and the electrochemistry,” vol. 8, pp. 229–255, 1982.
- [115] H. Aircraft, “Koh concentration effect on the cycle life of nickel-hydrogen cells iv. results of failure analyses,” vol. 29, pp. 503–519, 1990.
- [116] L. Demourgues-guerlou and C. Delmas, “Effect of Iron on the Electrochemical Properties of the Nickel Hydroxide Electrode,” vol. 141, no. 3, pp. 7–11, 1994.
- [117] A. Brisse and P. Stevens, “Ni ( OH )<sub>2</sub> and NiO Based Composites : Battery Type Electrode Materials for Hybrid Supercapacitor Devices.”
- [118] W. Zhu, J. Ke, H. Yu, and D. Zhang, “POWER SllURc~,” vol. 56, pp. 75–79, 1995.
- [119] B. Shruthi et al., “Journal of Science : Advanced Materials and Devices Synthesis , spectroscopic analysis and electrochemical performance of modi fi ed b -nickel hydroxide electrode with CuO,” *J. Sci. Adv. Mater. Devices*, pp. 8–13, 2016.
- [120] X. Cao, J. Wei, Y. Luo, Z. Zhou, and Y. Zhang, “Spherical nickel hydroxide composite electrode,” vol. 25, pp. 643–647, 2000.
- [121] B. Liu, X. Y. Wang, H. T. Yuan, Y. S. Zhang, D. Y. Song, and Z. X. Zhou, “Physical and electrochemical characteristics of aluminium-substituted nickel hydroxide,” pp. 855–860, 1999.
- [122] A. H. Zimmerman and P. K. Effa, “Discharge Kinetics of the Nickel Electrode,” no. 4, pp. 709–713, 1983.

- [123] X. Y. Wang, J. Yan, Y. S. Zhang, H. T. Yuan, and D. Y. Song, “Cyclic voltammetric studies of pasted nickel hydroxide electrode microencapsulated by cobalt,” vol. 28, pp. 1377–1382, 1998.
- [124] A. K. Shukla, S. Venugopalan, and B. Hariprakash, “Nickel-based rechargeable batteries,” vol. 100, pp. 125–148, 2001.
- [125] M. I. T. Electric and V. Team, “A Guide to Understanding Battery Specifications,” no. December, 2008.
- [126] <https://www.binder-world.com/en/products/vacuum-drying-chambers/series-vd/vd-115#1>, “Binder vd115,” BINDER GmbH – Headquarters Im Mittleren Ösch 5 78532 Tuttlingen Germany Phone: +(49) 7462 2005-0 Fax: +(49) 7462 2005-100 info@binder-world.com. .



UNIVERSITY *of the*  
WESTERN CAPE

## **Appendix A: Definition of battery parameters**

### **Battery Capacity**

Typically expressed in Amp-hr and determined by the mass of active material contained in the battery. The battery capacity represents the maximum amount of energy that can be extracted from the battery under certain specified conditions. However, the actual energy storage capabilities of the battery can vary significantly from the "nominal" rated capacity, as the battery capacity depends strongly on the age and history of the battery, the charging or discharging regimes of the battery, and the temperature [125].

### **Columbic Efficiency**

The columbic efficiency of the battery is defined as the ratio of the charges entering the battery during the charging process compared to the charges that can be delivered during the discharge process [125].

### **Cycle Life (the number for a specific DOD)**

The number of discharge-charge cycles the battery can experience before it fails to meet specific performance criteria. Cycle life is estimated for specific charge and discharge conditions. The actual operating life of the battery is affected by the rate and depth of cycles and by other conditions such as temperature and humidity. The higher the DOD, the lower the cycle life [125].

### **Depth of Discharge**

The Depth of Discharge (DOD) of a battery determines the fraction of power that can be withdrawn from the battery. Depth of Discharge (DOD) (%) – The percentage of battery capacity that has been discharged expressed as a percentage of maximum capacity. A discharge to at least 80 % DOD is referred to as a deep discharge [125].

### **Energy Density (Wh/L)**

The nominal battery energy per unit volume sometimes referred to as the volumetric energy density. Specific energy is a characteristic of the battery chemistry and packaging. Along with the energy consumption of the vehicle, it determines the battery size required to achieve a given electric range [125].

### **Energy or Nominal Energy (Wh (for a specific C-rate))**

The “energy capacity” of the battery, the total Watt-hours available when the battery is discharged at a certain discharge current (specified as a C-rate) from 100 percent state-of-charge to the cut-off voltage.

Energy is calculated by multiplying the discharge power (in Watts) by the discharge time (in hours). Like capacity, energy decreases with increasing C-rate[125].

### **Energy, Volumetric and Power Density**

Energy density is a parameter used chiefly to compare one type of battery system to another. The energy density of a battery is the capacity of the battery divided by either the weight of the battery, which gives the gravimetric energy density in Wh/kg or by the volume, which gives a volumetric energy density in Wh/dm<sup>3</sup> (or Wl/litre<sup>3</sup>) [125].

### **Internal Resistance**

The resistance within the battery, generally different for charging and discharging, also dependent on the battery state of charge. As internal resistance increases, the battery efficiency decreases, and thermal stability is reduced as more of the charging energy is converted into heat[125].

### **Maximum Continuous Discharge Current**

The maximum current at which the battery can be discharged continuously. This limit is usually defined by the battery manufacturer in order to prevent excessive discharge rates that would damage the battery or reduce its capacity. Along with the maximum continuous power of the motor, this defines the top sustainable speed and acceleration of the vehicle [125].

### **Open-circuit voltage (V)**

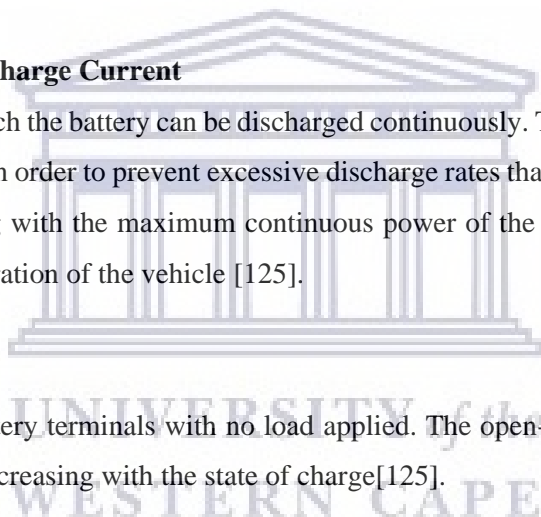
The voltage between the battery terminals with no load applied. The open-circuit voltage depends on the battery state of charge, increasing with the state of charge[125].

### **Power Density (W/L)**

The maximum available power per unit volume. Specific power is a characteristic of the battery chemistry and packaging. It determines the battery size required to achieve a given performance target [125].

### **Specific Energy (Wh/kg)**

The nominal battery energy per unit mass sometimes referred to as the gravimetric energy density. Specific energy is a characteristic of the battery chemistry and packaging. Along with the energy consumption of the vehicle, it determines the battery weight required to achieve a given electric range[125].



**Specific Power (W/kg)**

Specific power is the maximum available power per unit mass. Specific power is a characteristic of the battery chemistry and packaging. It determines the battery weight required to achieve a given performance target[125].

**Terminal Voltage (V)**

The voltage between the battery terminals with load applied. Terminal voltage varies with SOC and discharge/charge current.

**Voltage Efficiency**

The voltage efficiency is determined largely by the voltage difference between the charging voltage and voltage of the battery during discharging[125].





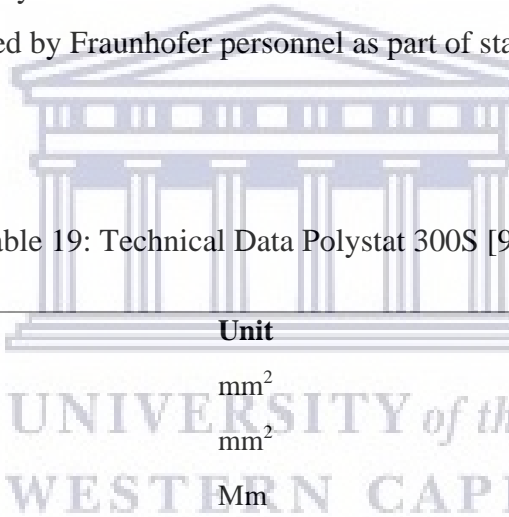
## Appendix B: Equipment used for the development of the electrodes.

### *Hydraulic Press*

Hydraulic hot pressing was selected as the manufacturing process of choice for the establishment of Ni- and Fe-based electrodes based on a preliminary study at Fraunhofer UMSICHT institute. Optimisation of the operating parameters of the hot-press included temperature, time, and pressure.

The technical data of the polystat 300S are detailed in *Table 19* Mandatory training to operate this equipment was provided by Fraunhofer personnel as part of standard safety protocols.

Table 19: Technical Data Polystat 300S [93]



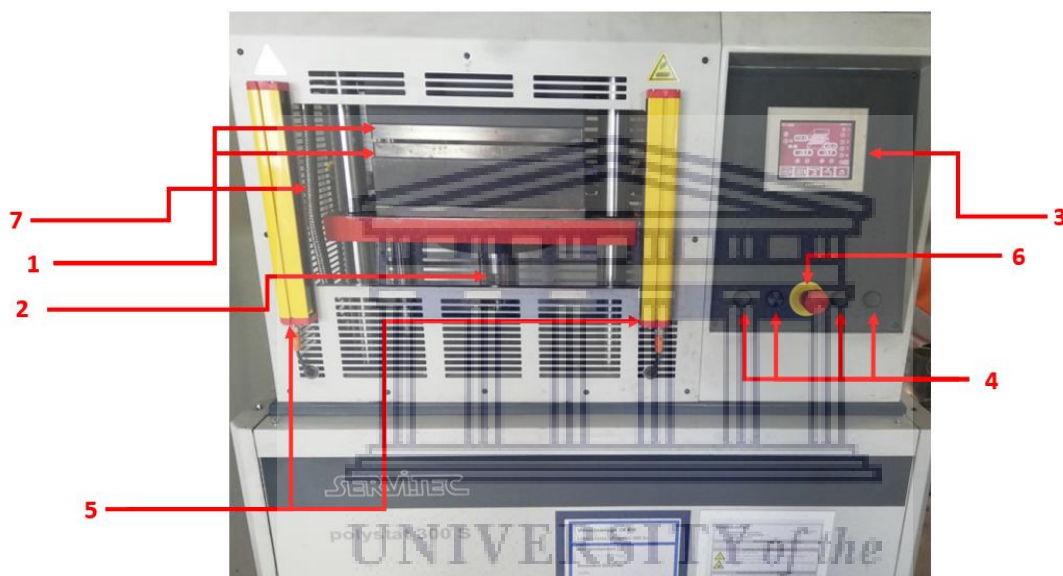
<b>Polystat 300 S</b>	<b>Unit</b>	<b>Value</b>
<b>Working Area</b>	mm <sup>2</sup>	300
<b>Plate dimension</b>	mm <sup>2</sup>	350
<b>Daylight opening</b>	Mm	195
<b>Press force</b>	Up to KN	450
<b>Hydraulic</b>	Up to bar	400
<b>Working temperature</b>	Up to °C	300
<b>Heating power per plate</b>	kW	8.0
<b>Machine length</b>	Mm	1200
<b>Machine depth</b>	Mm	650
<b>Machine height</b>	Mm	1550
<b>Machine weight</b>	Kg	800

As shown in Figure 80 the machine is laid out as a four-column-press with an integrated high-pressure hydraulic system to allow high press forces with a double-side operation cylinder. The hydraulic system uses oil and allows a working pressure of 500 N.cm<sup>-2</sup> equal to a press force

of 450 kN. An electronic pressure control unit allows pressure adjustments between 10 and 400 bar with an accuracy of +/- 5%.

The working area is made of a flat steel plate; the maximum temperature that can be reached is set to 300 °C, through an electrical power of 8 kW in each plate ensuring a heating rate of 10 °C/min. A solid-state-relay controls the temperature distribution of +/- 2 °C.

The cooling system is made of a counter-current bore system, in which pressurised water is circulating. Depending on the temperature range cooling rates between 10 °C/min and 20°C/min can be achieved.



- 1 Press plates
- 2 Hydraulic piston
- 3 Polycontrol a touch screen and PLC-control
- 4 Hand mode control button
- 5 Hand-in sensors
- 6 Emergency stop button
- 7 Water cooling pipes

Figure 80: Hot-Press Polystat 300S

As shown in Figure 81 the Polycontrol is a combination of PLC-control and touch screen for a user-friendly operation of the hot-press machine. The Polycontrol includes setpoint

management, program management with time sequences in four steps, and several other helpful functions.



Figure 81: Polycontrol Interface

### ***Vacuum Oven***

The vacuum oven BINDER VD 115 model, as depicted in Figure 80, was employed to facilitate the drying process during material synthesis and electrode treatment. Its technical data are detailed in *Table 20*.



Figure 82: Vacuum oven BINDER VD 115 model [126]

Table 20: Technical data of BINDER VD 115 model [126]

Performance Data (Temperature)	
Heating-up time to 100 °C [min]	95
Temperature fluctuation [ $\pm$ °C]	0.1
Temperature range 15 °C above ambient temperature to [°C]	200
Temperature variation at 100 °C [ $\pm$ °C]	3.5
Performance Data (Pressure)	
Leak rate [bar.h <sup>-1</sup> ]	0.01
Permitted end vacuum [mbar]	0.01

## Appendix C: Nickel electroplating of Cu current collector

### - Background information on Nickel electro-plating :

Essentially, the electrodeposition phase involves passing an electrical current between two electrodes submerged in an electrolyte. The positively charged electrode constitutes the anode whilst the cathode is the negatively charged electrode. The electrolyte contains particles or ions dissolved. When an electrical potential is applied between the electrodes these ions migrate towards the electrode with the opposite charge. The electrical energy is supplied by a DC power source. For nickel plating, the electrolyte contains soluble nickel salts such as Nickel sulphate, Nickel chloride, and Nickel Sulphamate [42].

### - Rate of Deposition

Electrodeposition, introduced by Faraday demonstrated that the amount of deposited metal at the cathode or the anode is proportional to the electricity amperage going through the electrical circuit. Faraday showed that the quantity of electricity required to deposit or dissolve 1 gram equivalent of a metal is a constant and has a value of 96,500 coulombs (ampere-seconds) or 26.799 ampere-hours. This is known as Faraday's Constant [42].

Using these relationships, it can be shown that the weight of nickel deposited at the cathode and the amount dissolved at the anode can be calculated from the following expression:

$$W = 1.095 It$$

Where W is the amount of nickel deposited at the cathode (or dissolved at the anode) in grams, I is the current that flows through the plating tank in amperes and t is the time that the current flows in hours [42].

The factor 1.095 in the above calculation is derived from Faraday's work discussed on the previous page. For a nickel, the atomic weight is 58.70 and the valence is 2, giving an equivalent weight of 29.35. Therefore, 26.799 ampere-hours will deposit (or dissolve) 29.35 grams of nickel or 1.095 grams per ampere-hour [42].

Alternatively, the average thickness can be computed directly from the current and time using the following calculation:

$$T = \frac{12.294 \cdot I \cdot t}{A}$$

Where T is the average thickness ( $\mu\text{m}$ ) and A is the area being electroplated ( $\text{dm}^2$ ), I is the current that flows through the plating tank in amperes and t is the time that the current flows in hours [42].

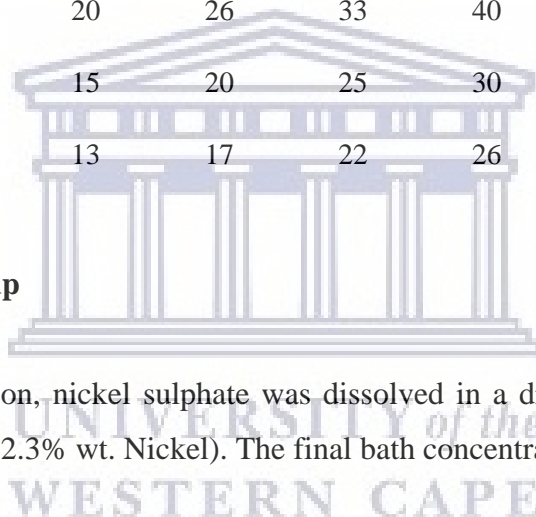
As shown in Table 21, the ratio of current to area  $I/A$  is known as the current density. It will be seen, therefore, that the average thickness depends on the current density and time, whereas the weight of nickel deposited (or dissolved at the anode) depends on the current and time. Usually in nickel plating, the current density will be expressed as  $\text{A} \cdot \text{dm}^{-2}$  [42].

Table 21 : Time to electrodeposit nickel at various current densities

Time in minutes to deposit the indicated average thickness of Nickel at various current densities.								
Current Density (A.dm <sup>-2</sup> )	5 µm	10 µm	15 µm	20 µm	25 µm	30 µm	40 µm	50 µm
1	26	51	77	100	128	154	200	255
2	13	26	39	51	65	78	100	130
2.5	11	22	32	42	53	64	84	105
3	8.5	17	26	34	43	52	68	85
4	6.5	13	20	26	33	40	51	65
5	5	10	15	20	25	30	41	50
6	4.5	8.5	13	17	22	26	34	43

**- Experimental setup**

To prepare the bath solution, nickel sulphate was dissolved in a distilled water to obtain a solution of NiSO<sub>4</sub>.6H<sub>2</sub>O (22.3% wt. Nickel). The final bath concentration was 250 g.L<sup>-1</sup>.





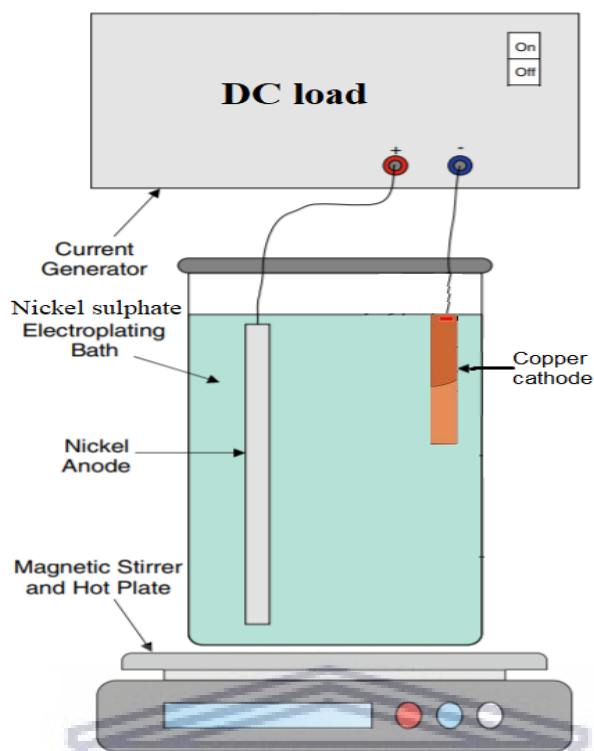


Figure 83 : Experimental setup for electroplating

As depicted in Figure 83 , the experimental procedure consisted of two major steps, first the preparation of the electrolyte solution, where a large volume beaker placed on a magnetic stirrer to ensure appropriate dissolution of the nickel salt, the second step consisted of connecting the electrodes to the DC load and set the electroplating parameters.

Approximately, 26 min of plating time was needed to obtain 10  $\mu\text{m}$  thickness layer of plated under a current density of 2  $\text{A}\cdot\text{dm}^{-2}$ . As illustrated in Figure 84 a photo of the copper electrodes was taken before and after the electroplating process.

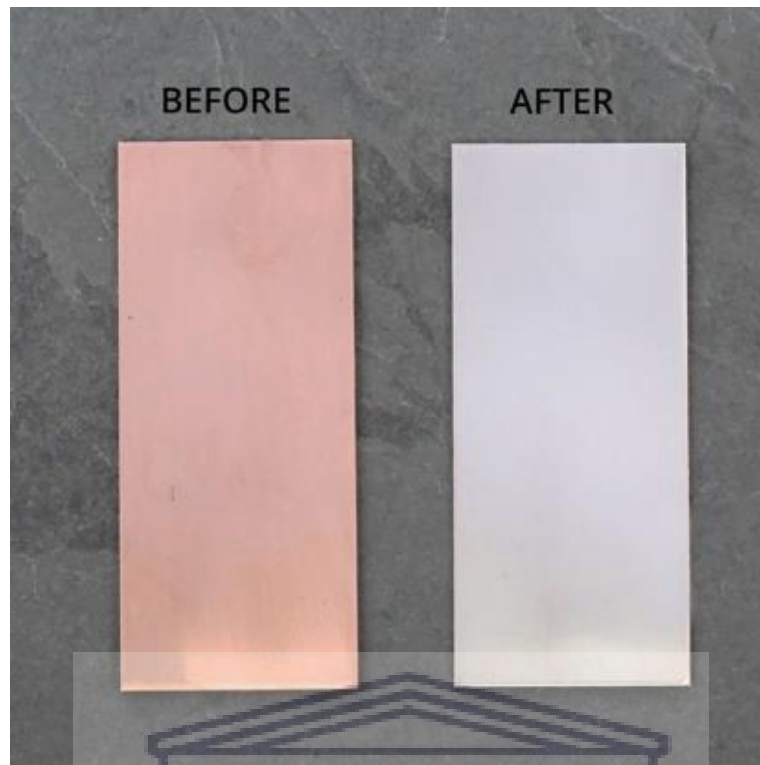


Figure 84 : Before and after nickel electroplating

